UNIVERSITÀ DEGLI STUDI DI PADOVA

Corso di Laurea Magistrale in Astronomia
Dipartimento di Fisica e Astronomia "G. Galilei"

POST-STARBURST GALAXIES IN CLUSTERS FROM THE GASP SURVEY

Relatore: Prof. Enrico Maria Corsini
Co-relatrice: Dott.ssa Daniela Bettoni

Laureanda:
Maria Santorelli 1145729

Anno Accademico 2017-2018

Contents

Abstract **1**

1 Introduction **3**
1.1 Post-starburst galaxies 3
1.2 Integral field spectroscopy 7
1.2.1 Integral field spectroscopy surveys 7
1.3 Purpose and structure of this thesis 9

2 The GASP project **11**
2.1 Description of the GASP sample 11
2.2 MUSE data reduction ad analysis 13
2.3 Brief outline of SINOPSIS 14

3 The galaxy sample **17**
3.1 Description of the galaxy sample 17
3.2 Surface photometry 20
3.3 Analysis of SINOPSIS data 35
3.3.1 Error budget 35
3.3.2 EW(Hβ) radial profiles 42
3.3.3 Star formation history 42
3.3.4 Luminosity and mass weighted ages 45

4 Overview of individual galaxies **49**
4.1 A3128_B_0248 49
4.2 A3158_11_91 49
4.3 A3158_B_0223 56
4.4 A3158_B_0234 56
4.5 A500_F_0152 63
4.6 A500_22_184 63
4.7 A1069_B_0103 63

4.8 A3376_B_0214 70

5 Main results **77**
5.1 Specific angular momentum 77
5.2 Color-magnitude diagram 81
5.3 PSB galaxies in the phase-space 82
5.4 Stellar mass vs (EW(Hβ)) mean 85
5.5 Mass-weighted age and luminosity-weighted age vs EW(Hβ) mean 86

6 Conclusions **87**

Abstract

Post-starburst galaxies, also known as k+a galaxies, show no sign of emission lines and prominent Balmer absorption lines in their spectra. They are in a transitional phase between the star forming and the passive galaxies.
I present here the study of a sample of eight post-starburst galaxies, belonging to five different galaxy clusters, from the GAs Stripping Phenomena with MUSE (Multi Unit Spectroscopic Explorer at the Very Large Telescope) project dataset. The data-cubes from MUSE had been analyzed in order to study their main properties.
In particular the 2D maps of Hβ equivalent width (EW), the star formation history and the specific angular momentum had been argued. These properties had been finally discussed and connected to their environment and morphology.

Chapter 1

Introduction

In this chapter I describe the main properties of PSB galaxies, as these objects are an important link in understanding the mechanisms of gas stripping in galaxies belonging to different environments. Furthermore, I introduced integral field spectroscopy and its main surveys performed with this observational technique.

1.1 Post-starburst galaxies

Many galaxy properties, such as color, morphology, and star formation rate (SFR), distribute the galaxy population in two broad classes: blue and red galaxies (Strateva et al. 2001, Baldry et al. 2004). This is evident in the color-magnitude diagram of local galaxies, where the galaxies split in a red sequence, characterized by red, quiescent early-type objects and a blue cloud, mainly populated by blue, star-forming, late-type disk galaxies (Figure 1.1). The galaxies in the midway between the two peaks are in the so called green valley. These are probably transition galaxies. Understanding the galaxy bimodal distribution, in particular the transition between the blue cloud and red sequence, is one of the main goals of research in contemporary extra-galactic astrophysics.

In this context, post-starburst (PSB) galaxies are a class of objects that can be considered caught in a transitional phase, in fact they have recently had a burst of star formation and all the gas has been transformed into stars.

The main characteristics that define this class of galaxies are: the presence of strong Balmer absorption lines, the strong Balmer decrement, and finally the lack of emission lines (see a typical PSB spectrum in Figure 1.2). In summary, PSB galaxies have just now consumed all their gas and this is

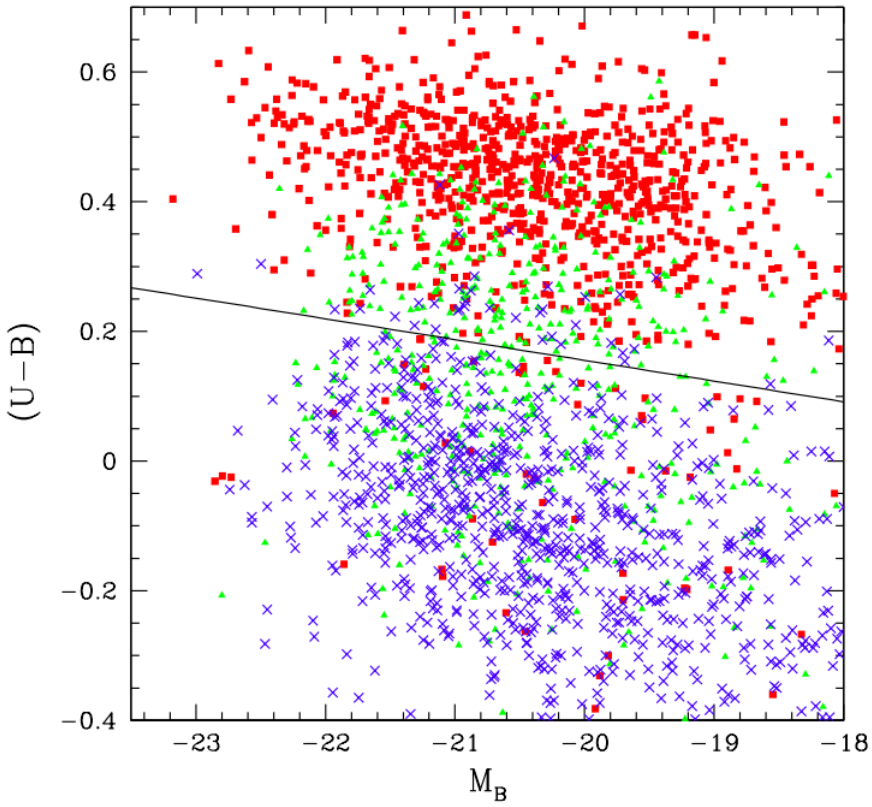

Figure 1.1: Color-magnitude diagram for nearby galaxies. A dicotomy in the distribution is observed: red and passive early-type galaxies, are in the so called red sequence, blue and star-forming late-type ones, are found in the blue cloud (Conselice 2006). Ellipticals are represented with red squares, spirals with blue crosses. The green triangles are galaxies in the so called "Green Valley". The solid line splits red sequence from the blue cloud galaxies (Faber et al., 2007).

indicated by the presence of a young stellar population. Sometimes these galaxies are defined as k+a because the spectra show typical features of both A and K stellar types.
A distinction has to be made: k+a spectra are typical not only for the PSB galaxies, but also for the post-starforming galaxies. PSB galaxies are objects where the star formation activity had been abruptely truncated after a burst, while the lattest are galaxies with normal star formation brusquely truncated without a star burst event (Poggianti, 2004).
Dressler and Gunn (1983), while studying spectra of high-redshift cluster galaxies, were the first to notice this kind of objects. They observed their peculiarities and suggested a scenario in which a star-burst has occurred in

recent epochs (up to $\sim 10^9$ yr ago), this to explain the presence of an A-type stellar population mixed with an older one (mainly composed by K-type stars). These galaxies were successively named e+a galaxies (used for the first time by Gunn and Dressler, 1988), as their spectra looked like a blend of those of elliptical galaxies and of A-type stars.
Alternatively to PSB and e+a, the term k+a galaxies is used (Franx, 1993; Poggianti et al. 1999) referring to spectra of K and A stars. PSB galaxies in clusters do not have a single morphological type, they span a wide range of morphologies excluding only the latest spirals and irregulars.
It is commonly accepted that k+a galaxies are observed in a short-lived phase, as they transit from the blue cloud to the red sequence and thus provide the opportunity to obtain unique insights into the processes driving the evolution of galaxies. For this reason it is crucial to define large galaxy samples. Recently, thanks to large spectroscopic surveys as the Sloan Digital Sky Survey (SDSS, York et al., 2000), Goto et al. (2003) have found that $\sim$ 1% of field galaxies in the local universe are in the PSB phase.
The lack of emission lines (such as [OIII]λ5007 or Hα) indicates that no ongoing star formation is present in these galaxies (Couch and Sharples, 1987). However, the presence of a young stellar population (composed by A-type stars) is a hint of a recent event of star formation occurred less than 1 Gyr ago.
Some studies refer to these galaxies as transitional objects, the missing link between blue star-forming disks and red passive early-type galaxies, belonging to the green valley (Zabludoff et al., 1996), even if not all the green valley galaxies show PSB features.
To explain the main features observed in the spectra of PSB galaxies, different origins have been proposed for the these objects.
The first proposed mechanism that could turn off star formation for a limited time is ram-pressure stripping. It could explain the presence of PSB galaxies in dense regions, such as clusters (Balogh et al., 2000). Blue early-type galaxies fall into the cluster potential well and their gas is stripped by the interaction with the hot intra-cluster medium, stopping star formation. In this context, their disk-like morphology is untouched (Couch and Sharples, 1987; Poggianti et al., 1999; Paccagnella et al., 2017). Other explanations involve galaxy interactions, such as tidal interactions close encounters, merging, or AGN (Active Galactic Nuclei) feedback (Goto, 2005; Yesuf et al., 2014). When gas-rich galaxies have a merging phase, a starburst occurs due to the fact that the gas is strongly disrupted. Such a perturbation leads the gas towards the center, causing another starburst and an AGN activity. This scenario particularly applies to field galaxies: the star formation is stopped

by the depletion of the gas or by the expulsion of it due to the AGN feedback. In this case the galaxy morphology is strongly disturbed, and should show signs of recent interaction, such as tails and asymmetry (Zabludoff et al., 1996).
In this work, I exploit a sample of PSB galaxies in clusters drawn from the GAs Stripping Phenomena with MUSE (GASP, Poggianti et al., 2017) survey. The Multi Unit Spectroscopic Explorer (MUSE, Bacon et al. 2010) is an integral field spectrograph and imager, installed on Yepun, the fourth unit telescope of the Very Large Telescope (VLT) at the Paranal Observatory (Chile). I investigate the properties of these galaxies in five clusters. The aim of this analysis is to shed light on the processes acting on these galaxies and on the timescale needed to trigger and quench the star formation.

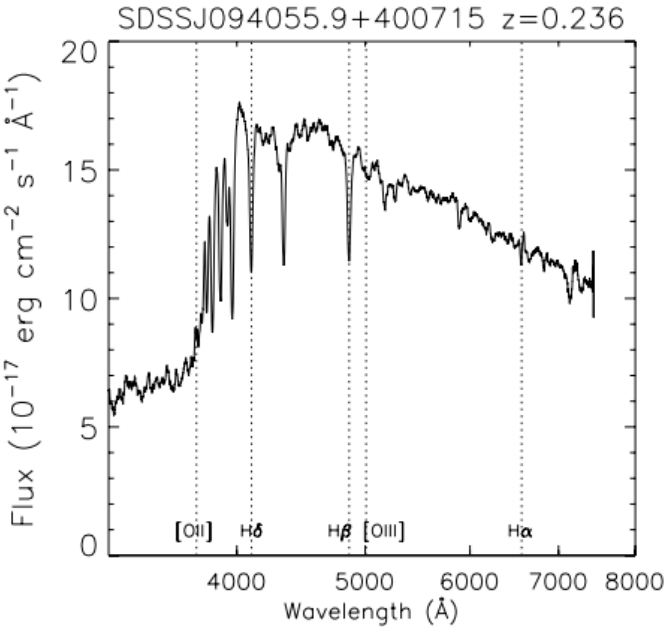

Figure 1.2: Rest-frame spectrum of a typical PSB galaxy from Goto et al. (2003). Its main features are the strong Balmer absorption lines and the lack of emission lines. The Balmer decrement in the region between ∼ 3000 and 4000 Å is clearly evident. Galaxy name and redshift are specified on the top of the figure.

1.2 Integral field spectroscopy

In this thesis, I will make use of data obtained from integral field spectroscopy (IFS), a technique that provides a spectrum for each position of the field of view. The resulting output is a spectral data-cube, containing the wavelength for each pixel coordinate (x, y), a so called spaxel. For this reason, I give a brief introduction to these particular data that are the "core" of the analysis for our sample galaxies. The instrument is located on a telescope focal plane and is composed by an integral field unit (IFU), or image slicer, and a spectrograph. IFS can map the whole field of view (Figure 1.3).
In the study of galaxies this is a powerful tool because it allows to derive simultaneously kinematic, spectral, and morphological information. Moreover, there is the possibility to span the whole wavelength range and detect also unexpected features.
So IFS provides a detailed analysis of both the spatial and spectral information of individual galaxies, allowing to study in a more complete way the physical parameters of these targets.

1.2.1 Integral field spectroscopy surveys

In the recent years, thanks to IFS a large number of surveys have been conducted to study the stellar and ionized gas kinematics of nearby galaxies ($z \sim 0$) over a wide range of galaxy masses. These surveys provide a fundamental contribution to our understanding of galaxy evolution and to characterize processes such as merging, environmental effects, star formation history and AGN presence.
For what concerns local galaxies, the PPAK Integral Field Spectroscopy Nearby Galaxies Survey (PINGS) (Rosales-Ortega et al., 2010) is a two-dimensional spectroscopic mosaic of 17 nearby disk galaxies in the optical wavelength range. This project represents the first attempt to obtain continuous coverage spectra of the whole surface of a galaxy in the nearby universe.
PINGS opened the way to surveys that link large photometric surveys of nearby galaxies, such as SDSS, with a large sample of IFS data. The Calar Alto Legacy Integral Field Area survey (CALIFA) (Sánchez et al., 2011), used the same spectrograph as PINGS, the PPAK IFU of the Potsdam Multi-Aperture Spectrograph (PMAS), instrument at the 3.5 m telescope at Calar Alto (Spain). Spectra from $\sim$ 3750 to 7000 Å of all morphological types were obtained for 600 local galaxies. The main purpose of CALIFA is to investigate the galaxy properties, such as age and metallicity of their

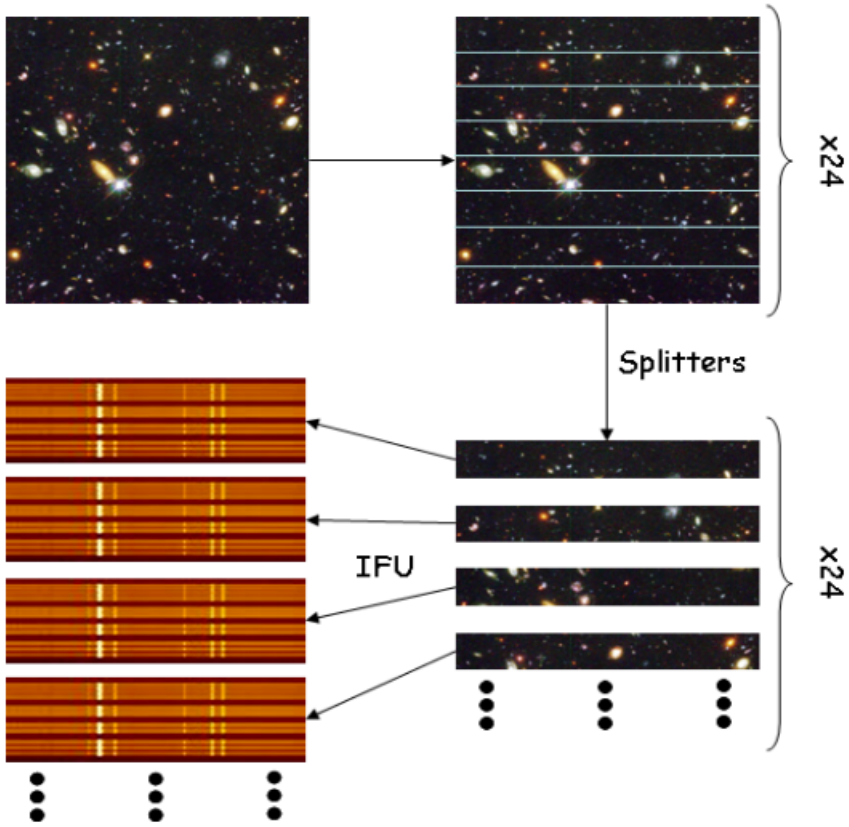

Figure 1.3: Representation of a single observation, using a slicer and 24 IFUs with one CCD sensor each. For each unit an image slicer splits the subfield into 48 slices which are aligned before entering the spectrograph. Then, the light is dispersed along an axis normal to the slices and the image is composed on a CCD matrix of 4096×4096 *pixels.*

stellar populations, chemical abundance and distribution of ionized interstellar medium, stellar and ionized-gas kinematics.
ATLAS^{3D} (Cappellari et al., 2011) concerns the study of $\sim$ 260 early-type galaxies in the local universe ($z < 0.01$). The main goal is to give a kinematically well-studied sample of early-type galaxies that can be used as the comparison one for future studies. One of the main results was the quantitative measure of the term λ_R, used to kinematically classify these galaxies in a way that is more robust than the $(V/\sigma, \epsilon)$ diagram and is nearly insensitive to projection effects. λ_R permitted a clear separation of the galaxies in two classes: slow and fast rotators. These findings were exploited in the project to improve the understanding of the structure and formation

of early-type galaxies.
Another successful galaxy survey is the Sydney-AAO Multi-object Integral Field Spectrograph (SAMI) (Croom et al., 2012) at the 4m Anglo-Australian Telescope at Siding Spring Observatory. The main goal is to make a wide survey of $\sim$ 3600 galaxies, covering a broad range in galaxy stellar mass (M_* = 10^8–10^{12} $M_\odot$) in a large range of environments. The redshift range of the survey is $0.004 < z < 0.095$. The main scientific goal of the SAMI survey is to understand the physical role of environment in galaxy evolution, the correlation between stellar mass and angular momentum and finally to identify the drivers of star formation and gas flowing in and out of galaxies.
To increase the number of targets, SDSS team proposed a new project: the Mappings Nearby Galaxies at Apache Point Observatory (MANGA) (Bundy et al., 2015) performed with IFS on the 2.5m Sloan Telescope. The targets are selected to represent the overall galaxy population with stellar masses greater than 10^9 $M_\odot$ at $0.01 < z < 0.15$. All the MANGA galaxies are selected from the SDSS main galaxy sample to exploit the known global physical and observational properties such as metallicities, morphologies, star formation rates, and stellar masses. The main purpose of MANGA is to study galaxy formation and evolution, and to be a starting point for current and future high-redshift studies.
Finally, the Fornax3D project (Sarzi et al., 2018) used MUSE to obtain integral-field spectroscopic data for the inner regions of the 33 bright ($m_B \leq 15$) galaxies within the virial radius of the Fornax cluster. The survey main goal is to study the history of early-type galaxies and the role played by environment in their evolution.

1.3 Purpose and structure of this thesis

The main goal of this master thesis work is to derive the common properties of a sample of PSB galaxies observed in the GASP survey and correlate physical and morphological quantities, such as star formation history, lines equivalent width, stellar mass, stellar population and galaxy morphological type.

In Chapter 1 I describe the main properties of PSB galaxies, as these objects are an important link in understanding the mechanisms of gas stripping in galaxies belonging to different environments. Furthermore, I introduced integral field spectroscopy and its main surveys performed with this observational technique.

In Chapter 2 I present the GASP project which is a MUSE Large Program aimed to study gas removal process in galaxies.
More specifically, in Section 2.1 I describe the GASP galaxy sample; in the Section 2.2 I discuss the MUSE instrument and in Section 2.3) I briefly describe SINOPSIS, the spectro-photometric fitting code, used to analyze star formation history of each galaxy of the sample.

In Chapter 3 I discuss our galaxy sample and the tools used to analyze the photometric and spectroscopic data. Particularly, in the Section 3.1 I focus on the description of each galaxy and its morphology. In section 3.2 I present the surface brightness profiles of the galaxies and their photometric analysis with GALFIT. In the Section 3.3 I show the SINOPSIS outputs, namely the star formation history and mass weighted age derived by analyzing their integrated spectra. The code also permits to study the equivalent widths of the spectral lines, including also an automatic routine to measure them.

In Chapter 4 I show the results for each sample galaxy. Its morphological features, star formation history and correlations between physical properties.

In Chapter 5 I discuss the main results. In the Section 5.1 I present the specific angular momentum analysis derived from ATLAS^{3D} (Emsellem et al., 2004). Moreover I show the color-magnitude diagram for the sample galaxies (Section 5.2), the phase space analysis to search common features that characterize PSB galaxies in clusters (Section 5.3), and the correlation between EW(Hβ) and galaxy stellar mass and age (Section 5.5).

In chapter 6, I summarize the conclusions of this work.

I adopt a standard concordance cosmology with $H_0 = 70$ km s^{-1} Mpc^{-1}, $\Omega_{\rm M}$= 0.3 and $\Omega_\lambda = 0.7$ all throught the thesis.

Chapter 2

The GASP project

In this Chapter I present the GASP project which is a MUSE Large Program aimed to study gas removal process in galaxies.
More specifically, in Section 2.1 I describe the GASP galaxy sample; in Section 2.2 I discuss the MUSE instrument and in Section 2.3) I briefly describe SINOPSIS, the spectro-photometric fitting code, used to analyze star formation history of each galaxy of the sample.

2.1 Description of the GASP sample

The sample is composed by eight galaxies belonging to five clusters from the GASP (GAs Stripping Phenomena in galaxies with MUSE) project.
These galaxies were included in the GASP sample because they showed a typical PSB spectrum, as observed from the fiber spectroscopy in the WIde-field Nearby Galaxy-cluster Survey (WINGS, Fasano et al., 2006; Cava et al., 2009) and OMEGAWINGS (Gullieuszik et al., 2015, Moretti et al., 2017) survey. No selection on the basis of the morphology or position in the clusters has been made.
The search for candidates of the GASP sample has been carried out on optical images of galaxies at $0.04 < z < 0.06$ belonging to WINGS (Fasano et al. 2006) and OMEGAWINGS (Gullieuszik et al., 2015) surveys for galaxies in clusters and Padova-Millennium Galaxy and Group Catalog (PM2GC, (Calvi et al. 2011) for the general field.
The WINGS survey target are 76 galaxy clusters, selected to have an X-ray luminosity between $10^{43.3} \leq L_X \leq 10^{45}$ erg s^{-1} in the redshift range $0.04 \leq z \leq 0.07$ and at $|b| \leq 20°$.
The WINGS survey field of view covered 34 arcmin $\times$ 34 arcmin, with B and

V photometry, performed with the Wide Field Camera (WFC) at the prime focus of the 2.5 m Isaac Newton Telescope (INT) at La Palma (Spain) and the WFC at the 2.2m MPG/ESO telescope at La Silla (Chile). Spectroscopic follow-ups had been carried out with the Two Degree Field (2dF) at the 3.9 m AAT situated in New South Wales (Australia) and the Wide Field Fibre Optic Spectrograph (WYFFOS) at 4.2 m William Herschel Telescope (WHT) at La Palma (Spain). The J and K imaging had been performed with the WFC at United Kingdom Infrared Telescope (UKIT) in Mauna Kea (Hawaii).
WINGS main goal is to infer the properties of a sample of nearby galaxy clusters (such as morphology, mass, and star formation history) and their correlation with cluster characteristics to better understand how galaxy evolution is influenced by environment and to save as template for high redshift studies.
OMEGAWINGS is the extension of the WINGS project, increasing to 1 square degree the field of view. Imaging was obtained with OmegaCAM at the 2.6m VLT Survey Telescope (VST), at the Paranal Observatory (Chile), while spectroscopy was done with AAOmega, at the AAT. The survey observed 46 WINGS clusters.
GASP is an ESO Large Program done with the MUSE integral field spectrograph with the goal to study gas removal processes in galaxies (Poggianti et al. 2017).
The constraints on the observations were clear conditions, moon illumination $< 30\%$, moon distance $> 30°$, and image quality < 0.9 arcsec, corresponding to less than 1 arcsec seeing at zenith. The majority of the GASP galaxies were observed with four exposures of 675 s each, each rotated by 90°. The minimum time on target is therefore 2700 s for each galaxy.
The GASP sample is mainly composed by objects that show typical signatures of ongoing gas stripping. 80% of the sample galaxies are members of a cluster, the remaining being galaxies in lower density environments. As "control sample" a number of galaxies with no apparent signature of gas removal have been also observed. These galaxies have been selected from the Poggianti et al. (2016) catalog. The eight galaxies analyzed in this thesis belong to this control sample.
The main characteristics of GASP are the following:

- Galaxy areal coverage. Thanks to the combination of MUSE large field of view (1 arcmin $\times$1 arcmin) together with its good spatial resolution ($\sim$ 1 kpc, as the scale is 0.2 arcsec/px), GASP allows to observe the main galaxy body, its outskirts and eventual tails out to $\sim 50 - 100$ kpc

away from the main galaxy component, corresponding to $> 10\ r_e$. This feature is crucial to detect extraplanar gas and stars.

- Environment. Galaxies in the GASP sample span a large range of environments, from galaxy cluster to groups, to field galaxies. The main goal of this survey is to study gas removal processes in function of environments and understand in what conditions these processes are efficient.

- Galaxy mass range. To study the gas stripping processes in the broad sample possible, GASP galaxies are in the stellar mass range $10^{9.2}$ $M_\odot < M_* < 10^{11.5}$ $M_\odot$. The study of the correlation between masses, star formation, and gas removal processes are one of GASP goals.

2.2 MUSE data reduction ad analysis

MUSE is composed by an IFU, spanning the range of wavelength from $\sim$ 4650 to 9300 Å with a mean resolution of 3000. The main parameters of the instrument are summarized in Table 2.1.
An internal correction flat is taken each night at the beginning and at the end of the observation time, to minimize the effect of temperature changes. A standard star for calibration purpose is also observed. Arcs, biases, dark, and internal and sky flats are taken daytime too. The data reduction is carried out

MUSE observational parameters	
Wavelenght range	4650 - 9300 Å
Spatial sampling	0.2 arcsec pixel^{-1}
Field of view	1×1 arcmin^2
Average resolving power	3000
Number of IFU models	24
Limiting magnitude	V_{AB} = 22.64 mag (5500 Å)
(1 hr, airmass=1.0,	R_{AB} = 22.70 mag (5500 Å)
seeing 0.8 arcsec)	I_{AB} = 22.28 mag (7849 Å)

Table 2.1

with the MUSE pipeline[1]. It had been run in a semi-automated way, since the

[1]The MUSE pipeline is available at `https://www.eso.org/sci/software/pipelines/muse/`

observations are very similar in execution and calibration. The data and the standard star frames are corrected for flat-field, wavelength-calibration and for differential atmospheric refraction.
Since MUSE field of view has a large coverage, there is >50% area for sky measurements. This is modeled from the single frames using the 20% pixels with the lowest counts. Finally, the flux is calibrated using the standard star observations.

2.3 Brief outline of SINOPSIS

To derive the main spectro-photometric properties of the galaxies, the MUSE data were analyzed with the SImulatiNg OPtical Spectra wIth Stellar populations model (SINOPSIS), that is a spectro-photometric fitting code developed by Fritz et al. (2007, 2011, 2014, 2017) and based on the routine presented in Poggianti et al. (2001).
The main SINOPSIS outputs are equivalent widths (EW) of various absorption/emission spectral lines, from ultra-violet to near-infrared wavelengths. In addition, it allows to derive several galaxy physical parameters such as stellar mass, star formation rate for given age bins, dust extinction and average age of the galaxy with associated error bars.
In a predefined set of wavelength range, SINOPSIS computes the average value of the observed flux, comparing it with a theoretical stellar population model.
In particular, the code:

- allows to treat in an age-dependent way the interstellar dust extinction;
- uses simple stellar population (SSP) models;
- instead of using a pre-compiled library of models to built a specific star formation history, it searches the best combinations of SFR and extinction values as function of the SSP age, which better reproduced given observed features in a spectrum.

SINOPSIS measures the average flux in significant portions of continuum-dominated spectral regions. Moreover the main absorption or emission lines EW, intensity, and flux are derived. With these spectral features, it searches for the model that minimizes the differences between the observed features and the model.
SSP spectra of different ages and common predetermined metallicities (sub-solar $Z = 0.04$, solar $Z = 0.02$ and super-solar $Z = 0.05$) are used to construct

the model spectrum. The age of the oldest stellar population is chosen to be as close as possible to the age of the universe at the galaxy redshift. Each SSP spectrum is weighted by a given value for the stellar mass and the extinction is applied to each one, leaving its value free to change from one SSP age to another.
In this way the parameters to search are the SFR and the extinction at each SSP age.
The model spectrum is built in the following way:

$$F_{\mathrm{MOD}}(\lambda) = \sum_{i=1}^{N_{\mathrm{SSP}}} \mathrm{SFR}(t_i) \cdot \Delta t_i \cdot F_i(\lambda) \cdot 10^{-0.4 R_V E(B-V)_i A_\lambda / A_V} \qquad (2.1)$$

where $\mathrm{N_{SSP}}$ is the number of SSP models with the same metallicity, $F_i(\lambda)$ is the i-th spectrum of the SSP, $\mathrm{SFR}(t_i)$ is the star formation of an SSP, Δt_i is the time scale for each SSP, $E(B-V)_i$ the color excess for each SSP. A_λ/A_V is the extinction curve normalized to the V band.
The combination that minimizes the differences between the observable and the model are found with an adaptive simulated annealing algorithm, that deals with non-linear problems with many parameters in a space where there are local minima. With this algorithm the associated errors of the main physical quantities, such as stellar masses, SFRs are also computed.
For each set of SSP at a given metallicity value, the code run several spectral fitting that start from a different initial parameters set. Each of these fits will result in a best-fit model, with different final parameters. A best-fit model is chosen among the SSP sets at a metallicity which gives the lowest value of χ^2.
Moreover, concerning the extinction, an approximation had been made. In general, the contribute of dust depends on SSP age, SINOPSIS treats this effect like a uniform screen, constant and independent from the target nature. This approach is a good approximation of extinction when dust and emitters can be considered uniformly mixed, i.e at large scales, over 100-200 pc (Liu et al., 2013).
The input file consists in a data-cube (in our case smoothed by 5×5 pixels) containing $N_x \times N_y$ spectra and N_z is the number of wavelengths. Moreover SINOPSIS must be provided with an input catalog with general information on the spectra, such as redshift and observed magnitudes.

SINOPSIS outputs consist in:

- a data-cube `galaxyname_out.fits`, containing information such as

stellar masses, stellar populations ages, star formation rates in different bins, galaxy luminosity and age;

- a data-cube `galaxyname_eqw.fits`, with the main lines EW, i.e. H$\beta\lambda$4861, Mg$_b\lambda$5177, NaIλ5896, H$\alpha\lambda$6563), signal-to-noise ratio, and the velocity field.

Chapter 3

The galaxy sample

In this Chapter I discuss the galaxy sample and the tools used to analyze the photometric and spectroscopic data. Particularly, in the Section 3.1 I focus on the description of each galaxy and its morphology. In the Section 3.2 I present the surface brightness profiles of the galaxies and their photometric analysis with GALFIT. In the Section 3.3 I show the SINOPSIS outputs, namely the star formation history and mass weighted age derived by analyzing their integrated spectra. The code also permits to study the equivalent widths of the spectral lines, including also an automatic routine to measure them.

3.1 Description of the galaxy sample

The galaxies of the sample (Table 3.1) were selected within the GASP sample to match the following criteria:

- to exhibit strong Balmer absorption lines in their spectra;
- not to show emission lines;
- to be cluster members.

No selection on the basis of morphology, luminosity, or mass has been made. Eight galaxies met these standards. Here, I present a brief description of the objects, grouping them by cluster membership. For all these galaxies, the data are available from the WINGS database. In particular the morphology was derived using MORPHOT (Fasano et al. 2007), an automatic procedure to morphologically classify large samples of galaxies in wide and deep fields.
In Figure 3.1 I present the images of our sample galaxies. These color images

Galaxy	z	Stellar Mass	WINGS ID	M_V	m_V	T	Morphology
A3128_B_0248	0.0603	1.93	WINGSJ032923.41-522602.9	-19.63	17.25	-0.6	S0
A3158_11_91	0.0594	1.40	WINGSJ034116.76-532400.4	-19.78	17.35	2.3	Sa/Sab
A3158_B_0223	0.0594	2.34	WINGSJ034159.82-532804.3	-19.72	17.35	2.4	Sab/Sb
A3158_B_0234	0.0594	0.71	WINGSJ034224.69-532926.1	-19.20	18.13	1.5	Sa/Sab
A500_F_0152	0.0682	0.42	WINGSJ043821.23-221302.2	-18.01	19.56	2.0	Sab
A500_22_184	0.0682	-	WINGSJ043846.40-221322.5	-18.09	19.37	2.0	Sab
A3376_B_0214	0.0463	0.77	WINGSJ060043.16-395641.4	-18.86	18.12	-0.3	S0
A1069_B_0103	0.0651	2.26	WINGSJ103936.47-085634.4	-19.70	17.47	-0.7	S0

Table 3.1: GASP name of the galaxy, redshift, stellar masses (in units of $10^{10} M_{\odot}$), WINGS name, total V-band absolute and apparent magnitudes, and morphologyfrom MORPHOT (Fasano et al. 2007).

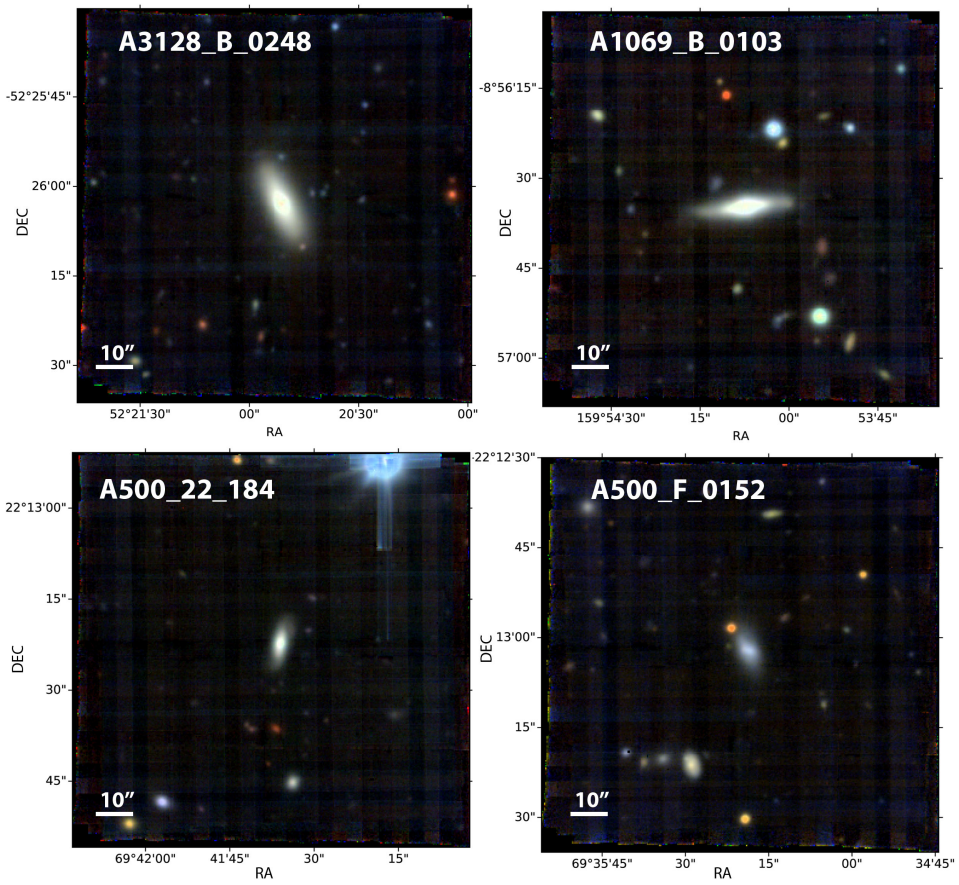

Figure 3.1: MUSE color images from MUSE data-cubes extracted in the SDSS g,r and i bands. North is up and east is left.

are obtained using the collapsed MUSE data-cubes in the g, r and i SDSS

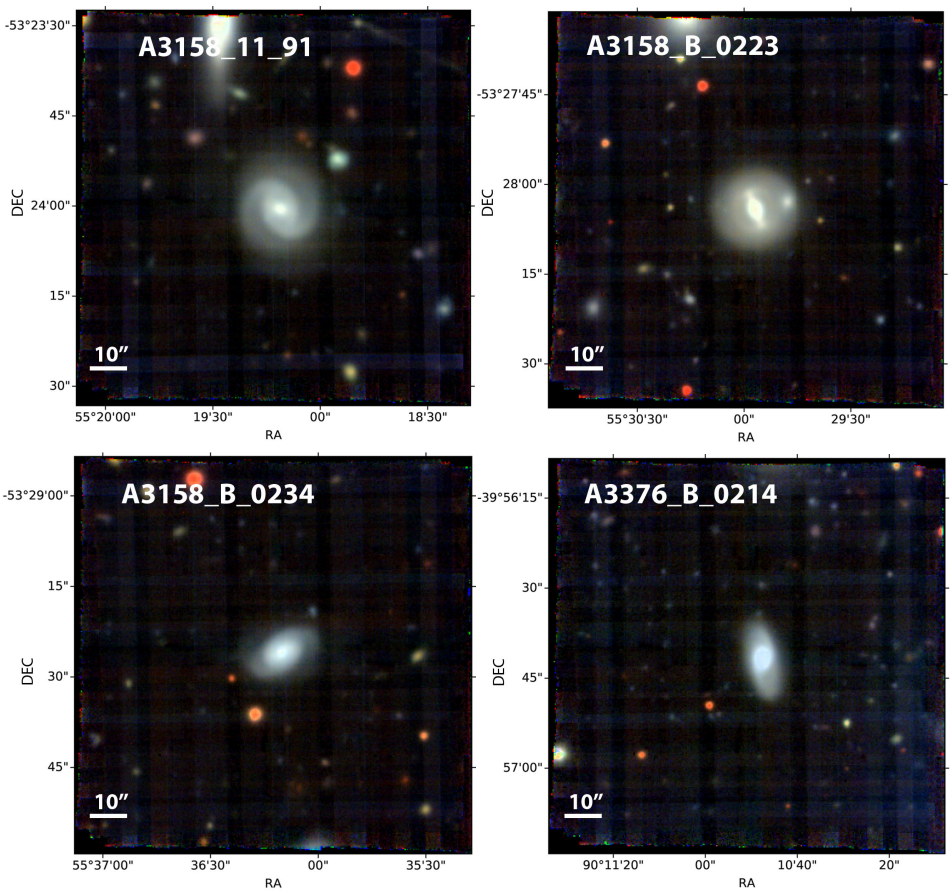

Figure 3.1: (continued)

bands.

As we can see from Figure 3.1 and table 3.1 all the selected galaxies are S0 or early spirals. Below I give a short description of each sample galaxy.

A3158_11_91, A3158_B_0223, A3158_B_0234

Three galaxies are in the cluster Abell 3158, namely A3158_11_91, A3158_B_0223 and A3158_B_0234. This cluster is part of the Shapley Concentration, first noted by Shapley (1930).
The Shapley Concentration is a supercluster of clusters in the range of redshift from ~ 0.03 to ~ 0.07. This structure is interesting for its relevance in the peculiar motion problem. It seems to be responsible for $\sim$30% of the Local Group's acceleration, and because it is one of the richest supercluster

of the sky (Zucca et al. 1993). Three clusters (A3556, A3558 and A3562) form the elongated core of this supercluster in addition to a poor one SC1329-314 (Bardelli et al. 1994).
The Shapley supercluster is in an unrelaxed dynamical state (Bardelli et al. 1994, 1998), and for this reason it is an ideal laboratory to study interactions between clusters.

A3158_11_91 and A3158_B_0223 (Figure 3.1) are seen at low inclination. A3158_11_91 presents an extended disk with evident spiral arms departing from the bulge. A3158_B_0223 seems to be more peculiar, showing a stellar halo, a lens and a bar. A3158_B_0234 is classified as an early spiral galaxy, Sa (Hubble T-Type: +1.5). Both spiral arms and a bulge are clearly visible.

A500_22_184 and A500_F_0152

A500_22_184 and A500_F_0152 (Figure 3.1) are the spiral galaxies of the sample with the latest morphological type (Hubble T-Type= +2, i.e. Sab). The two galaxies are very similar, A500_F_0152 presents a much fainter bulge.

A3128_B_0248

A3128_B_0248 is a member of the cluster Abell 3128 which is part of the Shapley Supercluster. It is a typical S0 galaxy almost edge-on with both a prominent disk and bulge (Figure 3.1).

A1069_B_0103

A1069_B_0103 is classified as S0. In the image (Figure 3.1) both the disk and the bulge are well visible.

A3376_B_0214

Some features in the large disk are visible in the image (Figure 3.1) as well as the bulge. The galaxy is a member of the Abell 3376 cluster of the Shapley Concentration.

3.2 Surface photometry

The main aim of the present section is to describe how I derived the surface brightness profiles for each object. To this purpose we used the `ellipse` task

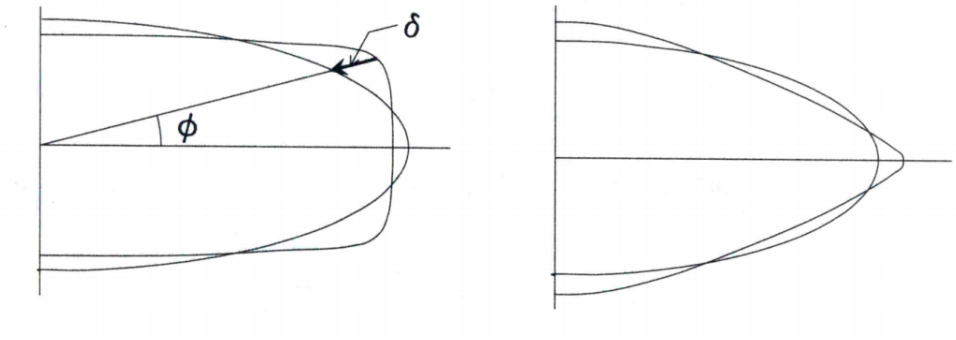

Figure 3.2: Boxy (left panel) and disky isophote (right panel) with their best-fitting ellipses. δ marks the isophote deviation from the perfect ellipse as a function of ϕ (Binney and Merrifield, 1998).

in the `isophote` IRAF package (Jedrzejewski, 1987).
`Ellipse` fits concentric ellipses to the isophotes of the galaxies. Here a brief description of how it works.
Each isophote is fitted with a predefined major axis. If the isophote is not perfectly ellipse-shaped, the Fourier analysis to describe the deviation of the isophote from the ellipse is done. If $R(\theta)$ is the coordinate that describes the isophote (with origin in its center) and (R, θ) are the polar coordinates of the ellipse, the deviation from a pure ellipse is given by a Fourier expansion (Figure 3.2):

$$\delta(\phi) = R(\phi) - R_{\rm ell}(\phi) = A_0 + \sum_{n=1}^{\infty}(A_n \cos(n\phi) + B_n \sin(n\phi)) \tag{3.1}$$

where $R_{ell}(\phi)$ describes the best-fitting ellipse, and a_n, b_n are the Fourier coefficients:

$$\begin{aligned} A_n &= \frac{1}{\pi}\int_0^{2\pi} R(\phi)\cos(n\phi)d\phi \\ B_n &= \frac{1}{\pi}\int_0^{2\pi} R(\phi)\sin n\phi d\phi \end{aligned} \tag{3.2}$$

The various Fourier terms (Figure 3.3) are defined as follow:

- A_1 and B_1 are the shift in x and y of the center coordinates of the ellipse, respectively.

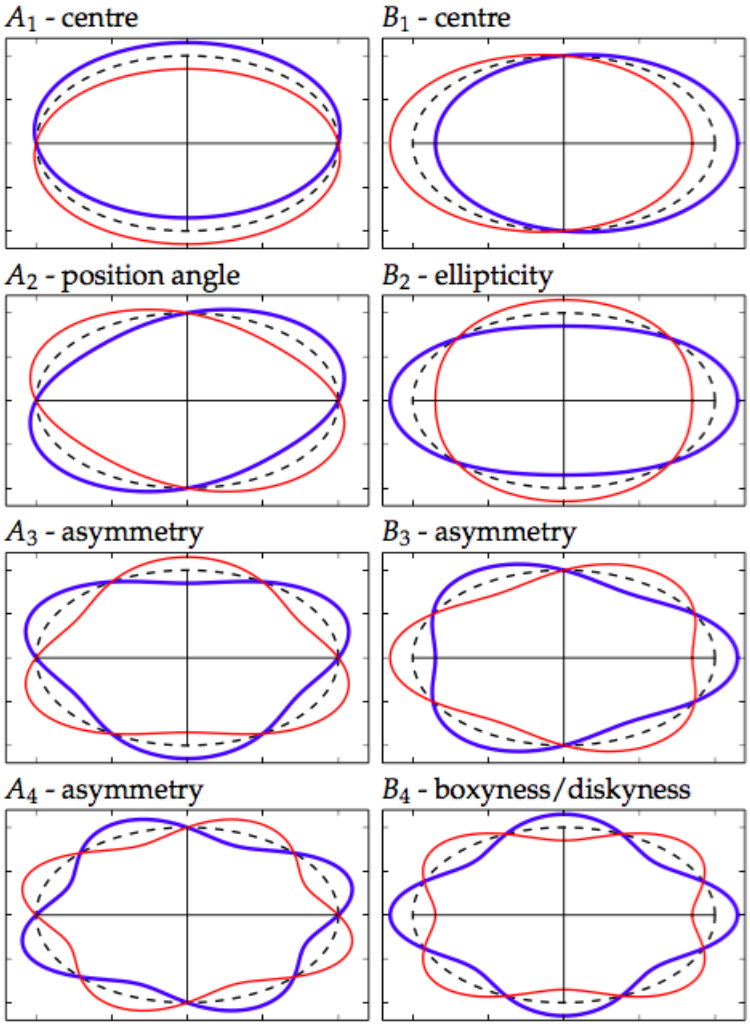

Figure 3.3: Graphic representation of the first Fourier coefficients. The blue and red lines represent negative and positive values for the coefficient, respectively. The dotted black line is the reference elliptical isophote (Ciambur, 2015).

- A_2 represents the deviation from the ellipticity of the isophote from the pure ellipse;
- B_2 represents the deviation from the position angle of the isophote from the pure ellipse;
- A_3 and B_3 provide the difference in simmetry of the x-axis and y-axis respectively;
- A_4 describes the symmetric deviations to the respect of both x and y-axis;
- B_4 describes the symmetric deviations to the respect to the center of the ellipse.

These coefficients are zero if the isophote is a perfect ellipse.
In the first place, `ellipse` starts from the initial guess, defined by the input parameters and performs the Fourier coefficients analysis described above. But it parametrizes

$$\delta(\phi) = A_0 + \sum_{n=1}^{\infty}(A_n \sin(n\phi) + B_n \cos(n\phi)) \tag{3.3}$$

so in order to analyze boxyness/diskyness of a galaxy the coefficient to take into account is A_4 and not B_4.
`Ellipse` outputs are summarized in Table (3.2). First, I get the center for each galaxy through the `imexamine` IRAF task, and the initial ellipticity and position angle from the OMEGAWINGS catalogue (Gullieuszik et al. 2015). Then I obtain the zero point for the V magnitudes, given by the expression from the MUSE pipeline:

$$V = -2.5 \cdot \log_{10}(\text{counts} \cdot 10^{-20}) - 21.098 \tag{3.4}$$

Therefore, 1 count corresponds to 28.902 mag. This allow to calibrate the magnitudes measured by `ellipse`. With these first guesses (x_0, y_0, ϵ, PA, zero point magnitude) the routine had been run. The center was left free to vary for all isophotes.
Finally, I extracted the surface brightness profile, plotting $\mu(r)$ using the expression:

$$\mu(r) = \text{MAG} + 2.5 \log_{10}(0.2^2) \tag{3.5}$$

being 0.2 arcsec pixel^{-1} the spatial scale of MUSE.

Main column parameter	Content
SMA	semi-major axis length (pixel)
INTENS	mean isophotal intensity (counts)
INT_ERR	mean isophotal intensity error (counts)
RMS	intensity mean standard deviation (counts)
ELLIP	ellipticity
ELLIP_ERR	ellipticity error
PA	position angle (degree)
PA_ERR	position angle error (degree)
X0, Y0	ellipse center (pixel)
TMAG_E	total magnitude enclosed in an ellipse (mag)
MAG	mean isophotal magnitude (mag)
MAG_UERR, MAG_LERR	lower and upper error for MAG (mag)
A4, B4	fourth armonic deviations from ellipse
A4_ERR, B4_ERR	fourth armonic deviation errors

Table 3.2: Main `ellipse` parameters for each row of the output table.

Methods and results

In order to build the one-dimensional fit of the surface brightness, I adopted a three components model, that consists of:

- a Sérsic law (or $r^{\frac{1}{n}}$ law) for the bulges;
- an exponential law for the disk;
- an eventual modified Ferrer law for the bar.

Sérsic law

The expression for the Sérsic law (Sérsic, 1963), the generalization of the de Vaucouleurs law (de Vaucouleurs, 1948) is:

$$I(r) = I_{\mathrm{e}} e^{-b_n\left(\left(\frac{r}{r_{\mathrm{e}}}\right)^{\frac{1}{n}}-1\right)} \tag{3.6}$$

which in terms of mag arcsec^{-2}, becomes:

$$\mu(r) = \mu_{\mathrm{e}} + 1.086 \cdot b_n\left[\left(\frac{r}{r_{\mathrm{e}}}\right)^{\frac{1}{n}} - 1\right] \tag{3.7}$$

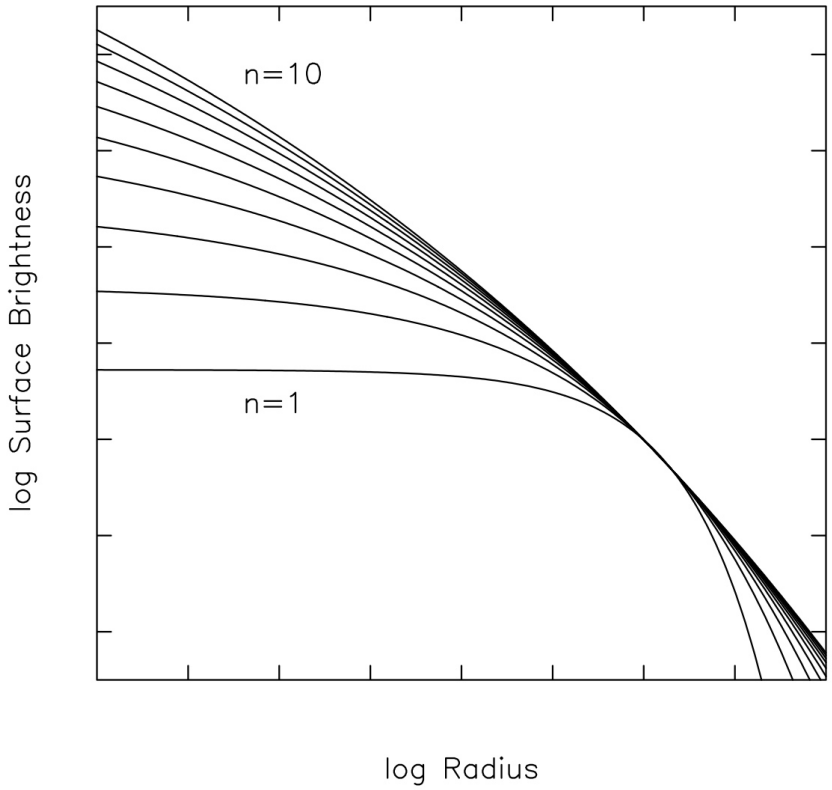

Figure 3.4: Different Sérsic profiles as a function of the value of index n.

where r_e is the effective radius, that encloses the half of the light of the galaxy, I_e is the effective surface brightness, namely the surface brightness at the effective radius ($\mu_e = -2.5 \log_{10} I_e$), n is the Sérsic index that gives the profile shape. For $n = \frac{1}{2}$ the profile is a Gaussian, for $n = 1$ it is an exponential, for $n = 4$ it is the De Vaucouleurs profile.
The Sérsic law has three free parameters: I_e, n and r_e. The coefficient b_n depends on n and it is chosen such as r_e could be the effective radius. It can be computed in a numerical way, in this work I use the approximation: $b_n = 2n - 0.324$ (Ciotti, 1991). In Figure 3.4 the Sérsic profile for different values of n.

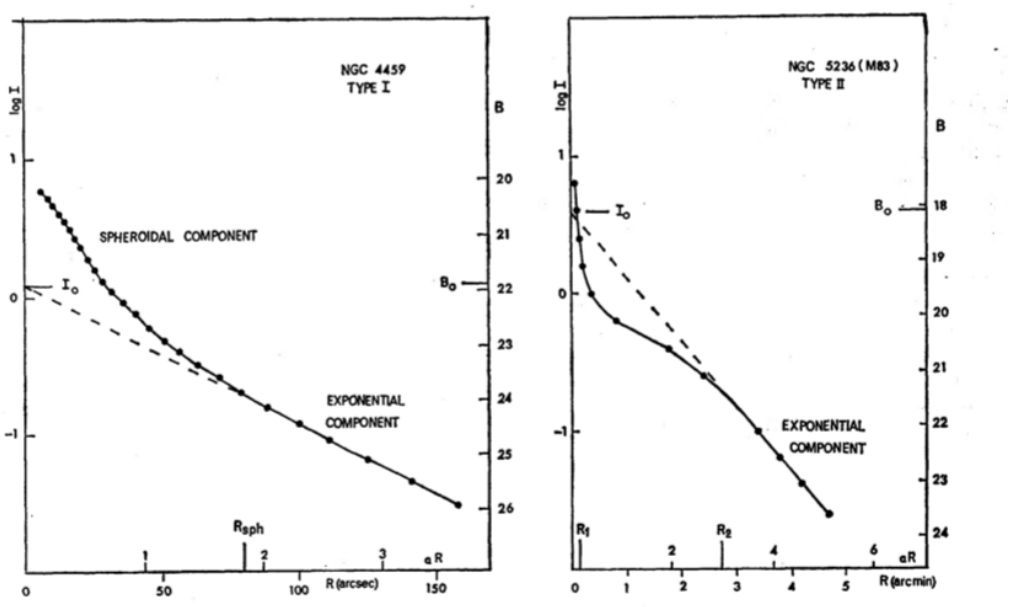

Figure 3.5: The solid line stands for the surface-brightness profile of NGC 4459 (left panel) and of M83 (right panel). The dashed line represents the exponential profile for the same galaxies(Freeman, 1970).

Exponential law

The parametric expression for the exponential law of a disk (Freeman, 1970) is:

$$I(r) = I_0 e^{-\frac{r}{h}} \tag{3.8}$$

or:

$$\mu(r) = \mu_0 + 1.086\frac{r}{h} \tag{3.9}$$

being h the scale length of the disk and I_0 the surface brightness at the center ($\mu_0 = -2.5\log_{10} I_0$). Free parameters of this power law are I_0 and h.

Modified Ferrer law

With the purpose of fitting also other components, such as a bar, I added a modified Ferrer profile (Ferrers, 1877; Peng et al., 2010):

$$I(r) = I_0\Big(1 - \Big(\frac{r}{r_{\rm out}}\Big)^{2-\beta}\Big)^{\alpha}, \tag{3.10}$$

which is defined only for $r \leq r_{\rm out}$ and is otherwise 0.
I_0 is the central surface brightness, while α and β are two parameters that

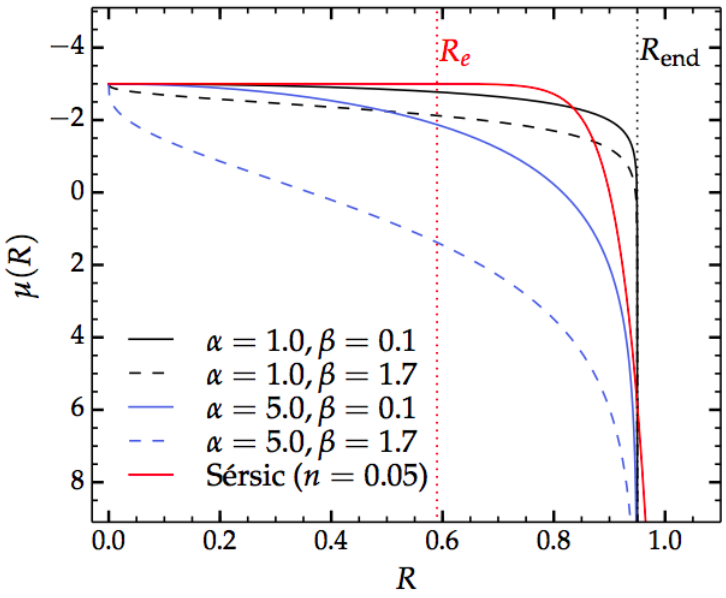

Figure 3.6: Different modified Ferrer profiles for different values of α and β compared to a Sérsic profile (Ciambur, 2016). $R_{\rm end}$ stands for $r_{\rm out}$.

describe respectively the slope of the outer truncation and central flatness of the profile. α and β are free parameters, with α ranging between 0 and 5 (Gao and Ho, 2017).

Surface brightness radial profiles

The surface-brightness radial profile for each galaxy has been fitted using a non-linear least-squares minimization and curve-fitting in Python (using `scipy.optimize`[1]).
The free parameters $I_{\rm e}$, $\rm r_e$ and n were chosen for the Sérsic law, I_0, h for the exponential one and α, β and $\rm r_{out}$ for the bar profile. Giving in input a first initial guess of these parameters, looking at the obtained profile, the routine allowed to obtain an estimated profile for the surface brightness. The error estimate was not taken into account, but it can be made using the covariance matrix and weighting the fit with the surface-brightness errors. Figure 3.7 shows the fit for the sample galaxy A3376_B_0214, and in figure 3.8 the radial profiles of position angle, ellipticity, A4 and B4 from `ellipse` output are shown.

[1]The open-source algorithm reference manual is available at the link: https://docs.scipy.org/doc/scipy/reference/tutorial/optimize.html

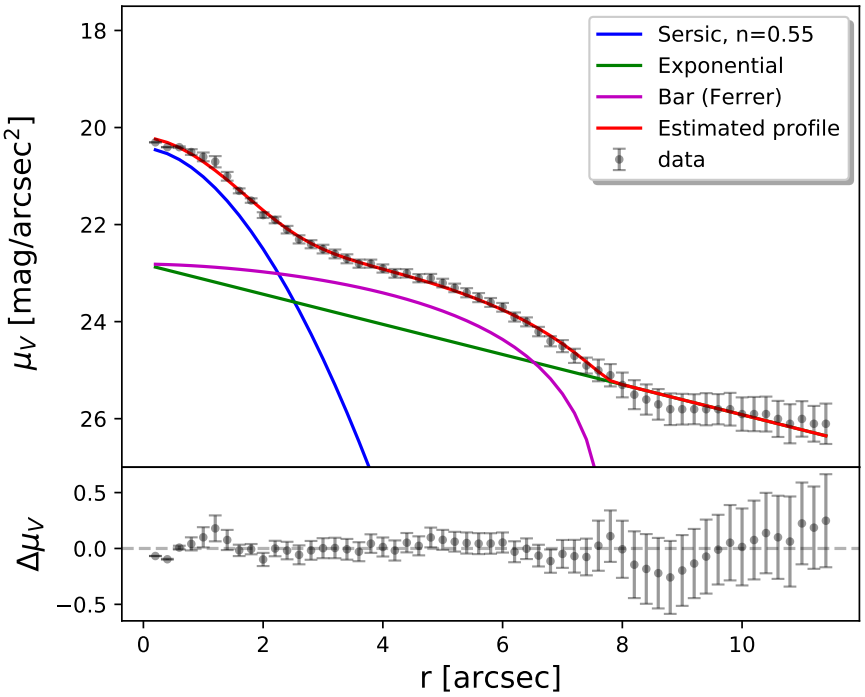

Figure 3.7: Three-component fit of the surface brightness for the A3376_B_0214 and residuals. The blue, green, and magenta lines stands for the Sérsic, Freeman, and Ferrer profiles, respectively. The red line is the estimated surface brightness profile. The best-fitting parameters are given in Table 3.4.

In the tables 3.3 and 3.4 I summarize the main results from the photometric analysis.

From the surface-brightness radial profiles (Figure 3.9) it is evident that four galaxies show a bar. They are the three members of A3158 and A3376_B_0214.

To test our procedure I decided to perform also a decomposition in pixel space directly in two dimensions. It is possible to create a two-dimensional model of the galaxy and subtracting it to the image. In this way structures that do not belong to the fitted profiles stand out in the residual map. To this aim, I used GALFIT (Peng et al. 2002), a two-dimensional fitting algorithm to perform photometric decomposition.

I preferred to use only one component for the two-dimensional fit to allow GALFIT to converge. The single Sérsic profile to run the GALFIT code was taken from the GASPHOT database (Table 3.5). GASPHOT (Pignatelli et al., 2006) is a tool for automatic galaxy photometry. Its primary goal is to extract reliable estimates of the main photometric and structural parameters

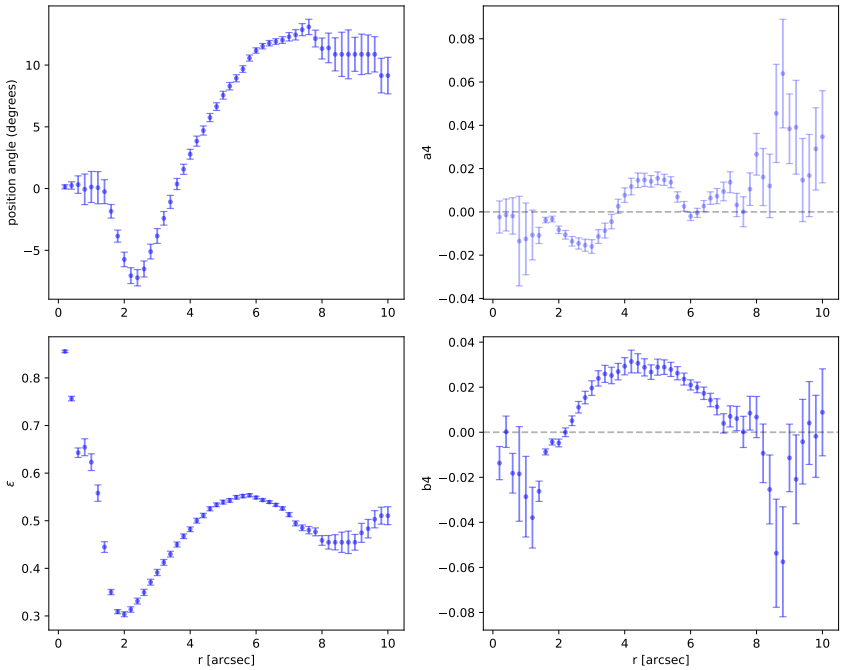

Figure 3.8: Radial profiles of the position angle, ellipticity, A4 and B4 for A3376_B_0214, from `ellipse`.

of large samples of galaxies from wide or deep field images and it fits a single Sérsic law to the light distribution of galaxies.
I fitted with GALFIT all the sample galaxies with a Sérsic profile . From the GALFIT outputs (Figure 3.11, 3.11), six galaxies have a bar and some have structures like spiral arms (for instance A3158_B_0234). Thanks to this analysis I suspect the presence of a faint bar in two more galaxies.
A second check had been made to test the accuracy of the 1D surface brightness fit. I fitted the profiles with a single Sérsic and entered these parameters into GALFIT routine too. An example of output image, model and residuals map is in figure 3.10.
Among eight galaxies, A3128_B_0248 and A1069_B_0103 have consistent residuals in the center, but I have no evidence of the presence of a bar. Finally, I made a test with the IRAF routine `bmodel`, that build a model from the `ellipse` output. Particularly, `bmodel` task creates a two-dimensional image file containing a noiseless photometric model of a source image. In our case the V-band image, in which I performed the photometric analysis. In Figures 4.2, 4.19, 4.24, 4.29 I show the V-band image, the model image and the residual image from `bmodel`. The model is

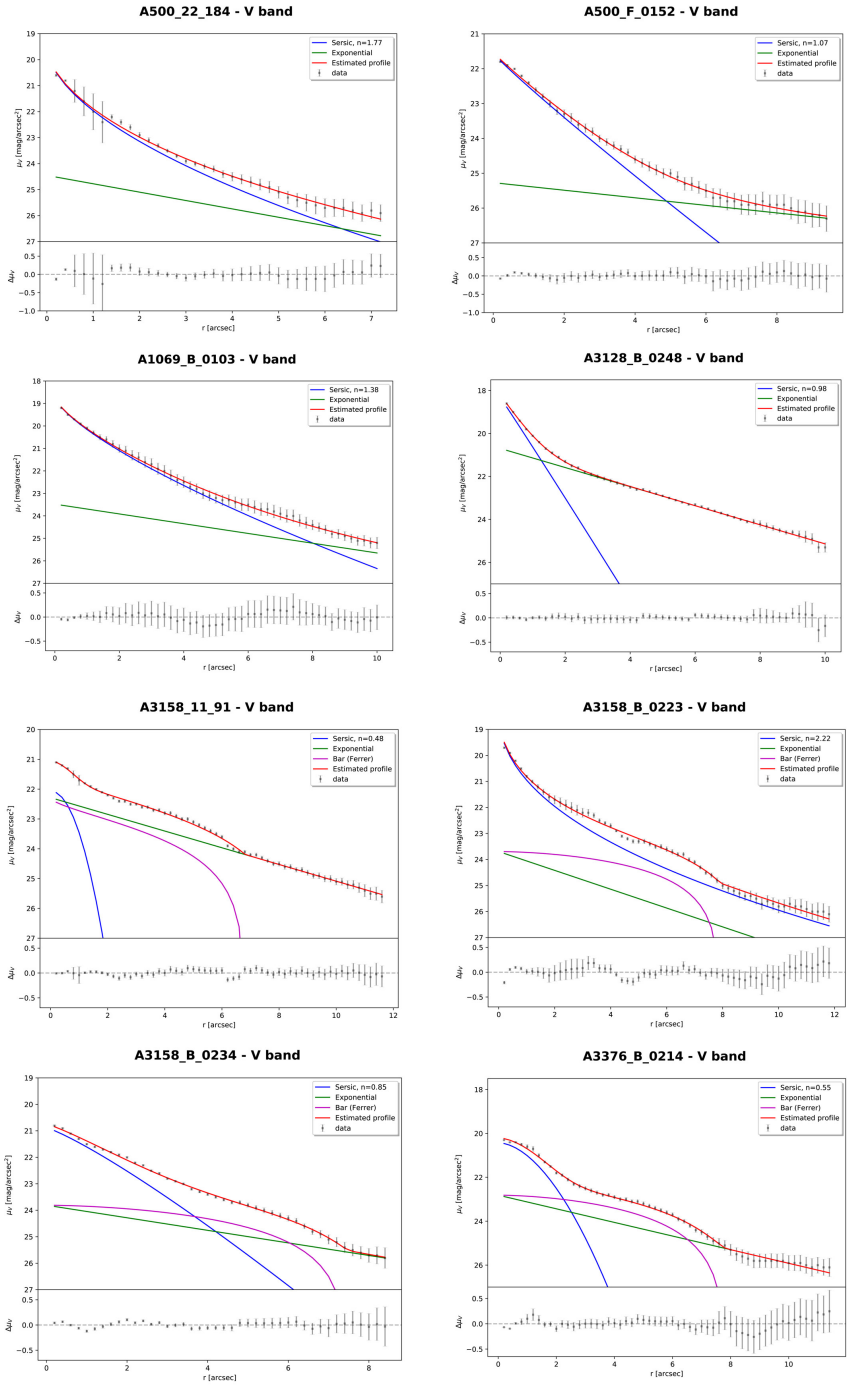

Figure 3.9: Photometric decomposition of all the sample galaxies. Best-fitting parameters are given in Table 3.4. The blue, green, and magenta lines stands for the Sérsic, Freeman, and Ferrer profiles, respectively. The red line is the estimated surface brightness profile.

Galaxy	b/a	ϵ	PA (degree)	m_V	i (degree)
A3128_B_0248	0.52	0.48	24.0	17.25	60.67
A3158_11_91	0.85	0.15	26.0	17.35	32.52
A3158_B_0223	0.9	0.10	19.0	17.35	26.42
A3158_B_0234	0.70	0.30	-66.0	18.13	46.80
A500_F_0152	0.67	0.33	22.0	19.56	49.26
A500_22_184	0.34	0.66	-15.0	19.30	73.70
A3376_B_0214	0.53	0.47	10.0	18.12	59.94
A1069_B_0103	0.41	0.59	-84.0	17.47	68.58

Table 3.3: Semi-axis ratio, ellipticity, position angle, total V apparent magnitude and inclination of the sample galaxies from the `ellipse` *output. The inclination has been derived from the observed axis ratio with the relation* $\cos^2 i = ((b/a)^2 - q^2)/(q^2 - 1)$ *assuming an intrinsic flattening* $q = 0.2$ *(Hubble, 1926, Holmberg, 1946).*

Galaxy	r_e (arcsec)	μ_e (mag arcsec^{-2})	n	μ_0 (mag arcsec^{-2})	h (arcsec)	r_{out} (arcsec)	α	β
A3128_B_0248	0.78	20.10	0.98	20.70	2.44	-	-	-
A3158_11_91	0.70	22.75	0.48	22.29	3.87	6.82	1.00	1.43
A3158_B_0223	2.94	22.68	2.22	23.70	3.00	7.92	1.00	0.30
A3158_B_0234	1.84	22.38	0.85	23.81	4.58	7.49	1.11	0.30
A500_F_0152	0.23	19.42	1.07	28.00	3.02	-	-	-
A500_22_184	1.85	22.99	1.77	24.45	3.37	-	-	-
A3376_B_0214	1.21	21.55	0.55	22.81	3.50	7.86	1.43	0.30
A1069_B_0103	2.30	21.36	1.38	23.48	5.00	-	-	-

Table 3.4: Best-fitting parameters for the bulge, disk, and bar obtained from the photometric decomposition of the sample galaxies.

built from the results of isophotal analysis generated by `ellipse`. I found the presence of a central component in both galaxies, that I can probably interpret as an inner small bar.
Finally, I run `bmodel` on the two galaxies without a visible central component (A500_22_184 and A500_F_0152), confirming the GALFIT analysis of the lack of a central morphological feature (figures 4.19, 4.24).
From the morphological point of view, 50% of our PSB galaxies show a bar. Bars are a common morphological feature in galaxies. Nair and Abraham (2010) found that among disk galaxies, the 30% present an evident bar, and this morphological feature correlates with the environment, star formation history, and redshift of the object. In fact the fraction of barred spiral galaxies is strongly dependent on the mass and star formation history of

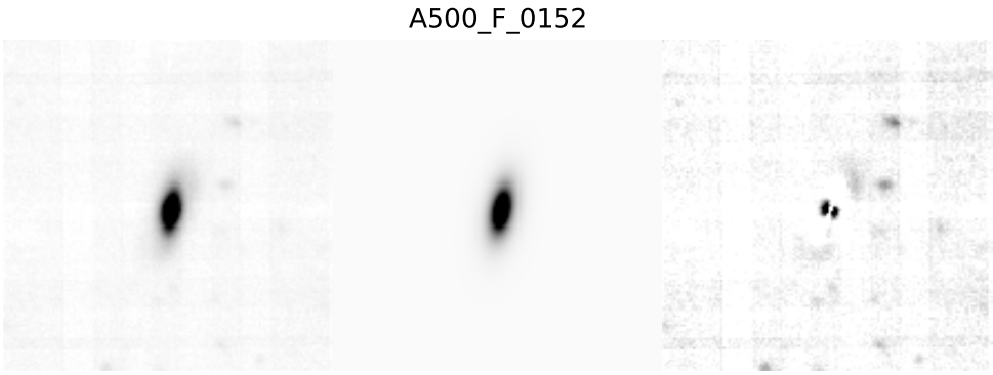

Figure 3.10: GALFIT outputs for A500_F_0152 fitting the galaxy image with a single Sérsic profile. The model image (central panel) and residual map (right panel) are consistent with GASPHOT data.

galaxies. In our sample the fraction is higher but the small sample I analyzed does not allow us to draw definitive conclusions.

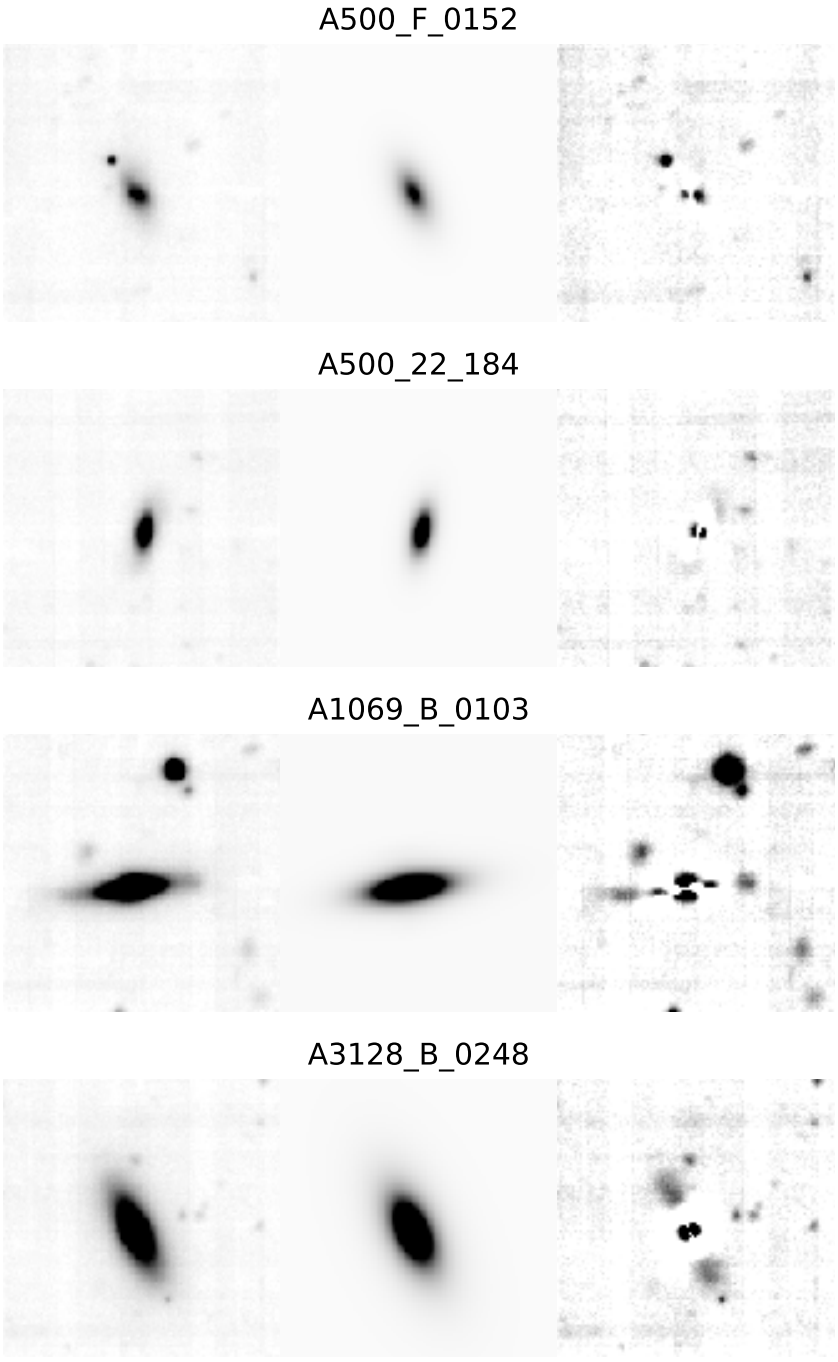

Figure 3.11: GALFIT output for the sample galaxies, showing the V-band image of the galaxy (left panel), two-dimensional best-fitting model obtained using a Sérsic profile (central panel), and residual map (right).

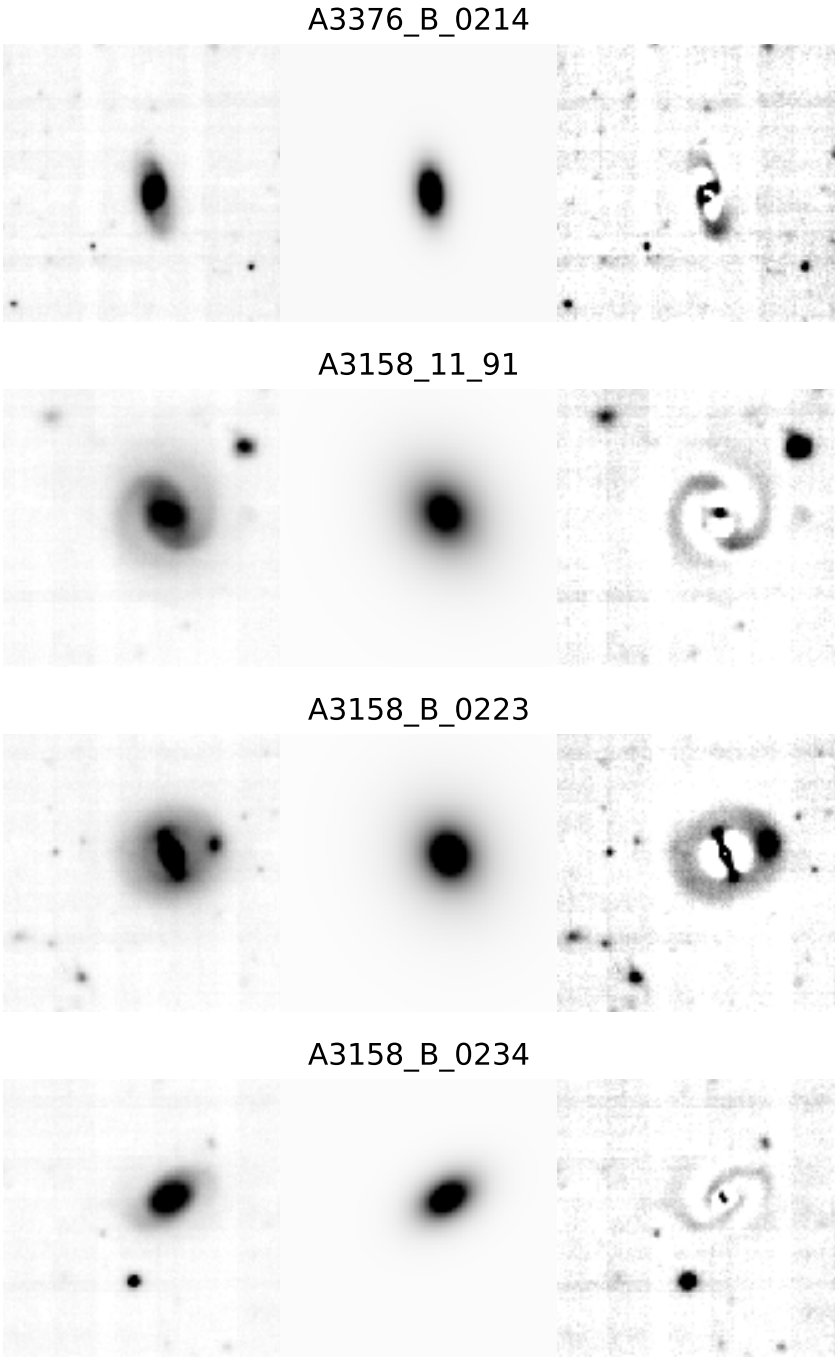

Figure 3.11: (continued)

Galaxy	r_e (arcsec)	μ_e (mag arcsec^2)	n (GASPHOT input)	n (GALFIT output)
A3376_B_0214	2.33	21.092	1.58	1.38
A3128_B_0248	2.22	19.942	3.51	3.04
A3158_B_0234	3.01	21.733	1.11	0.97
A3158_11_91	4.76	22.433	1.24	1.18
A500_F_0152	2.17	22.474	1.80	1.60
A3158_B_0223	4.90	22.294	3.60	3.77
A1069_B_0103	1.98	19.329	2.04	1.82
A500_22_184	2.17	22.474	1.79	1.68

Table 3.5: Guess parameters of the single Sérsic profiles from GASPHOT database entered as input into the GALFIT code.

3.3 Analysis of SINOPSIS data

As I pointed out at the beginning of this chapter, PSB galaxies show no emission lines and have strong absorption Balmer lines. Since these galaxies do not have emission lines, the only ones present in the SINOPSIS output are H$\beta\lambda$4861.3, Mg$_b\lambda$5176.7and NaIλ5895.6, H$\alpha\lambda$6562.8. These lines are of strong interest for their correlation with the star formation history of the sample galaxies.
From the data-cube output, I extract these four slices, masked the pixels with inconsistent values (negative values in SINOPSIS outputs are indicative of emission lines, but in our case these outputs are "noise" measurements) and bad pixels data. In Figure 3.12 I show an example of the typical SINOPSIS outputs for these lines for the galaxy A3376_B_0214.
Moreover, SINOPSIS had been run twice on each galaxy. First a mask applied on the image included all MUSE field of view. In the second run, the area to be fitted was restricted to the body of the galaxy, and the number of fits that have been made for each spectrum are increased by $\sim$10 times, in order to more carefully derive the uncertainties (fig. 3.13).

3.3.1 Error budget

In order to analyze the SINOPSIS outputs as the maps of EW(Hβ) in Figure 3.14), I tested the consistency of the errors given by the routine on the 5×5 pixels smoothed data-cube spectra. SINOPSIS returned errors for each computed EW (Figure 3.15), A sample of spaxels had been chosen to check if

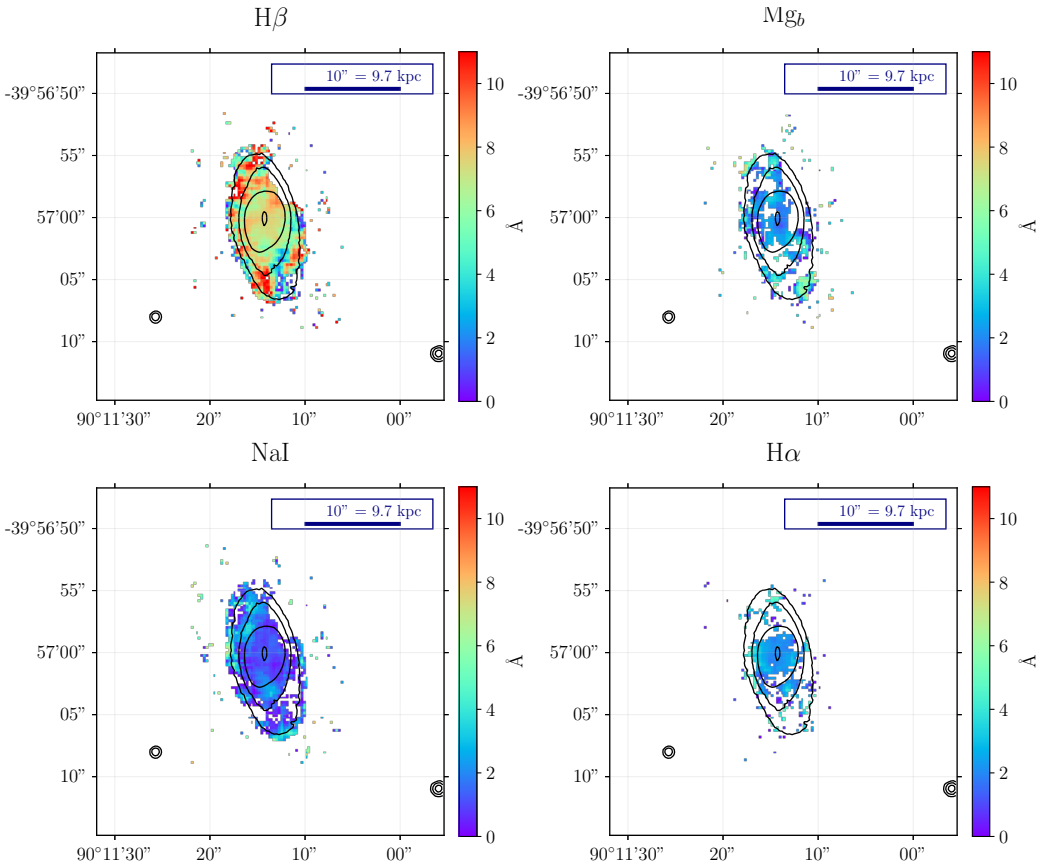

Figure 3.12: Equivalent widths of Hβ, Mg$_b$, NaI and Hα for the sample galaxy A3376_B_0214. Negative values and bad pixels data were masked.

SINOPSIS results were consistent by meaning the EWs by hand using IRAF task `splot`.

I used the `e+e` command of `splot` to measure the equivalent widths of Hβ and Hα. This test was made on the sample galaxy A3376_B_0214. With `e+e` I marked two continuum points around the line to be measured. The linear continuum is subtracted and the flux is determined by adding the flux of the pixels in these limits. Returned values are the line center, continuum at the region center, core intensity, flux above or below the continuum, and the equivalent width. I chose three areas of 5x5 spaxels and I displayed the 25 corresponding spectra. The chosen areas were the center where S/N is higher, a region close to the center, and a more external one where the S/N ratio is lower. For each one, I measured the Hβ and Hα lines equivalent widths with

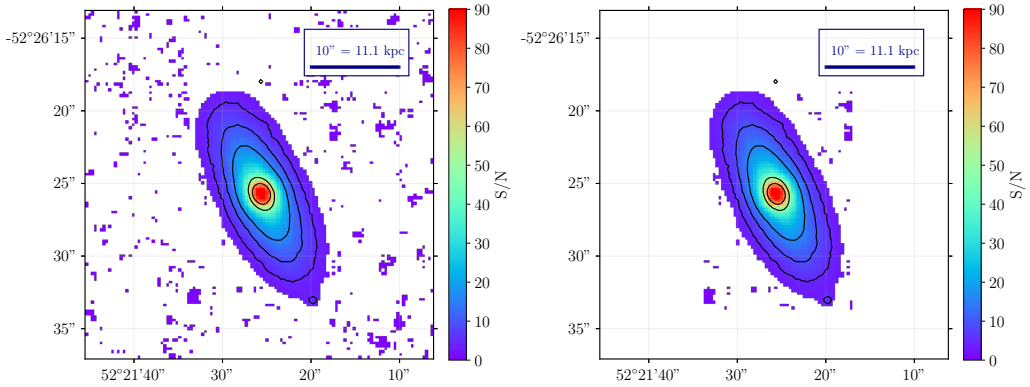

Figure 3.13: Signal-to-noise (S/N) ratio map for A3128_B_0248. Left panel: SINOPSIS first run, with a mask applied on the whole MUSE field of view. Right panel: SINOPSIS second run with a rectangular mask centered on the galaxy.

`e+e` task and I plotted the resulting values versus SINOPSIS outputs (Figure 3.17. Figure 3.18 shows a spectrum in a region close to the center in the magenta area of the Figure 3.16. Strong Balmer absorption lines are present and a continuum decrement towards the red part of the spectrum, as I expect from a PSB galaxy spectrum.
To better understand which kind of spaxels I displayed, I highlight also the S/N ratio (Figure 3.15), which ranges from ~ 30 to 100 in the central galaxy region.
SINOPSIS errors are consistent with the `splot` estimate. The SINOPSIS error is ± 2 Å. However there seems to be a trend. In fact the EW measured in the spaxels with higher S/N tend to be overestimated by SINOPSIS with respect to the measure made by hand.
Hα line is in general fainter than Hβ and in a more noisy region, for this reason I used only EW(Hβ) to characterize our galaxies.

With the purpose of exploiting EW(Hβ) as an indicator of the presence of younger stars, I computed the mean of its value in a circle, with origin in the center of the galaxy and r_e as radius. The results are in the Table 3.6.

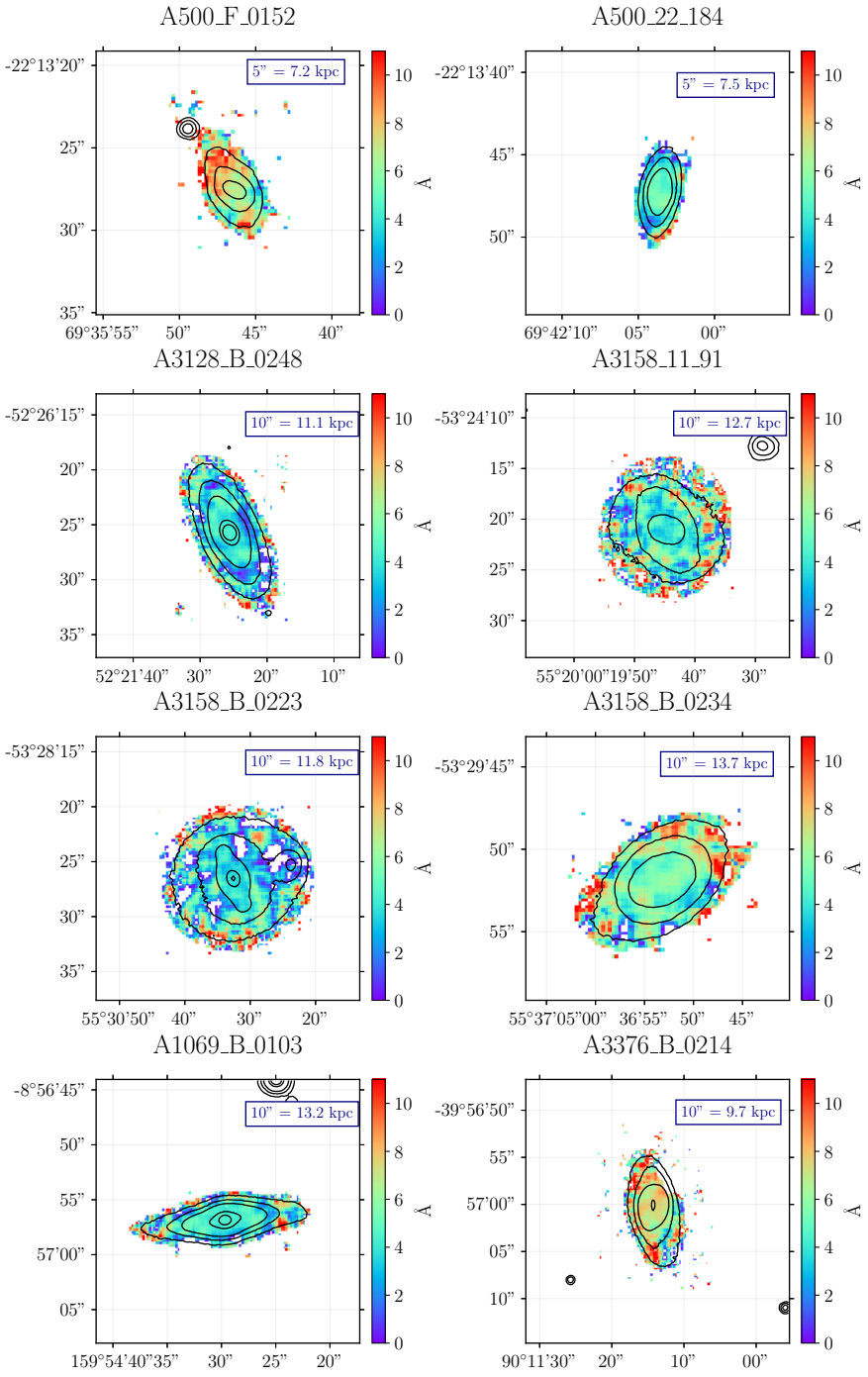

Figure 3.14: Maps of EW(Hβ) for all the sample galaxies, from the SINOPSIS. Negative values and bad pixel data have been masked.

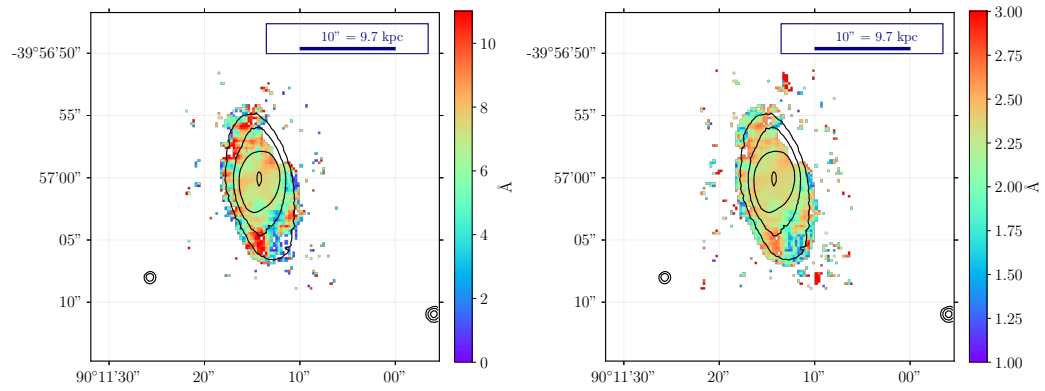

Figure 3.15: Map of EW(Hβ) (left panel) and corresponding error (right panel) for the sample galaxy A3376_B_0214 from SINOPSIS.

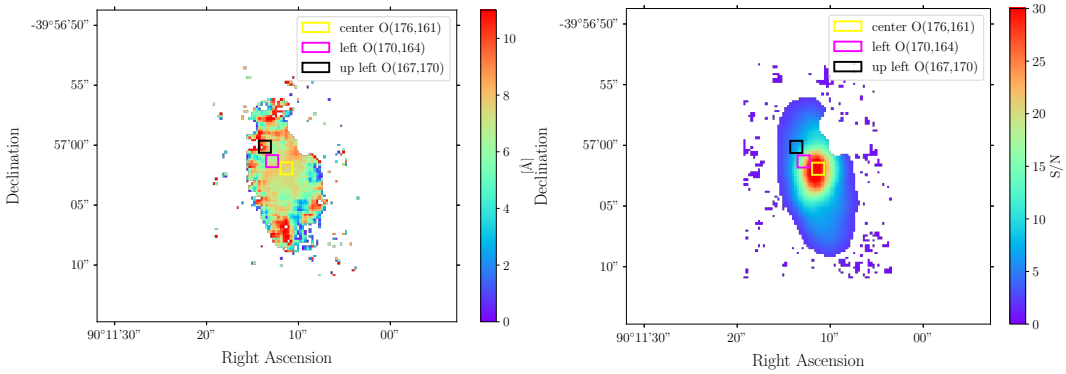

Figure 3.16: Map of the EW(Hβ) (left panel) and S/N (right panel) for A3376_B_0214. The colored squares are the areas where the test of the EW estimate was made. The coordinate of the selected region are given in the legend.

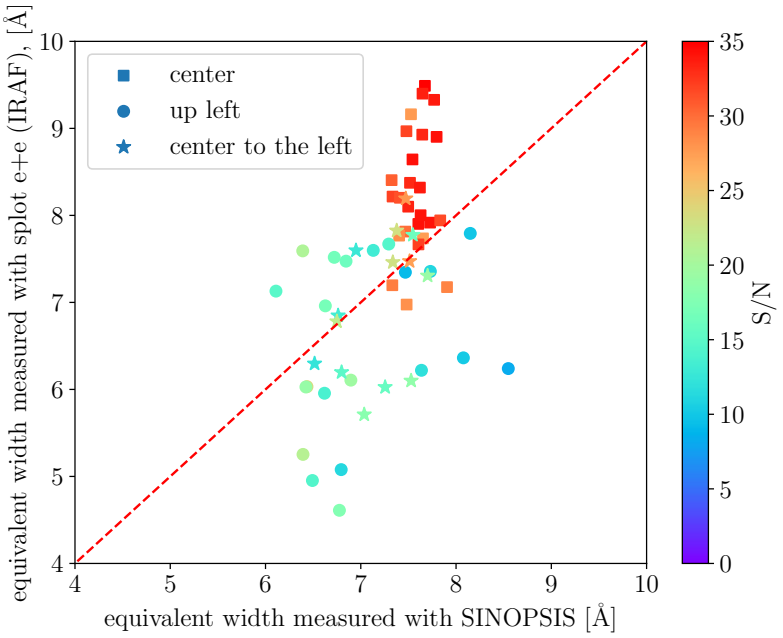

Figure 3.17: Correlation plot of the EW(Hβ) measured with SINOPSIS (x-axis) and `splot e+e` task (y-axis). The dashed red line stands for 1:1 correspondence.

Galaxy	EW(Hβ) mean (Å)	EW(Mg$_b$) mean (Å)
A3128_B_0248	3.54±1.02	4.33±0.62
A3158_11_91	4.71±1.80	3.34±1.19
A3158_B_0223	3.60±1.73	4.45±1.43
A3158_B_0234	5.46±1.51	2.86±0.92
A500_F_0152	6.61±2.07	2.70±1.39
A500_22_184	4.28±1.48	2.87±1.09
A3376_B_0214	7.08±0.93	2.13±0.68
A1069_B_0103	4.03±1.16	3.56± 0.91

Table 3.6: Mean and standard deviation for EW(Hβ) and EW(Mg$_b$) in a circular area centered on the galaxy nucleus with radius r_e.

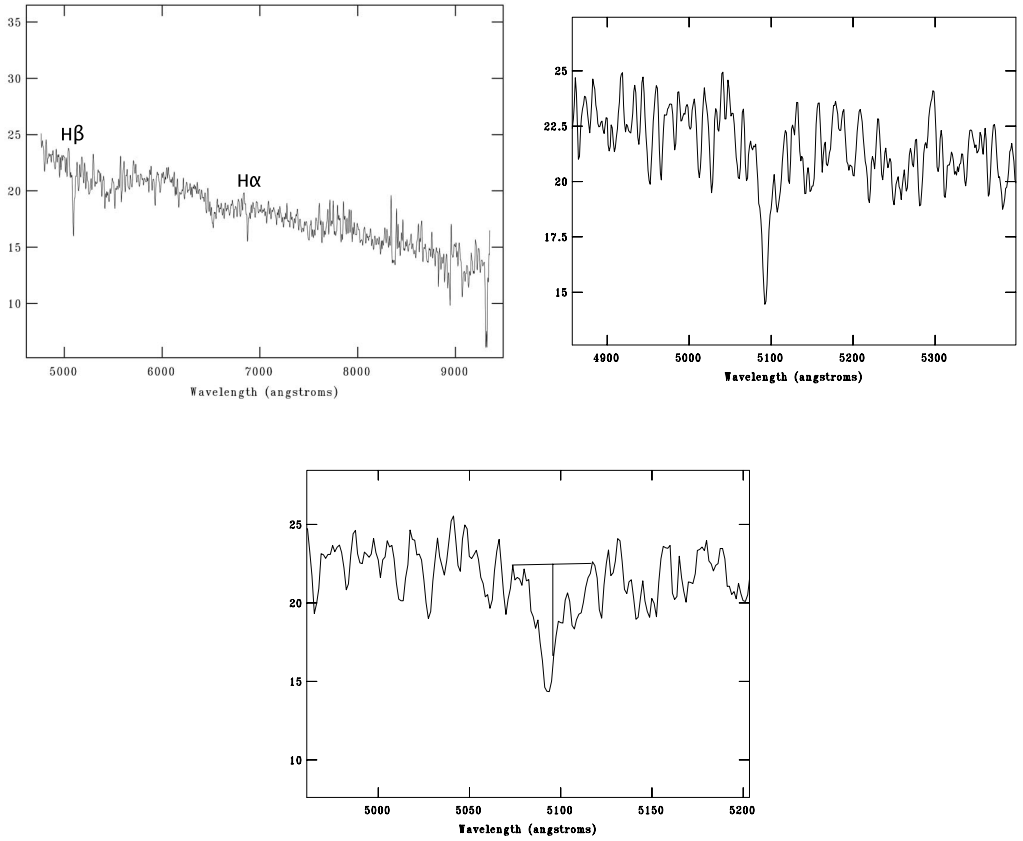

Figure 3.18: Top left panel: spectrum of A3376_B_0214 taken from the region labelled in magenta in Figure 3.16. Strong absorption lines are present, as well as a continuum decrease towards the red region of the spectra. Top right panel: Region of the spectrum of Hβ absorption line. Bottom panel: `e+e` task from IRAF `splot` applied on the 5×5 spectrum.

3.3.2 EW(Hβ) radial profiles

To put in contest the values obtained by SINOPSIS we need to know which is the theoretical value of the EW(Hβ) expected for our SSP synthetic spectra. Figure 3.19 shows EW(Hβ) as a function of the stellar age for SSP synthetic spectra (J. Fritz, private communication). We note that the peak for EW(Hβ) corresponds to about 0.87 Gyr. This value decreases for older or younger stellar populations. A typical k+a galaxy must have an EW larger than $\sim$3.5 Å, as is the case for all our galaxies.

To compare distribution of the younger stellar populations for each sample galaxy, I estimated the EW(Hβ) profile. To derive the profile, I masked each Hβ map with a circular aperture centered in the center of the galaxy. Next, I calculated the average of Hβ in the circular annulus between one aperture and another. Thus, the EW(Hβ) radial profile was obtained for each galaxy and all the profiles are shown in Figure 3.20. All the plots are obtained only for region of the galaxy with $S/N > 5$.

3.3.3 Star formation history

The star formation hystory (SFH) of a galaxy is its star formation rate as a function of cosmic age.

SINOPSIS provides an output to estimate SFH. Only the 12 age-bin averaged spectra are provided, letting free to vary star formation rate (SFR) and extinction in function of the color excess. In this pattern, 12 different ages of different SSP averaged spectra are used, the ages range from 10^5 to $1.4{\cdot}10^{10}$ yr (Table 3.7).

Within an age bin the spectra have similar characteristics (colours, EW and Balmer decrement). SFR and extinction are parametrized by means of the color excess $E(B-V)$, and let free to vary. The observed intensity of hydrogen lines are used to calculate the SFR and amount of dust extinction. Fritz et al. (2017) reproduced these observables with a theoretical spectrum to give constraints on these two quantities. They found a good agreement when considering a Chabrier (2003) initial mass function, recalibrated with the more recent work of Kennicutt and Evans (2012).

Using the data of WINGS dataset, Fritz et al. (2007) showed that four age bins (young, young-intermediate, intermediate-old and old) are the most representative of data considering the typical S/N of these spectra. In particular the bins corresponds to:

- young: up to $2.0{\cdot}10^7$ yr;

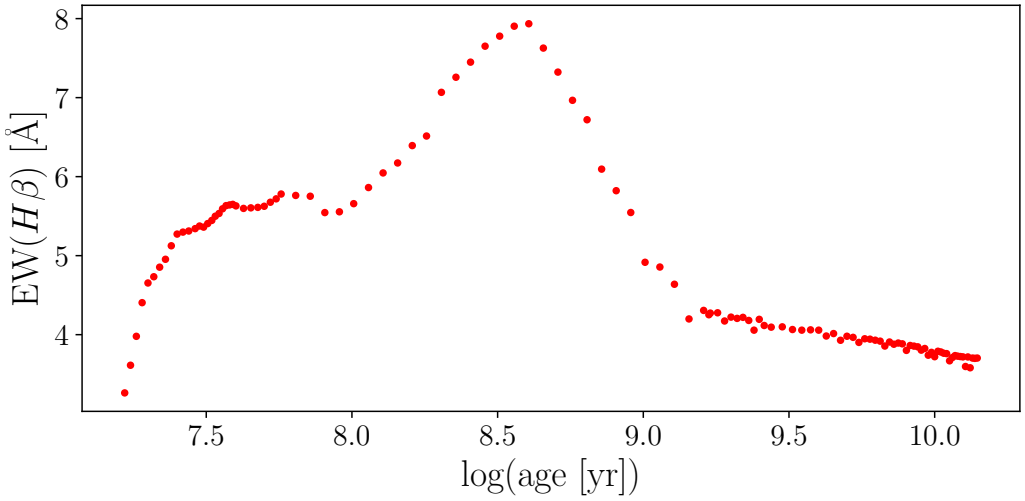

Figure 3.19: EW(Hβ) vs stellar age. High values of EW(Hβ) ($\geq$ 3.5 Å) are consistent with a younger population ($\leq$ 1 Gyr). These data were obtained by J. Fritz (private communication) and computed manually on SSP synthetic spectra.

Age-bin	initial time (Gyr)	final time (Gyr)
1	0	0.002
2	0.002	0.004
3	0.004	0.007
4	0.007	0.02
5	0.02	0.06
6	0.06	0.20
7	0.20	0.57
8	0.57	1.01
9	1.01	3.00
10	3.00	5.75
11	5.75	10.00
12	10.00	14.00

Table 3.7: Predefined age-bins of SINOPSIS.

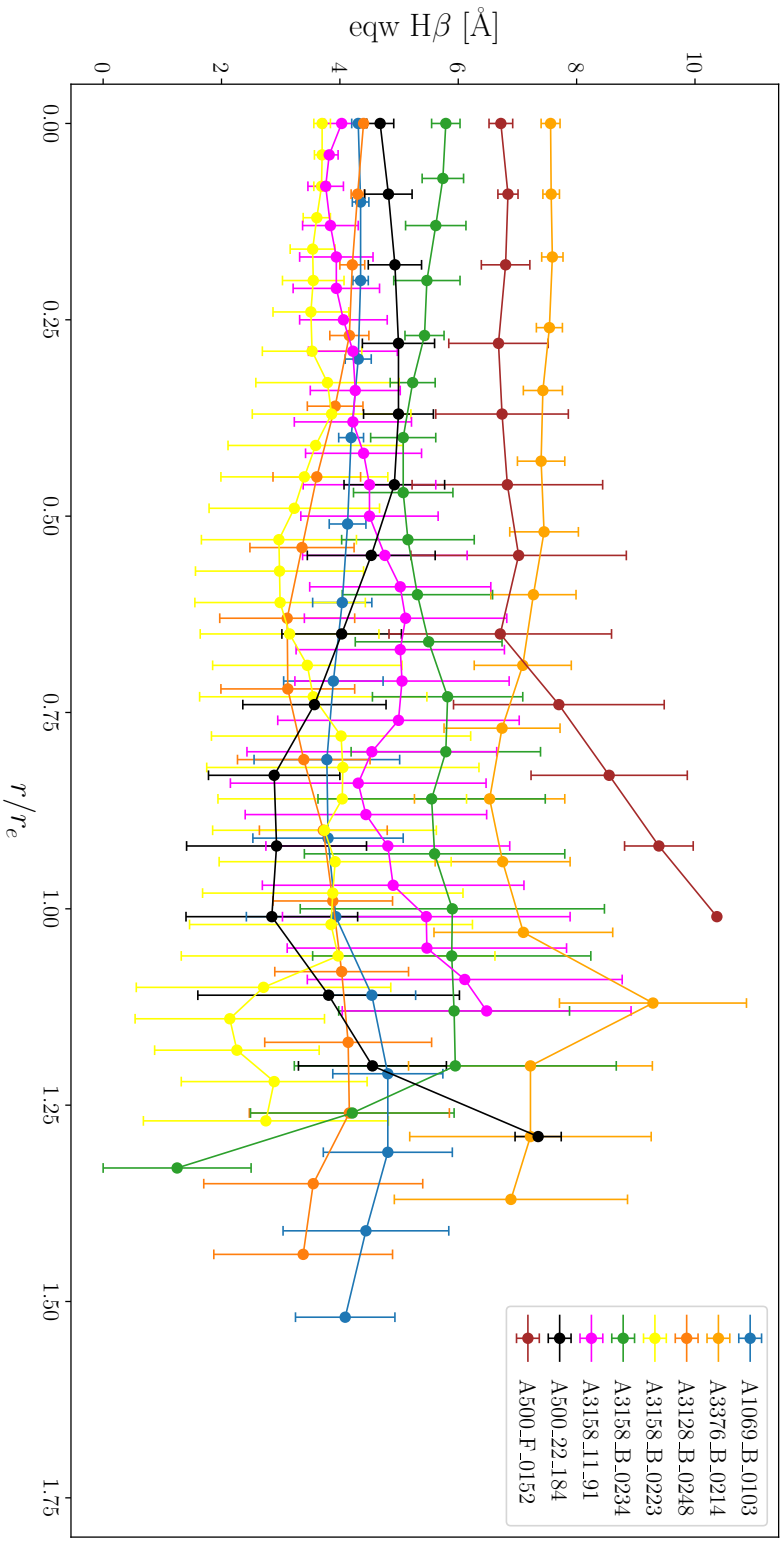

Figure 3.20: EW(Hβ) radial profiles for the sample galaxies. Error increases with decreasing S/N which is smaller than 5 close to r_e

.

- young-intermediate: from $2.0{\cdot}10^8$ yr to $5.7{\cdot}10^8$ yr;
- intermediate-old: from $5.7{\cdot}10^8$ yr to $5.7{\cdot}10^9$ yr;
- old: from $5.7{\cdot}10^9$ yr to $1.4{\cdot}10^{10}$ yr.

I plotted for each galaxy the four age bins of SFR. By focusing my analysis in the central region of each galaxy, I note that all of them had a second burst in earlier epochs, that is probably responsible of the presence of relatively young stars (Figure 3.21). For example, A3376_B_0214 had a burst between $\sim 2{\cdot}10^8$ yr to $5.7{\cdot}10^8$ yr ago.

To decrease the uncertainty of the time in which the starburst occurred, I plotted the 12 SFR age bins too (figure 3.22). We can notice how the SFH of A3376_B_0214 is more articulated in the cosmic time. The starburst responsible of the presence of relatively young stars occurred $2.0 \cdot 10^8$ yr $\leq t \leq 5.7 \cdot 10^8$ yr ago.

3.3.4 Luminosity and mass weighted ages

SINOPSIS estimates also the average age of a galaxy, weighting it on the stellar populations that compose its spectrum. It is well known that a blue spectrum will give a different mean age than a red one, since the more massive younger stars emit preferentially at bluer wavelengths, i.e. the mass-to-light ratio has a correlation with the age (Ferreras and Silk, 2003). There are two ways to break this degeneracy, using the mass-weighted age and luminosity-weighted age (Wuyts et al., 2007). The first requires the mass distribution in function of stellar age, the second is derived from the spectrum. The mass-weighted age will be higher than the luminosity-weighted age because the most massive stars are also the youngest, and the brightness, unlike the mass, is a non-linear quantity.
In SINOPSIS the luminosity-weighted age is defined as:

$$\left\langle \log(T) \right\rangle_L = \frac{1}{L_{\mathrm{TOT}}(V)} \cdot \sum_{i=1}^{N_{\mathrm{SSP}}} L_i(V) \cdot \log(t_i) \tag{3.11}$$

where $L_i(V)$ and $L_{\mathrm{tot}}(V)$ are the rest-frame V band luminosities of the i-th SSP and of the total spectrum and t_i the age of the i-th SSP. Similarly, the mass-weighted age is:

$$\left\langle \log(T) \right\rangle_M = \frac{1}{M_{\mathrm{TOT}}(V)} \cdot \sum_{i=1}^{N_{\mathrm{SSP}}} M_i(V) \cdot \log(t_i). \tag{3.12}$$

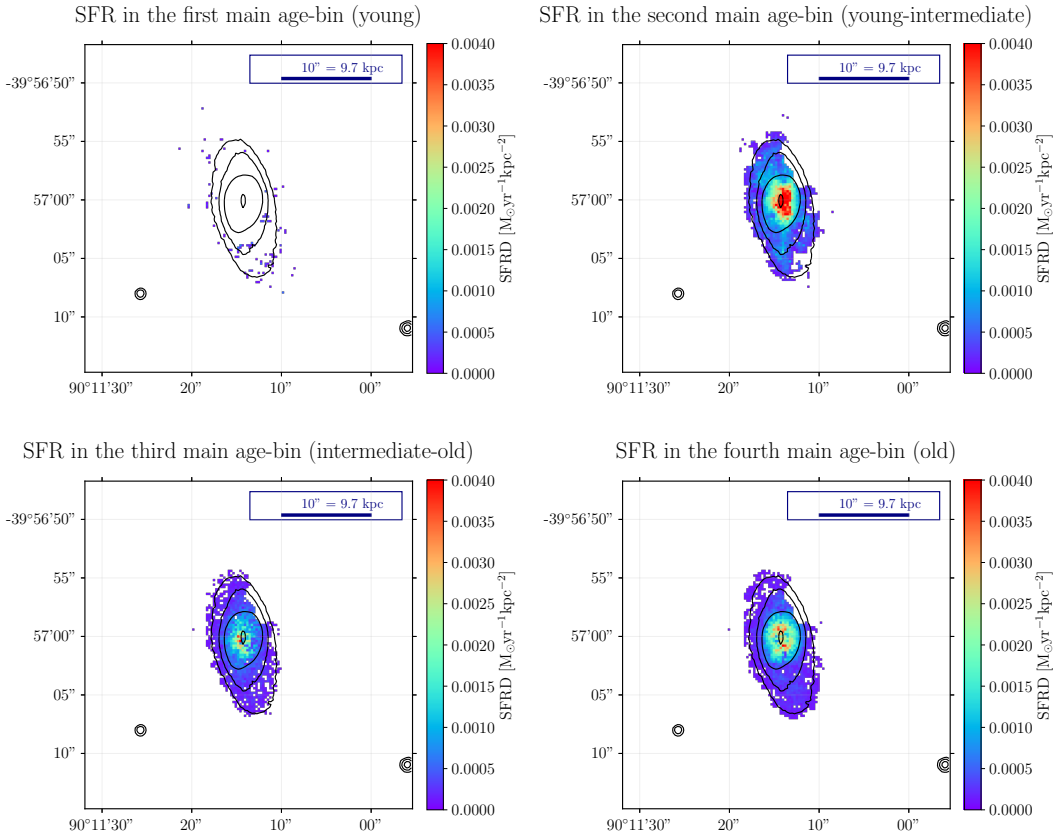

Figure 3.21: Maps of the star formation rate density (SFRD) for A3376_B_0214. In the second age-bin there is evidence of the presence of enhanced star formation in the central region of the galaxy (red area).

.

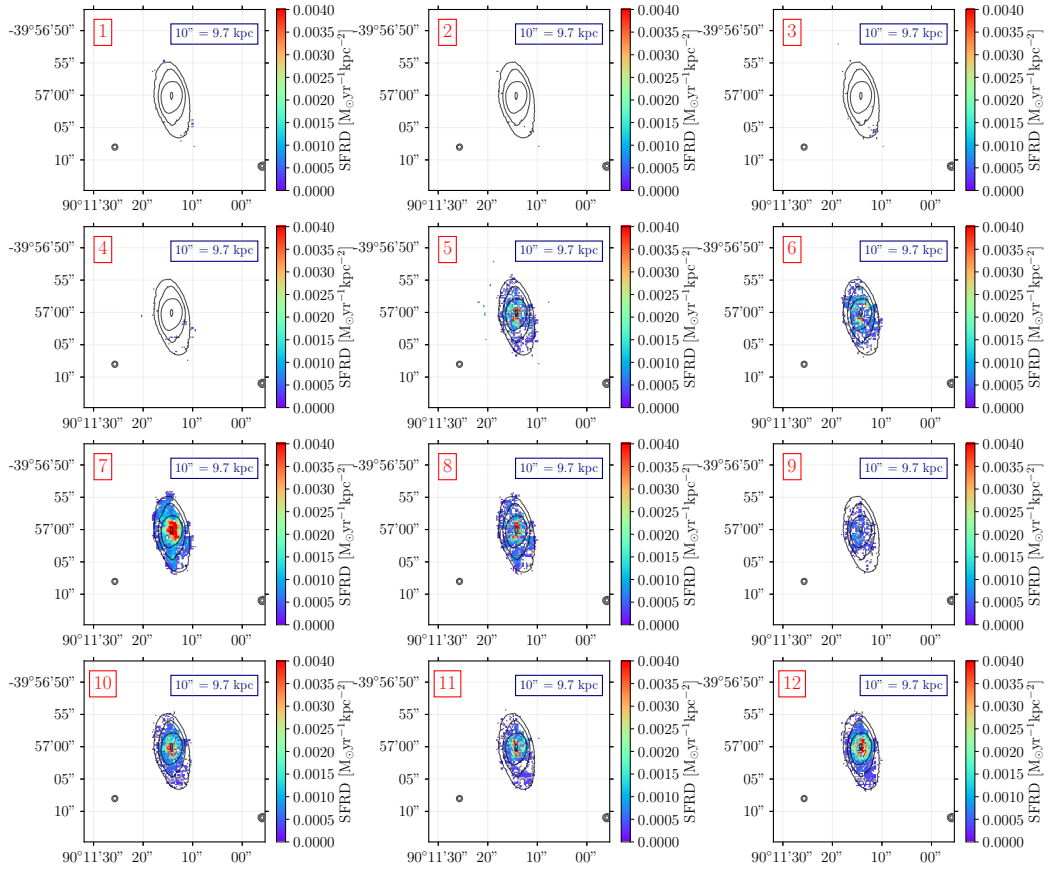

Figure 3.22: Age bins of the SFRD of A3376_B_0214. In the 7th bin we can notice the central burst of star formation (corresponding to $2.0 \cdot 10^8$ yr $\leq t \leq 5.7 \cdot 10^8$ yr ago). We excluded bad pixel data and values less than 10^{-4} for the SFRD from these maps.

Galaxy	Log_{10}(mass weighted age) mean (yr)
A3376_B_0214	9.77±0.08
A3128_B_0248	9.84±0.07
A3158_B_0234	9.70±0.09
A3158_11_91	9.76±0.08
A500_F_0152	9.69±0.13
A3158_B_0223	9.87±0.06
A1069_B_0103	9.83±0.06
A500_22_184	9.77±0.12

Table 3.8: Mass-weighted age mean within r_{e} and its standard deviation.

In this work, I use mass-weighted ages for our analysis (see chapter 5 for the main results and the appendix for the mass-weighted age maps.). I averaged the mass-weighted age values within r_{e}. The results are shown in Table 3.8.

Chapter 4

Overview of individual galaxies

In this Chapter I show the results for each sample galaxy. Its morphological features, star formation history and correlations between physical properties.

4.1 A3128_B_0248

A3128_B_0248 is an S0 galaxy. It is an almost edge-on system and one of the most massive galaxies of the sample, since its stellar mass is $M_* = 1.93 \cdot 10^{10}$ $M_\odot$. Its surface brightness profile shows no sign of other components than an exponential bulge ($n = 0.98$) and an exponential disk (Figure 4.1). The GALFIT analysis (figure 4.1), however highlights the possible presence of a small bar in its core. To confirm a bar presence, we used `bmodel` to analyze the residual map (Figure 4.2) which reveal a small and elongated component in the center.
From the SINOPSIS outputs (Figure 4.3), I find that the more recent central burst has occurred between $0.02 < t < 0.06$ Gyr ago. Moreover there has been no evolution in the initial distribution of star formation with the cosmic time. The computed EW(Hβ) inside r_e is 3.54 Å, and its radial profile is almost constant with a value of EW(Hβ)$\sim$ 4 Å till one r_e (Figure 4.5).

4.2 A3158_11_91

This spiral has an inner bar as seen from the surface-brightness radial profile (Figure 4.6). Two spiral arms depart from the bulge.
The photometric decomposition highlights the presence of a small bulge with $n = 0.48$. The GALFIT residual image (Figure 4.6) shows two spiral arms departing from the galaxy nucleus.

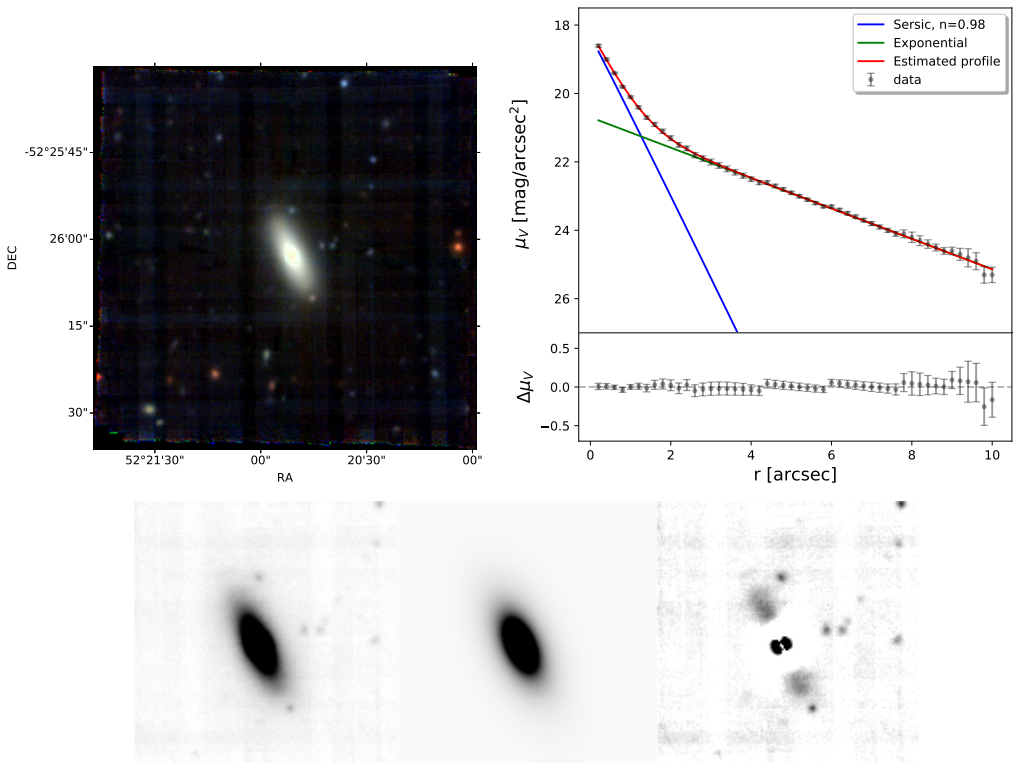

Figure 4.1: Color image from g, r, and i bands extracted from MUSE data-cube (upper left panel), surface brightness radial profile and photometric decomposition (upper right panel) and GALFIT output (input, model and residual image, lower panels) for A3128_B_0248.

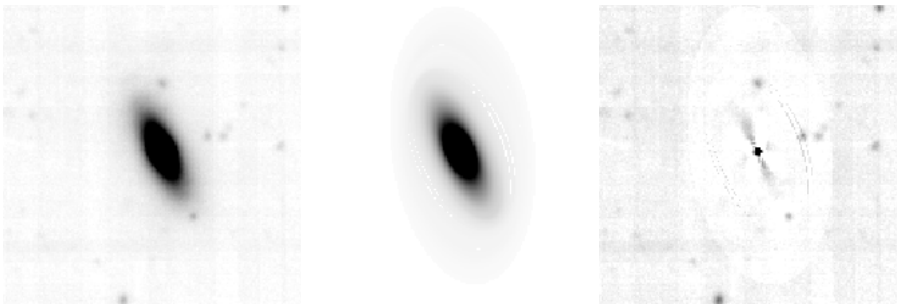

Figure 4.2: IRAF `bmodel` output for A3128_B_0248 (input, model and residual image).

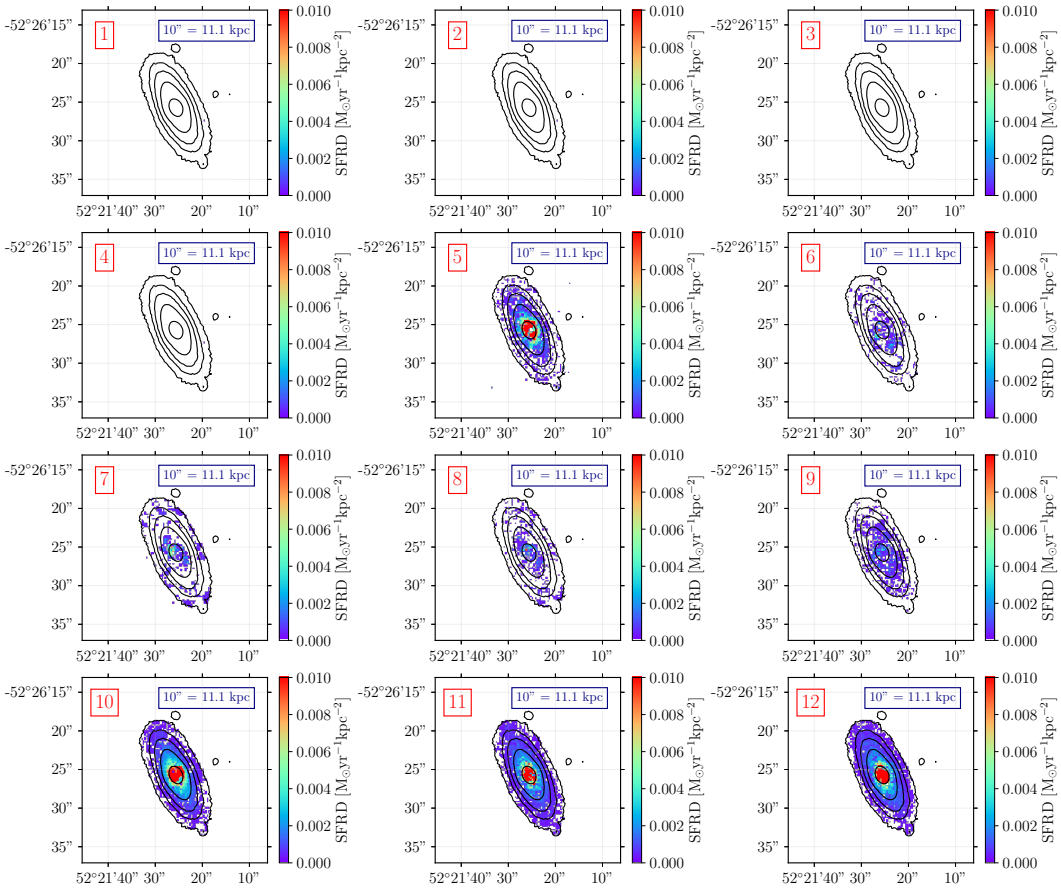

Figure 4.3: Age bins of the SFRD of A3128_B_0248. In the 5$^{\text{th}}$ bin we can notice the central burst of star formation ($2.0 \cdot 10^7$ yr $\leq t \leq 5.7 \cdot 10^7$ yr ago). We excluded bad pixel data and values less than 10^{-4} for the SFRD from these maps.

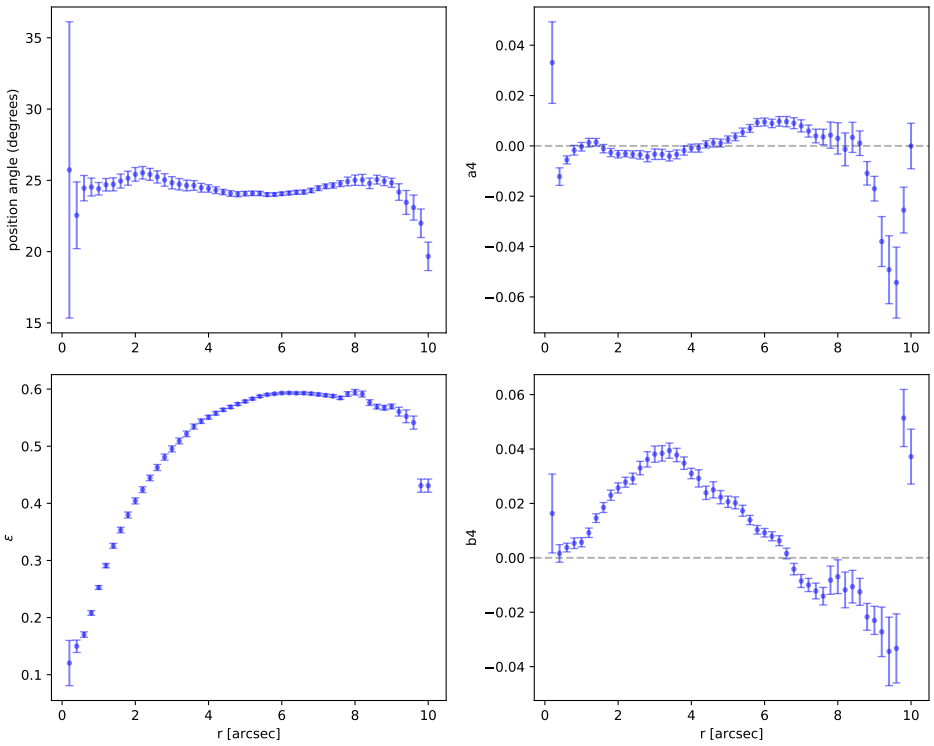

Figure 4.4: Radial profiles of the position angle, ellipticity, A4 and B4 for A3128_B_0248, from `ellipse`.

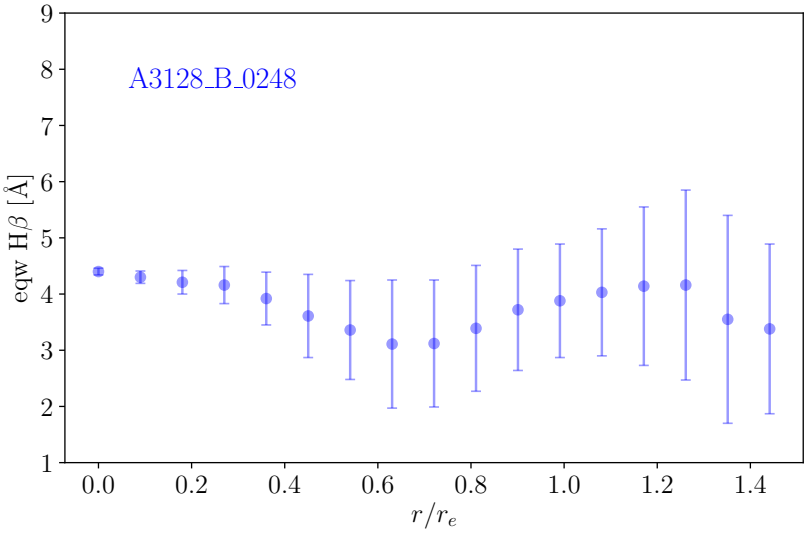

Figure 4.5: Averaged radial mean profile of EW(Hβ) for A3128_B_0248.

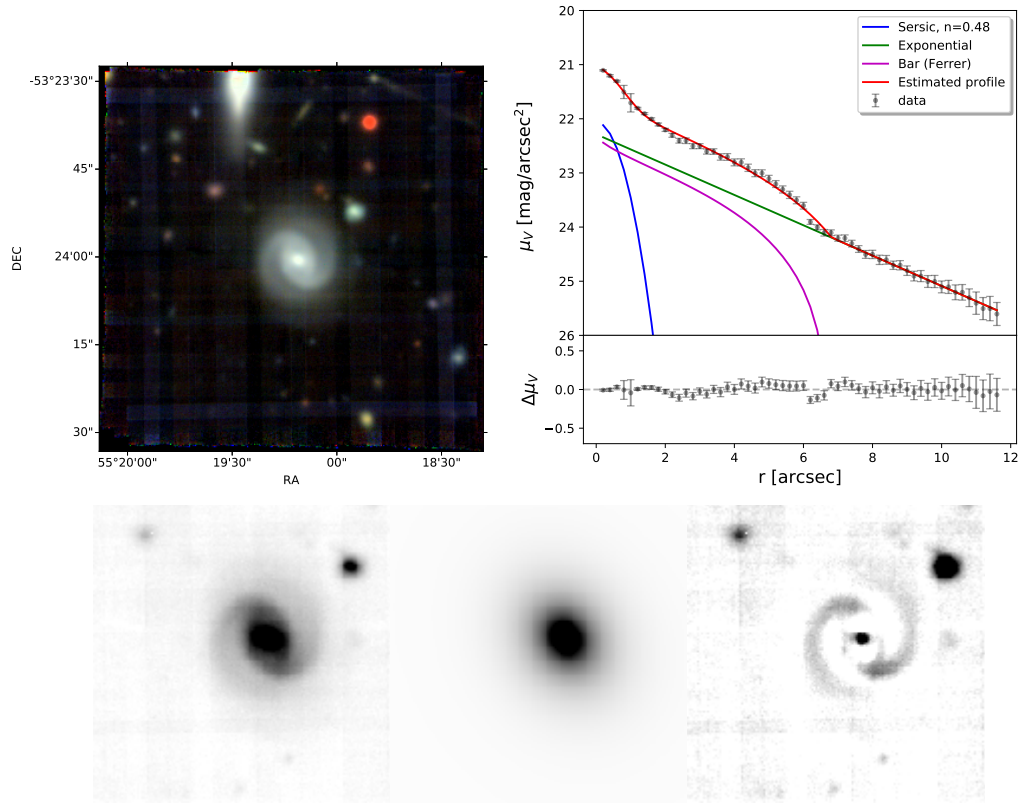

Figure 4.6: Color image from g, r, and i bands extracted from MUSE data-cube (upper left panel), surface brightness radial profile and photometric decomposition (upper right panel) and GALFIT output (input, model and residual image, lower panels) for A3158_11_91.

The radial profile of the EW(Hβ) (Figure 4.9) ranges from 4 to 5 Å within r_e, which is consistent with being a PSB galaxy. This is consistent with the EW(Hβ) mean value at r_e, that is 4.7 Å (see Table 3.6). From Figure 4.7, I notice that in the central region the more recent episode of star formation happened between $20 < t < 60$ Myr ago. The spatial distribution of the central burst of star formation shifted with cosmic time from the 9^{th} age bin to the 5^{th} in S-W direction.

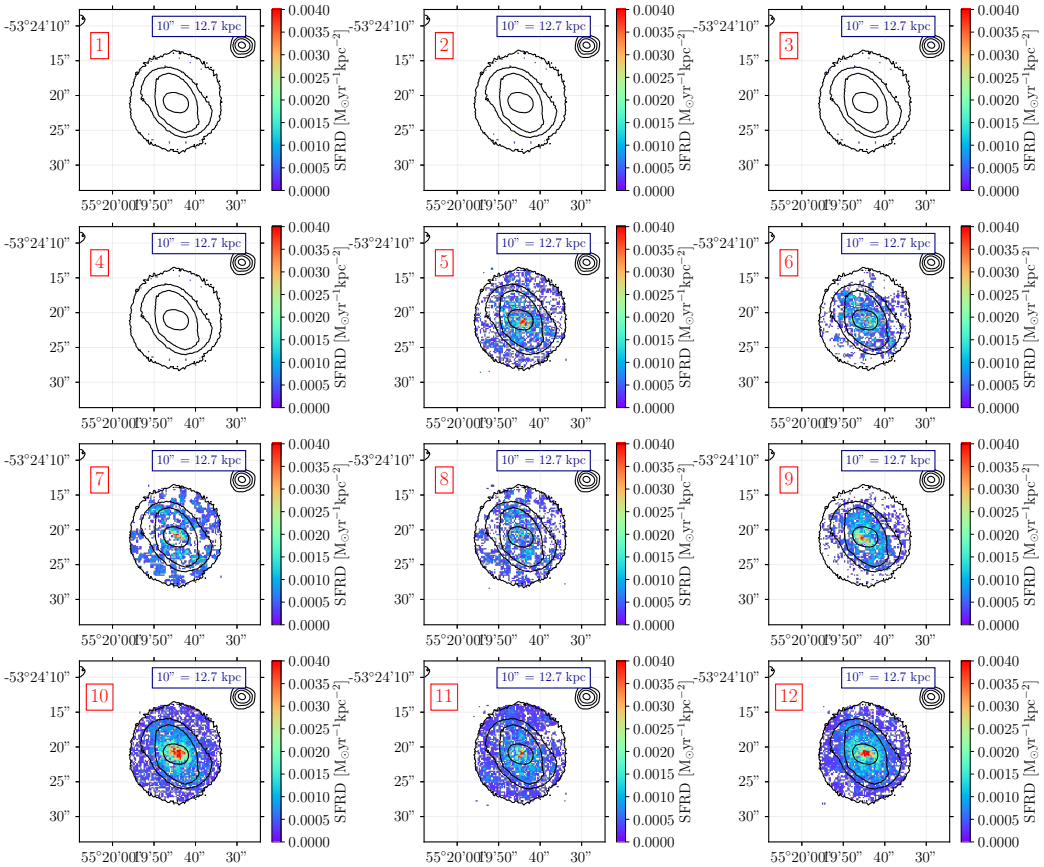

Figure 4.7: Age bins of the SFRD of A3158_11_91. In the 5^{th} bin we can notice the central burst of star formation ($2.0 \cdot 10^7$ yr $\leq t \leq 5.7 \cdot 10^7$ yr ago). We excluded bad pixel data and values less than 10^{-4} for the SFRD from these maps.

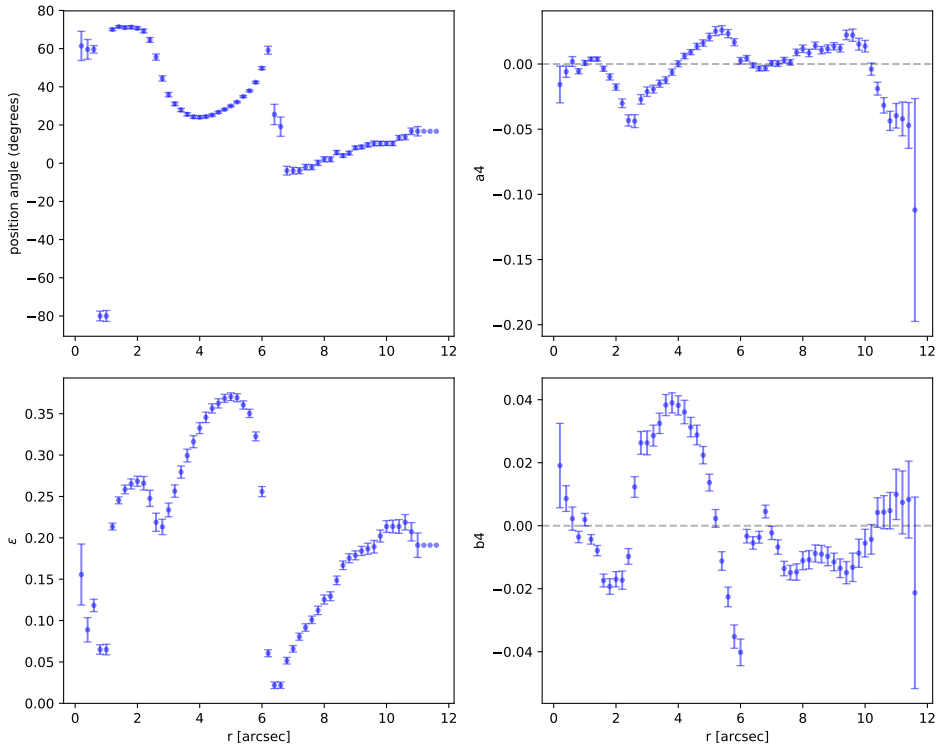

Figure 4.8: Radial profiles of the position angle, ellipticity, A4 and B4 for A3158_11_91, from `ellipse`.

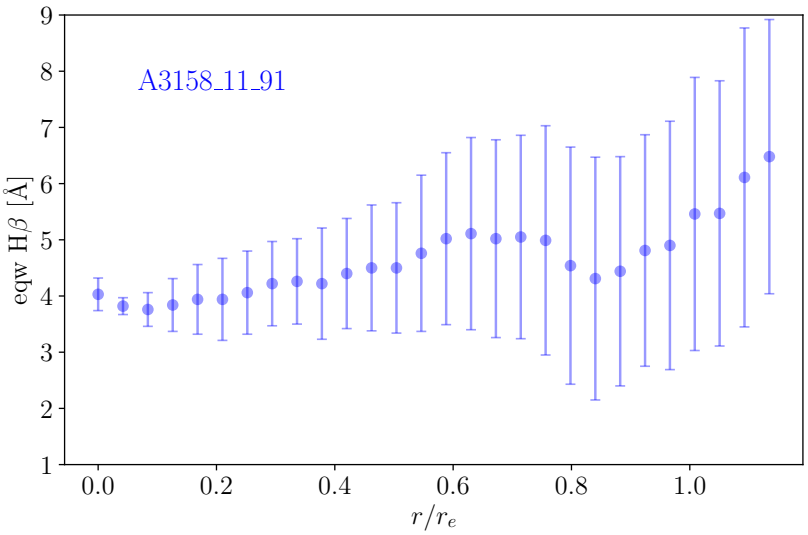

Figure 4.9: Averaged radial mean profile of EW(Hβ) for A3158_11_91.

4.3 A3158_B_0223

The image, photometric decomposition, and GALFIT output show the prominent bar of this lenticular galaxy, which is the most massive of the sample, with $M_* = 2.34 \cdot 10^{10}$ $M_\odot$. As already noted in Chapter 3, this galaxy has a small value for the inclination ($i \sim 26°$).
GALFIT analysis highlights the bar and the disk, with no spiral arms consistent with classification as S0.
This object presents the smaller $<$EW(Hβ)$>\sim$ 4.5 Å of the sample, with a decreasing radial profile (Figure 4.13). The central stellar population was probably born between $20 < t < 60$ Myr ago (Figure 4.11). The first burst of star formation, happened in the 12^{th} age bin, moved towards N-E, remained in the same position along the more recent central burst in the 5^{th} age bin.

4.4 A3158_B_0234

A3158_B_0234 is an early spiral galaxy, with a stellar mass of $M_*0.7{\cdot}10^{10}$ $M_\odot$. The spiral arms and bar are remarkably visible from the GALFIT residuals map (Figure 4.14). The surface-brightness radial profile shows the presence of a pseudo bulge ($n = 0.85$), a bar, and an exponential disk.
The more recent burst of star formation in the central region seemed to have occurred in two age bins (5^{th} and 6^{th}), $0.02 < t < 0.2$ Gyr ago. Another older episode happened between $1 < t < 3$ Gyr (Figure 4.15).
Its EW(Hβ) radial profile goes from $\sim$ 5 to 6 Å (Figure 4.17), thus its mean value within r_e, is $<$EW(Hβ)=5.46 Å.

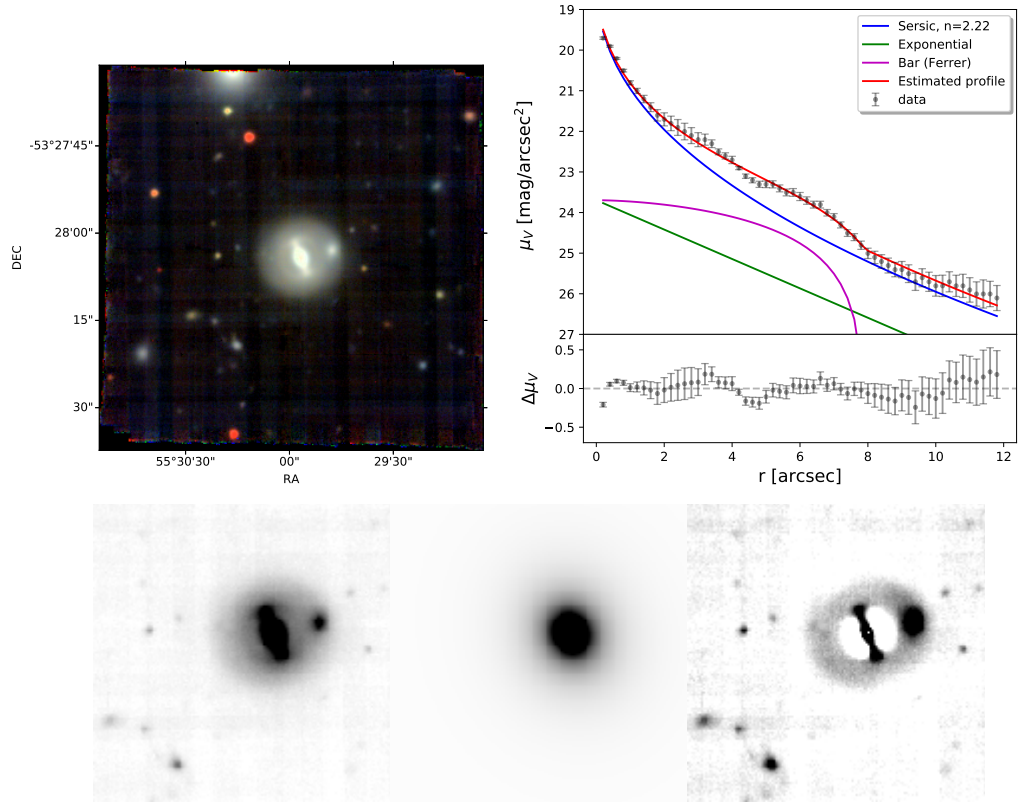

Figure 4.10: Color image from g, r, and i bands extracted from MUSE data-cube (upper left panel), surface brightness radial profile and photometric decomposition (upper right panel) and GALFIT output (input, model and residual image, lower panels) for A3158_B_0223.

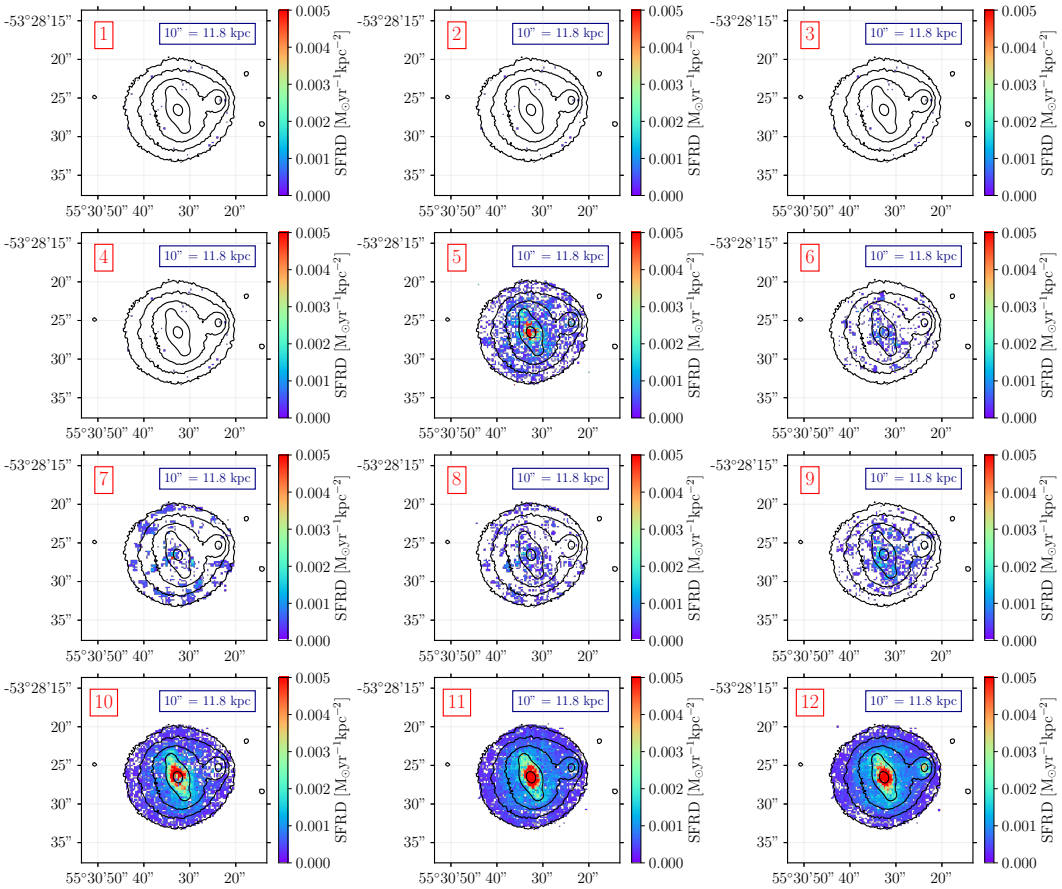

Figure 4.11: Age bins of the SFRD of A3158_B_0223. In the 5$^{\text{th}}$ bin we can notice the central burst of star formation ($2.0 \cdot 10^7$ yr $\leq t \leq 5.7 \cdot 10^7$ yr ago). We excluded bad pixel data and values less than 10^{-4} for the SFRD from these maps.

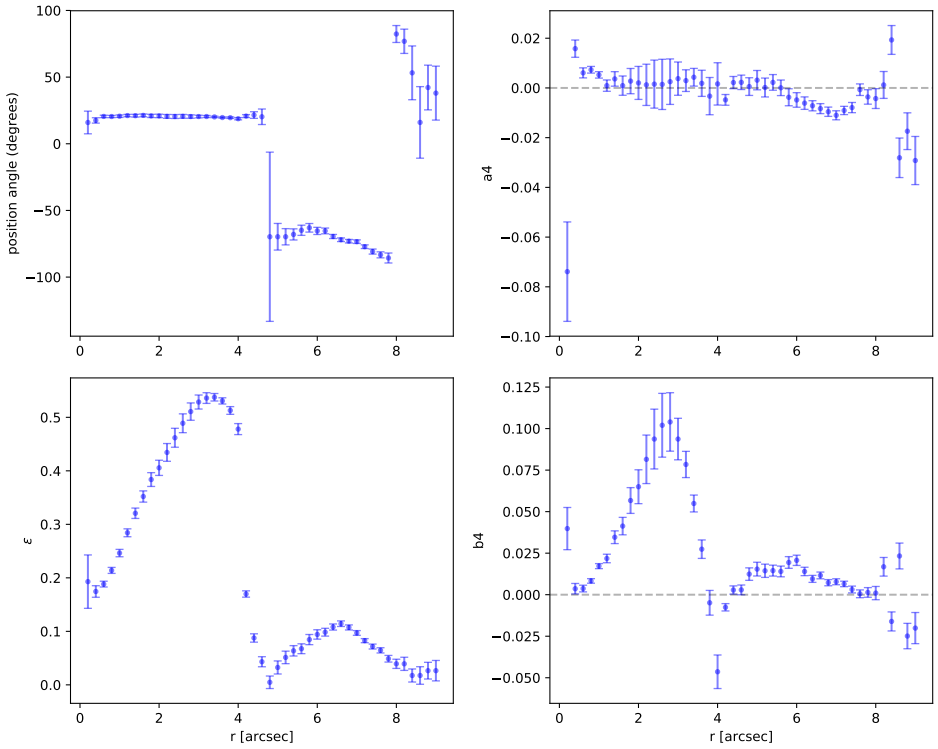

Figure 4.12: Radial profiles of the position angle, ellipticity, A4 and B4 for A3158_B_0223, from `ellipse`.

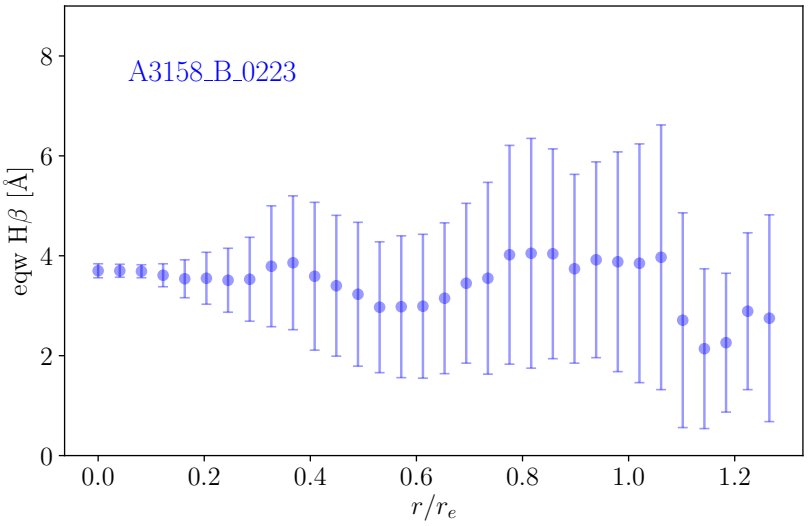

Figure 4.13: Averaged radial mean profile of EW(Hβ) for A3158_B_0223.

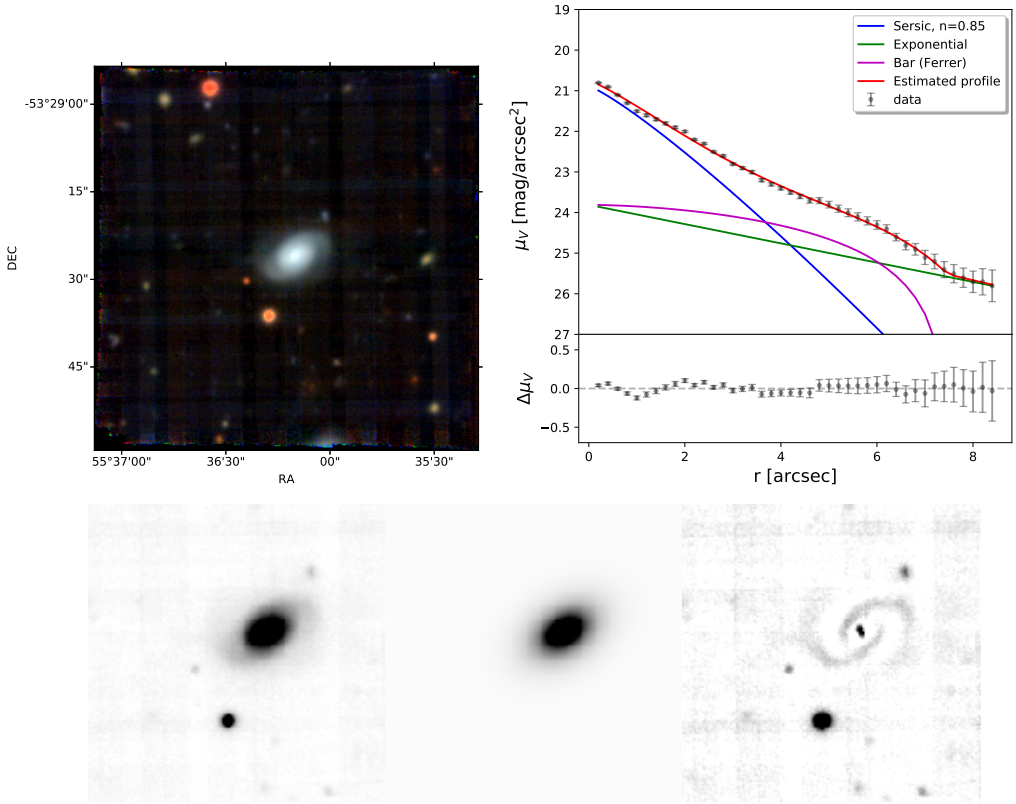

Figure 4.14: Color image from g, r, and i bands extracted from MUSE data-cube (upper left panel), surface brightness radial profile and photometric decomposition (upper right panel) and GALFIT output (input, model and residual image, lower panels) for A3158_B_0234.

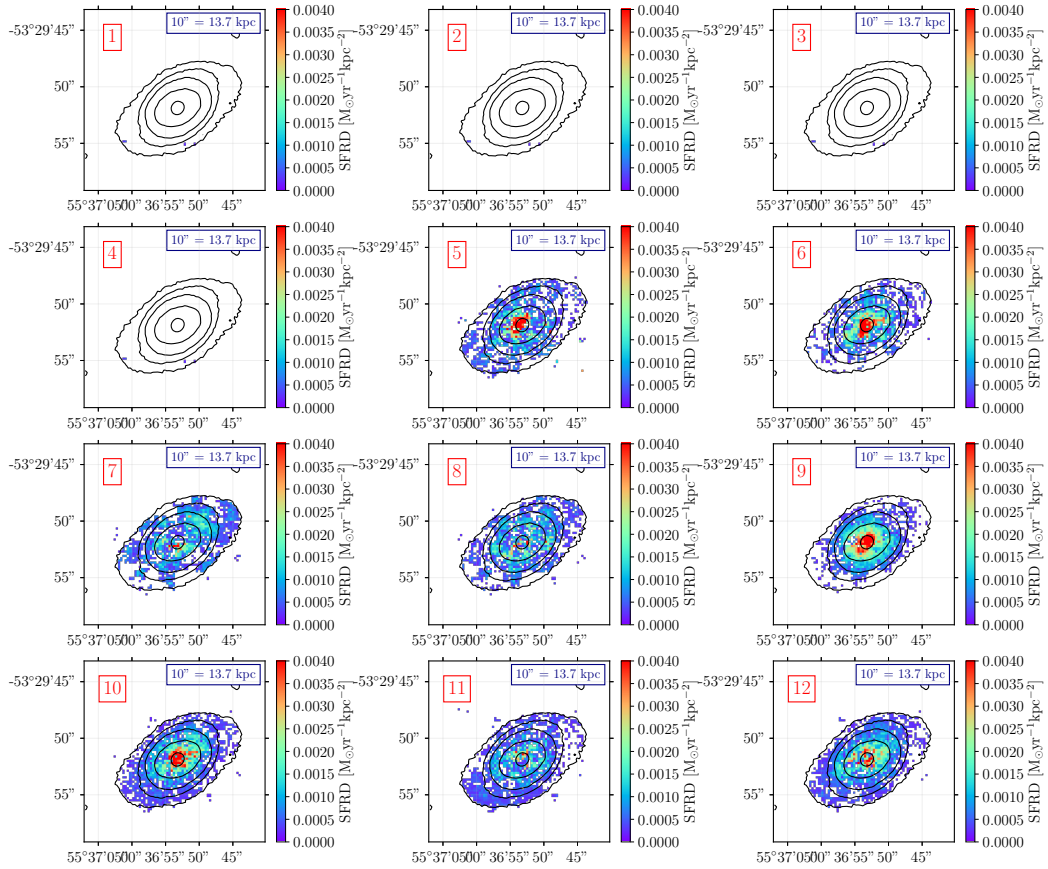

Figure 4.15: Age bins of the SFRD of A3158_B_0234. In the 5$^{\text{th}}$ bin we can notice the central burst of star formation ($2.0 \cdot 10^7$ yr $\leq t \leq 5.7 \cdot 10^7$ yr ago). We excluded bad pixel data and values less than 10^{-4} for the SFRD from these maps.

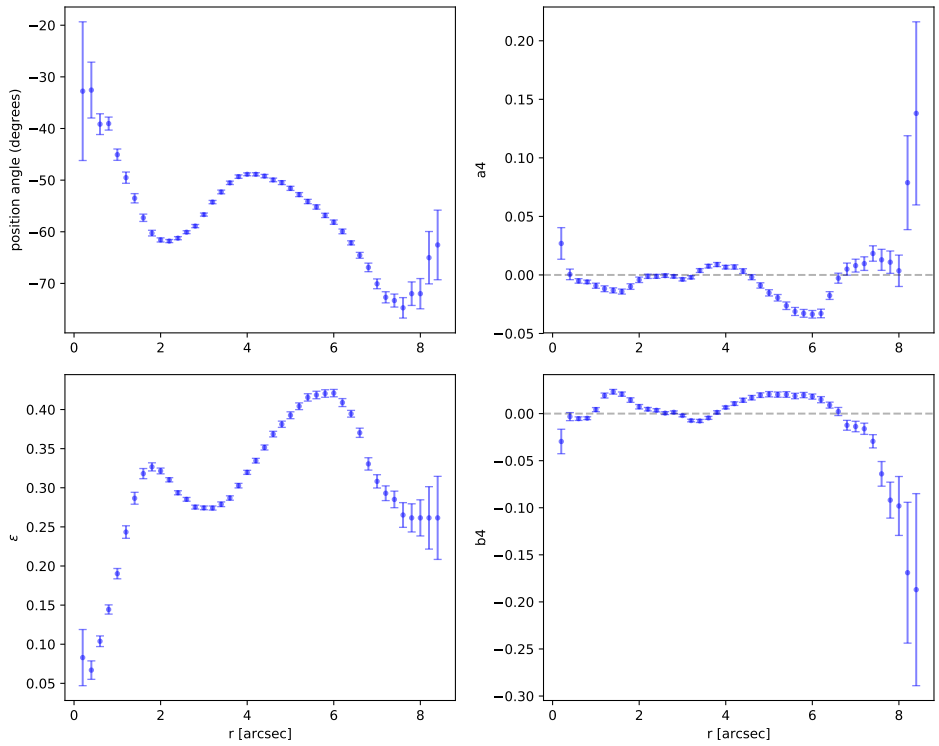

Figure 4.16: Radial profiles of the position angle, ellipticity, A4 and B4 for A3158_B_0234, from `ellipse`.

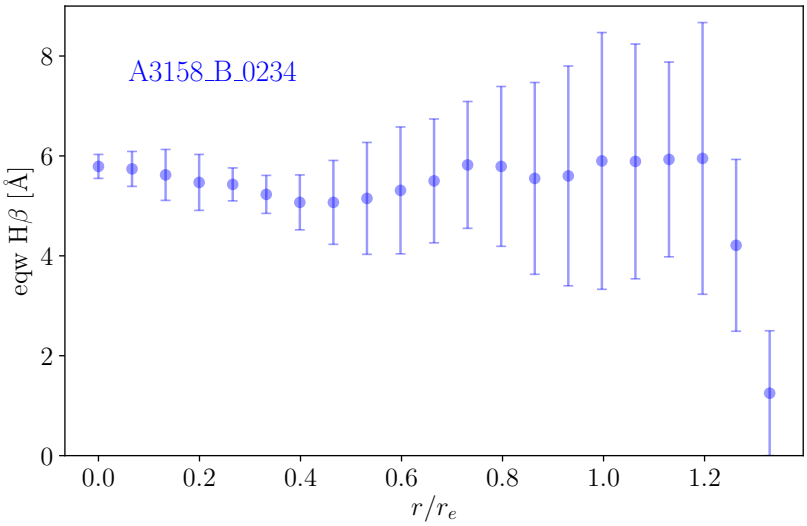

Figure 4.17: Averaged radial mean profile of EW(Hβ) for A3158_B_0234.

4.5 A500_F_0152

The early spiral galaxy A500_F_0152 has an exponential bulge ($n = 1.07$) and an exponential disk.
None of the two photometric decomposition techniques brings evidence of a bar (Figures 4.18 and 4.19). The mean value of EW(Hβ) within r_e is 6.61 Å and its radial profile goes from 6 Å to $\sim$ 7 Å in the same radial distance (Figure 4.22). The EW(Hβ) value is one of the highest in the whole sample together with A3376_B_0214.
SINOPSIS outputs show that the younger A-type stars population could be lightened up $0.02 < t < 0.2$ Gyr ago. The SFH of this galaxy shows an ongoing stellar birth from the 5^{th} to the 8^{th} age bin (Figure 4.20). As already pointed out in Chapter 1, the spectra of galaxies k+a can be associated with PSB galaxies but also with post-starforming ones. Not having had a single burst of star formation but showing an ongoing SFR with cosmic time, it seems that this galaxy can be counted as post-starforming. Moreover, there has been an evolution with cosmic time of star formation spatial distribution. From the 9^{th} age bin, it has shifted to S-W and returned N-E with the 5^{th} age bin.

4.6 A500_22_184

A500_22_184 is an early spiral galaxy. It shows no presence of a bar, both in the photometric decomposition and in the GALFIT output (Figure 4.23).
The mean EW(Hβ) value is 4.28 Å and its radial profile is almost constant within r_e (figure 4.27).
The more recent central burst occurred $20 < t < 60$ Myr ago (Figure 4.25). There are no evident sign of an evolution of spatial distribution of the star formation with cosmic time (Figure 4.25).

4.7 A1069_B_0103

This almost edge-on spiral (i$\sim$ 70°) shows a bar only in the GALFIT residuals (Figure 4.28). Its surface-brightness radial profile is decomposed into a nearly-exponential bulge ($n = 1.38$) and in an exponential disk.
Being uncertain the presence of a bar, I run `bmodel` (Figure 4.29). The residual map shows some central components, probably due to the spiral

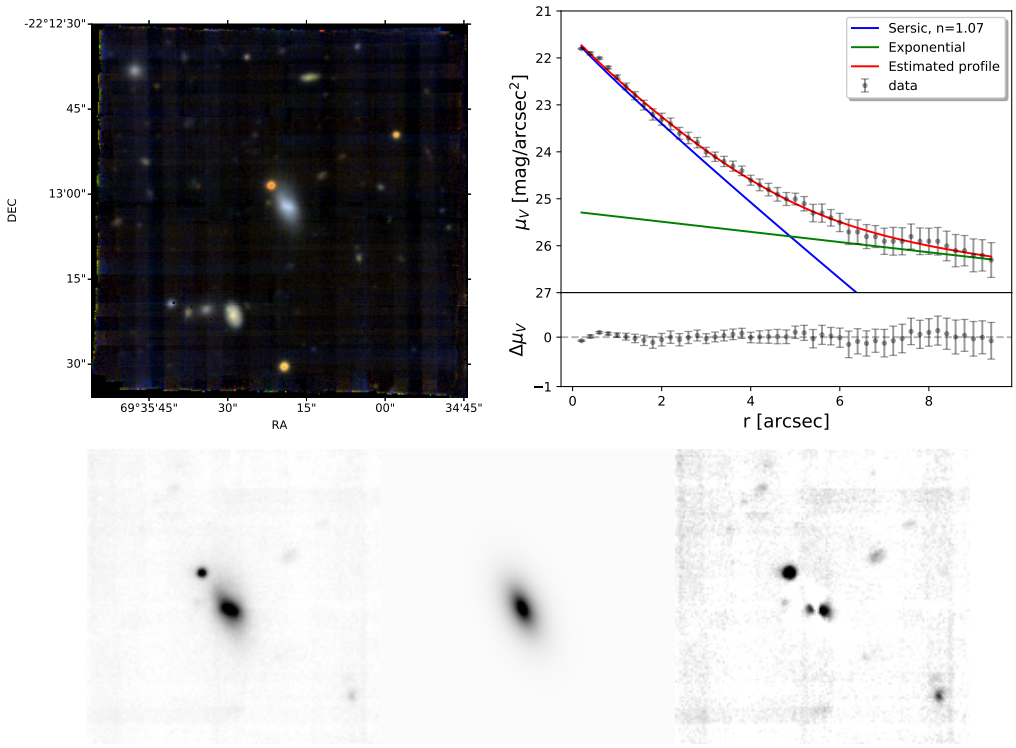

Figure 4.18: Color image from g, r, and i bands extracted from MUSE data-cube (upper left panel), surface brightness radial profile and photometric decomposition (upper right panel) and GALFIT output (input, model and residual image, lower panels) for A500_F_0152.

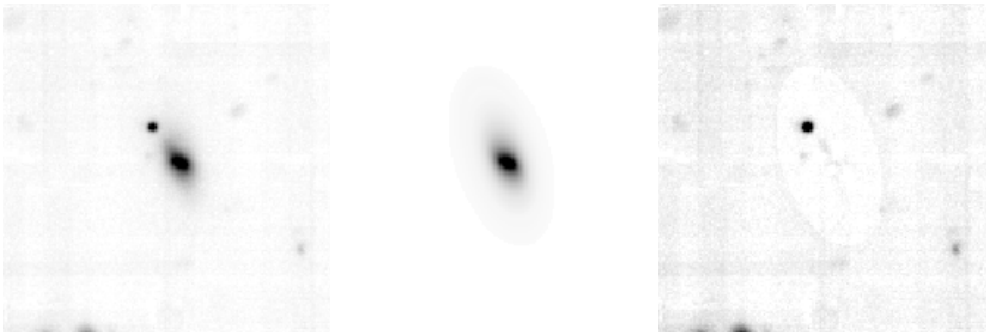

Figure 4.19: IRAF `bmodel` output for A500_F_0152 (input, model and residual image).

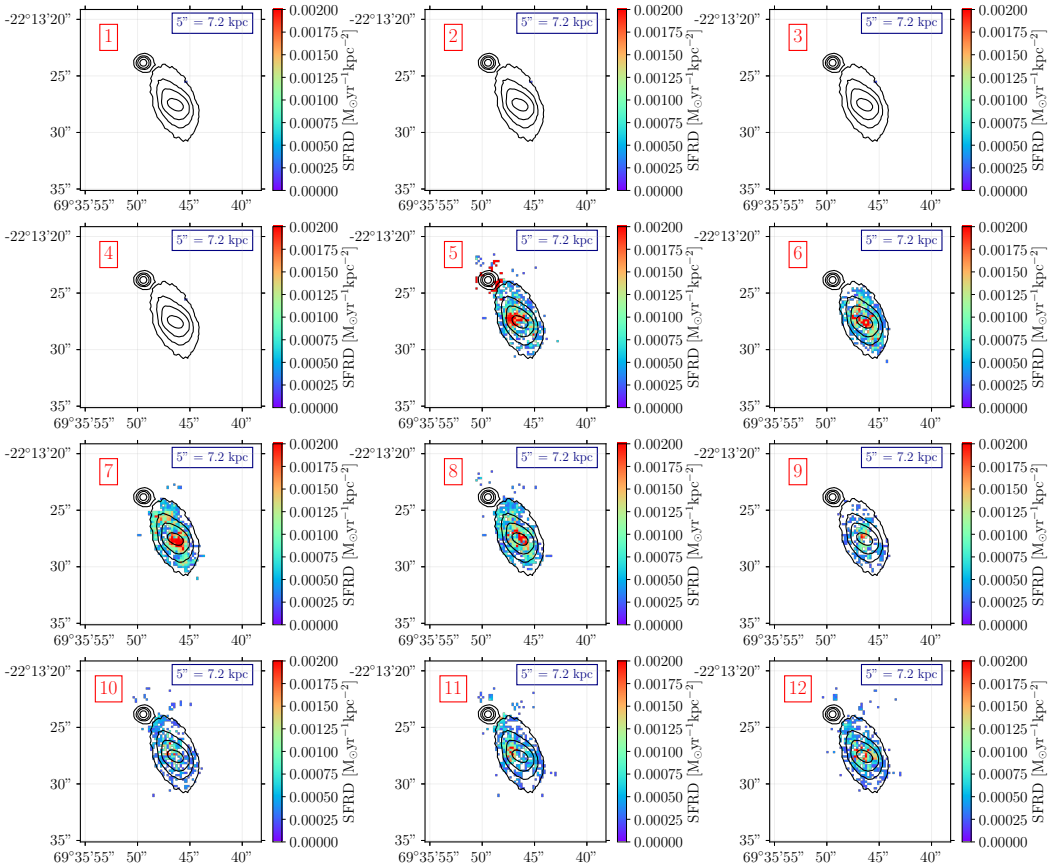

Figure 4.20: Age bins of the SFRD of A500_F_0152. In the 5$^{\text{th}}$ bin we can notice an ongoing central star formation up to $2.0 \cdot 10^7$ yr ago. We excluded bad pixel data and values less than 10^{-4} for the SFRD from these maps.

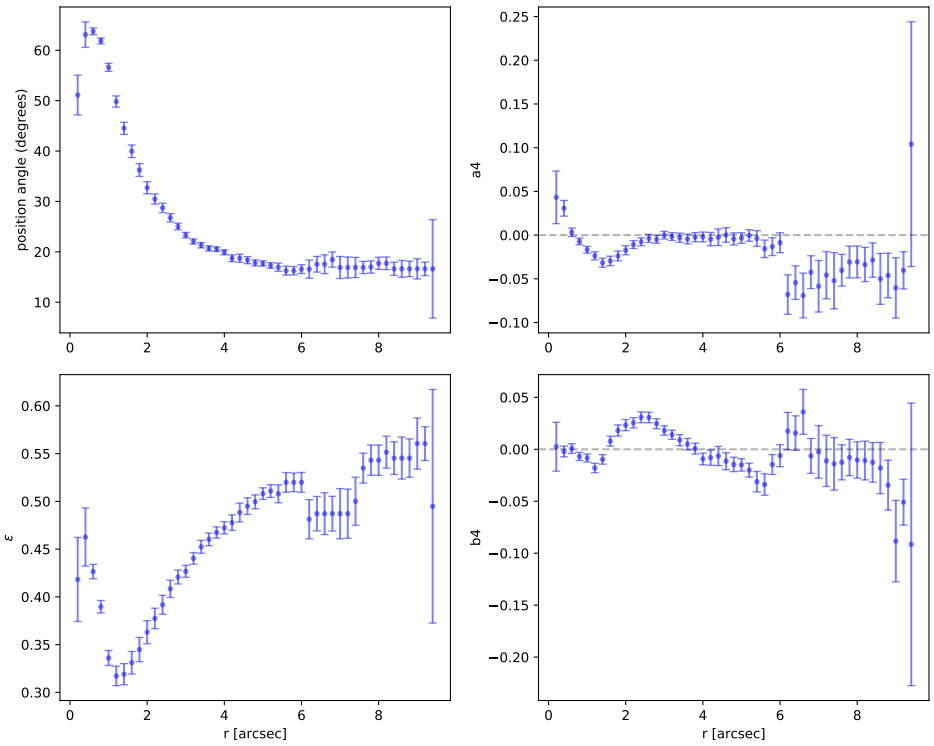

Figure 4.21: Radial profiles of the position angle, ellipticity, A4 and B4 for A500_F_0152, from `ellipse`.

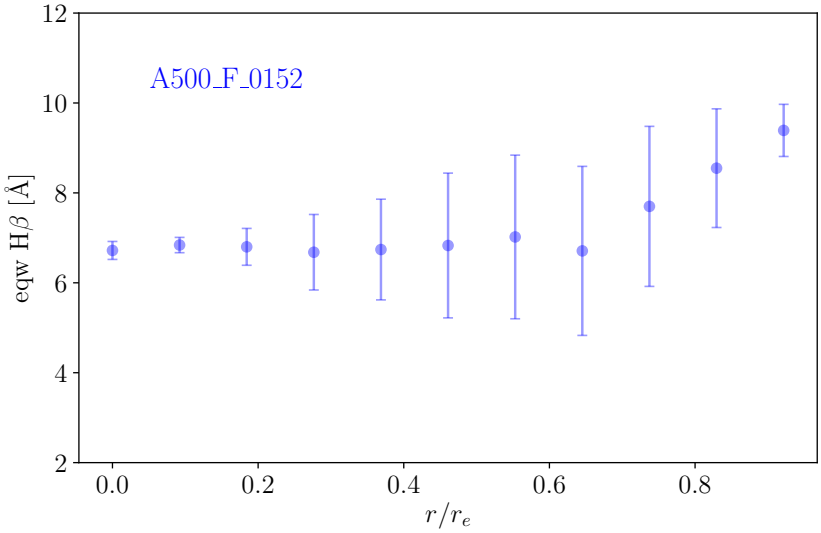

Figure 4.22: Averaged radial mean profile of EW(Hβ) for A500_F_0152.

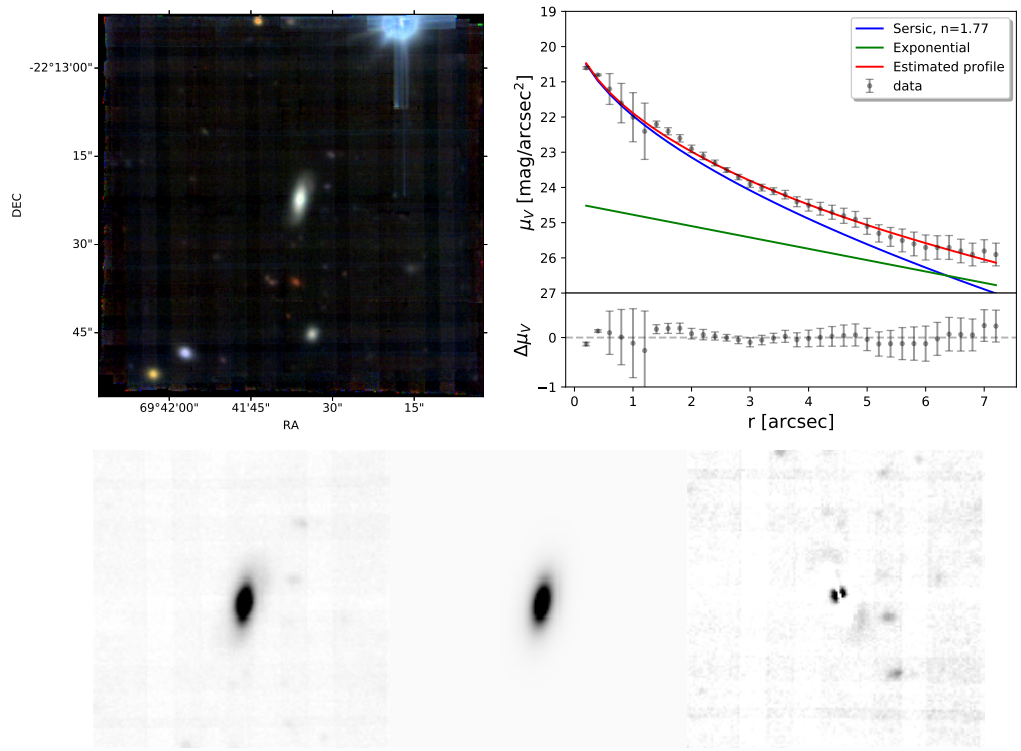

Figure 4.23: Color image from g, r, and i bands extracted from MUSE data-cube (upper left panel), surface brightness radial profile and photometric decomposition (upper right panel) and GALFIT output (input, model and residual image, lower panels) for A500_22_184.

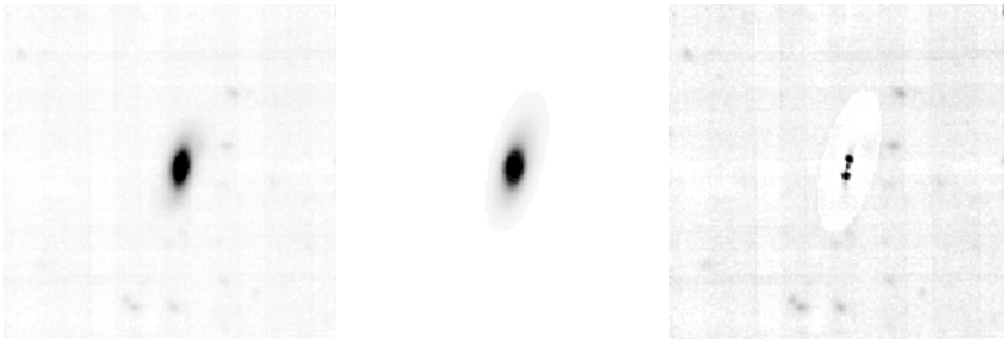

Figure 4.24: IRAF `bmodel` output for A500_22_184 (input, model and residual image).

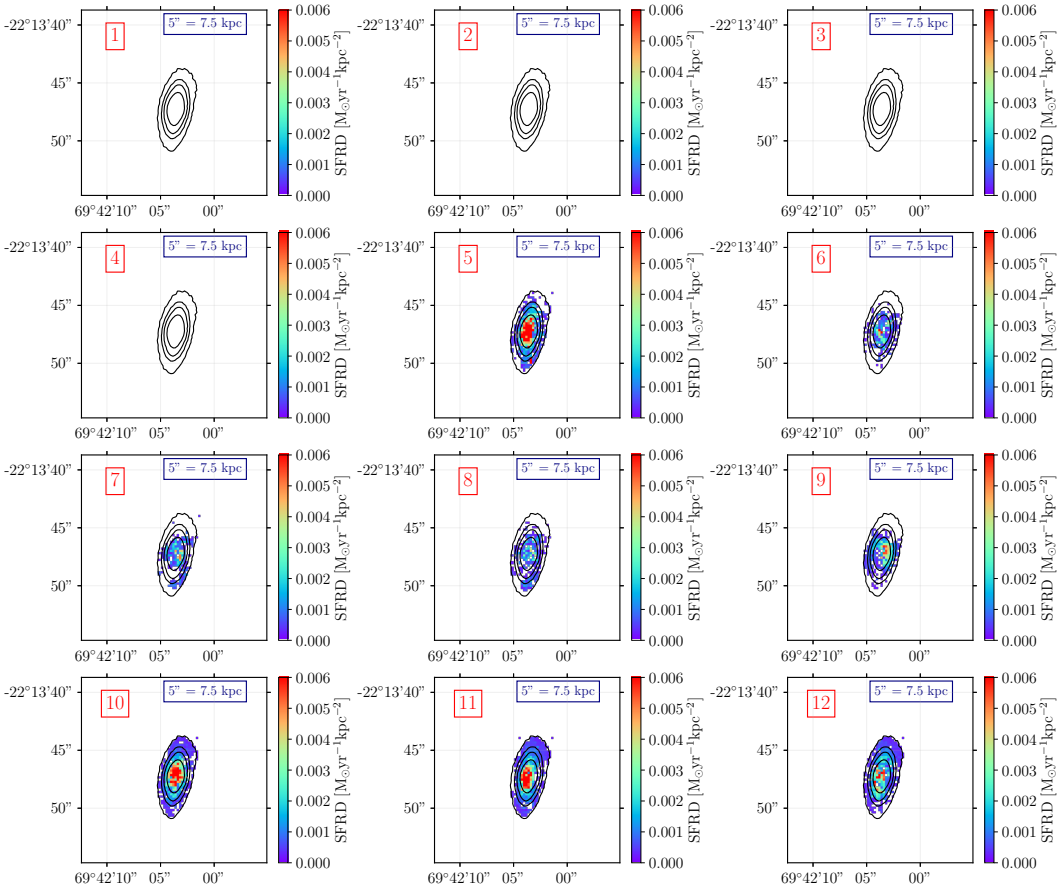

Figure 4.25: 12 SFR age-bins of SFR density for A500_22_184. In the 5$^{\text{th}}$ bin we can notice the more recent central burst of star formation, corresponding to $2.0 \cdot 10^7$ yr $\leq t \leq 5.7 \cdot 10^7$ yr ago). We excluded outliers and values less than 10^{-4} for the SFRD from these maps.

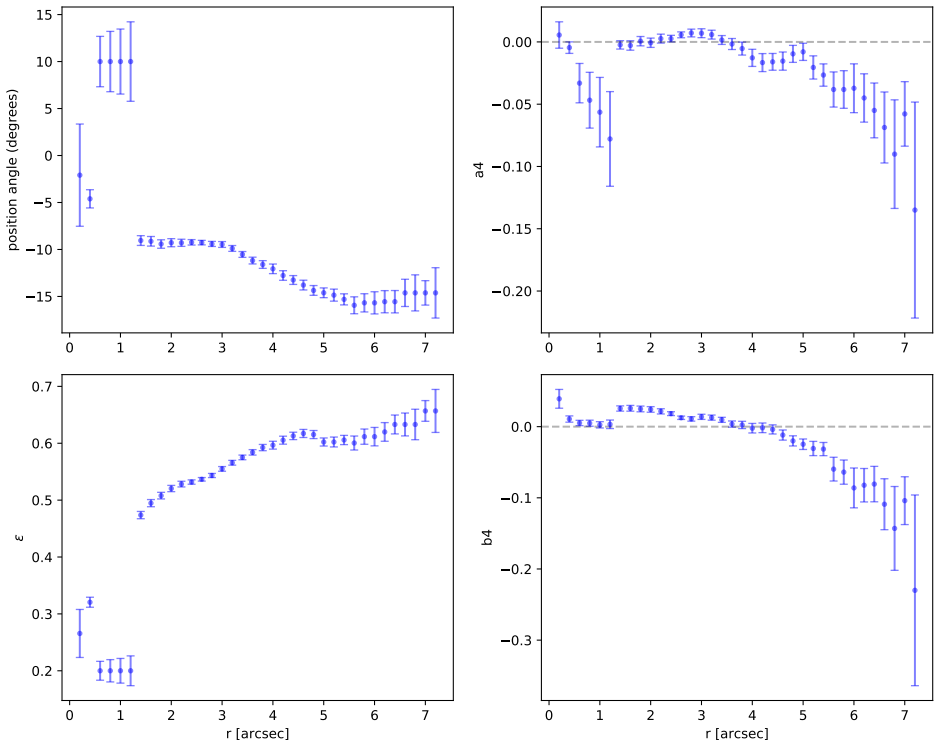

Figure 4.26: Radial profiles of the position angle, ellipticity, A4 and B4 for A500_22_184, from `ellipse`.

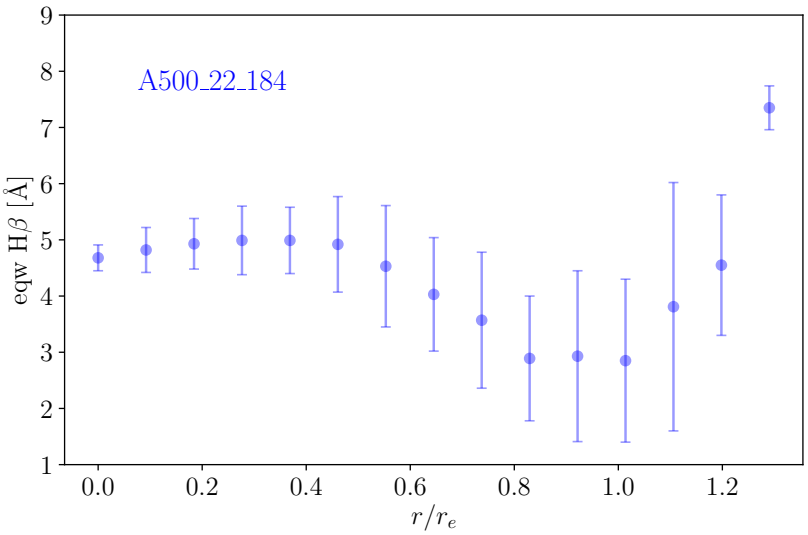

Figure 4.27: Averaged radial mean profile of EW(Hβ) for A500_22_184.

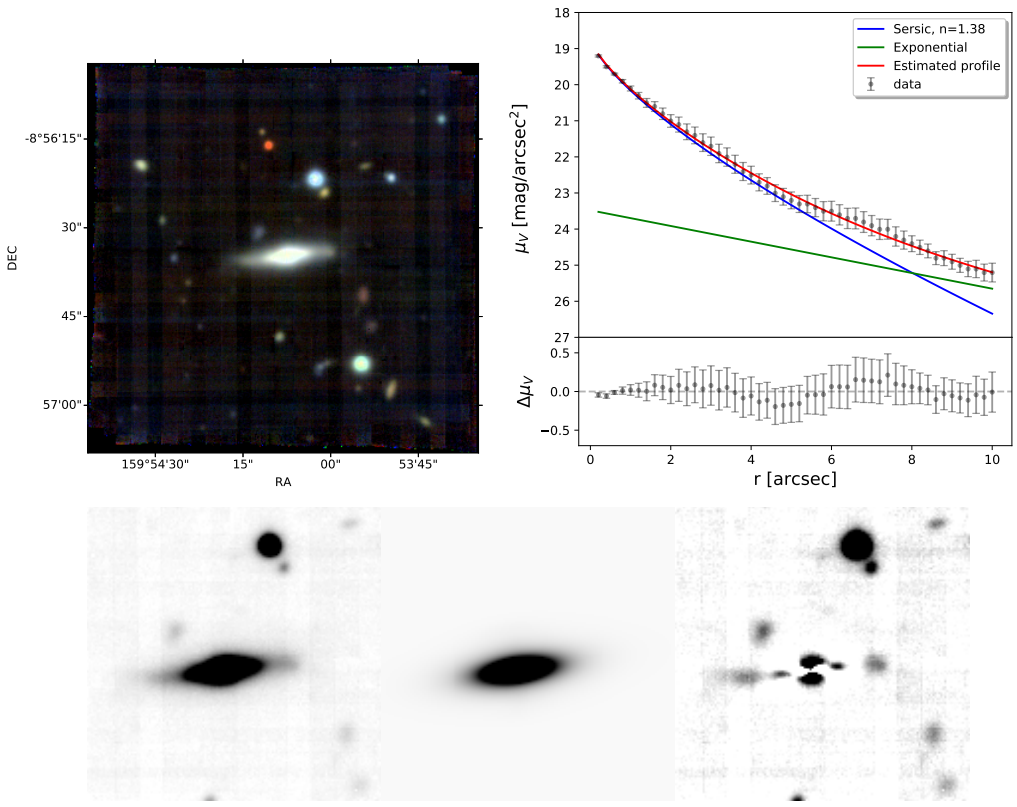

Figure 4.28: Color image from g, r, and i bands extracted from MUSE data-cube (upper left panel), surface brightness radial profile and photometric decomposition (upper right panel) and GALFIT output (input, model and residual image, lower panels) for A1069_B_0103.

arms seen edge-on.
It has a constant EW(Hβ) radial profile ($\sim$ 4 Å, Figure 4.32), confirmed by a mean of 4.03 Å. The more recent burst of star formation is dated from 20 $< t <$ 60 Myr ago. From the 6$^{\text{th}}$ to the 5$^{\text{th}}$ age bin, the central younger population of stars shifted from E-W direction to N-S along the minor axis.

4.8 A3376_B_0214

A3376_B_0214 exhibits a bar in the photometric decomposition. It is classified as an S0 galaxy, but it shows two prominent spiral arms in the

Figure 4.29: IRAF `bmodel` output for A1069_B_0103 (input, model and residual image).

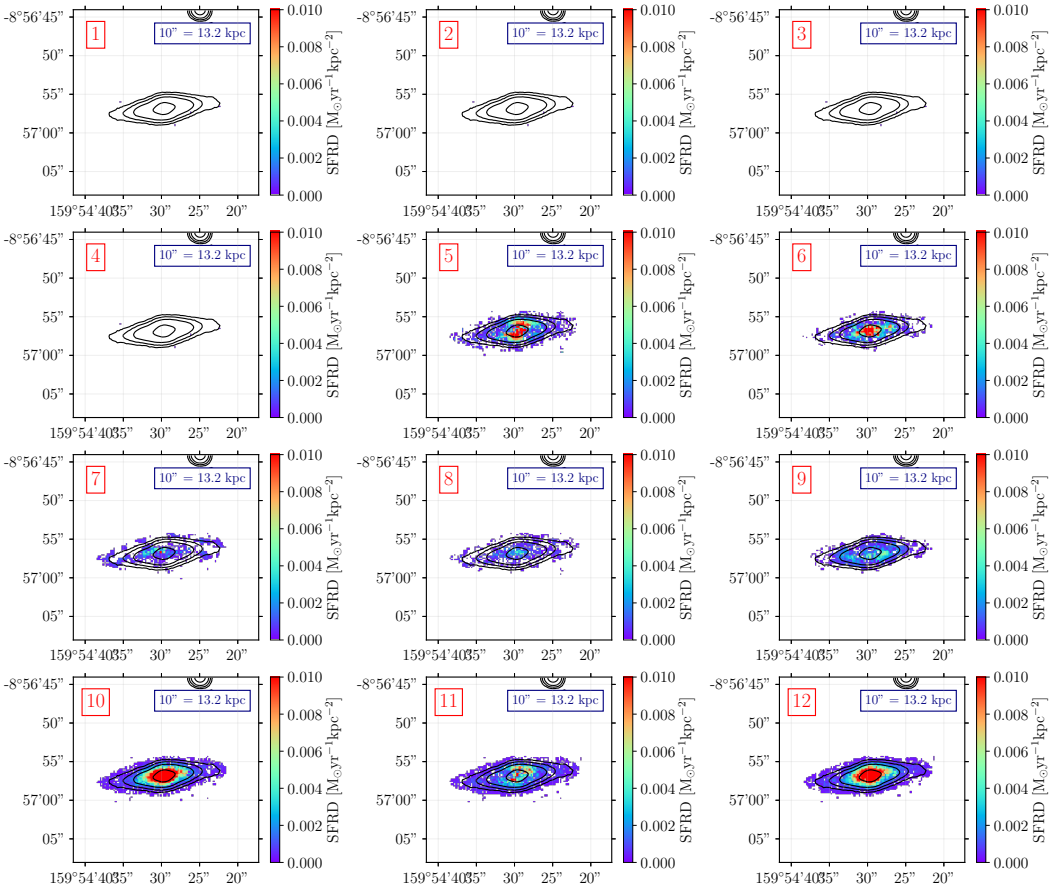

Figure 4.30: Age bins of the SFRD of A1069_B_0103. In the 5$^{\text{th}}$ bin we can notice the central burst of star formation ($2.0 \cdot 10^7$ yr $\leq t \leq 5.7 \cdot 10^7$ yr ago). We excluded bad pixel data and values less than 10^{-4} for the SFRD from these maps.

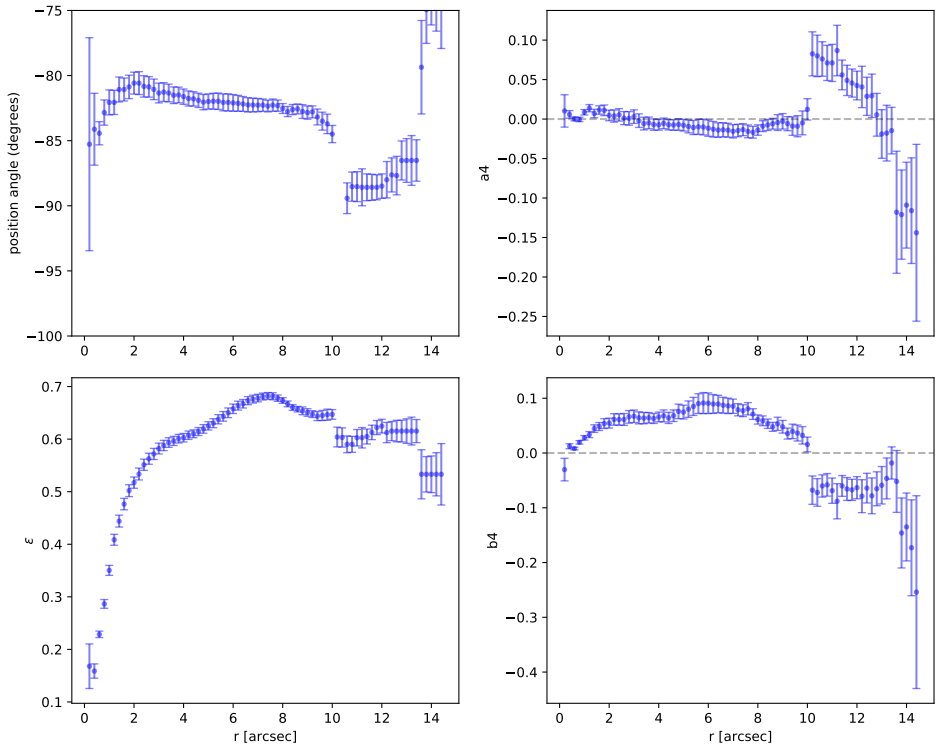

Figure 4.31: Radial profiles of the position angle, ellipticity, A4 and B4 for A1069_B_0103, from `ellipse`.

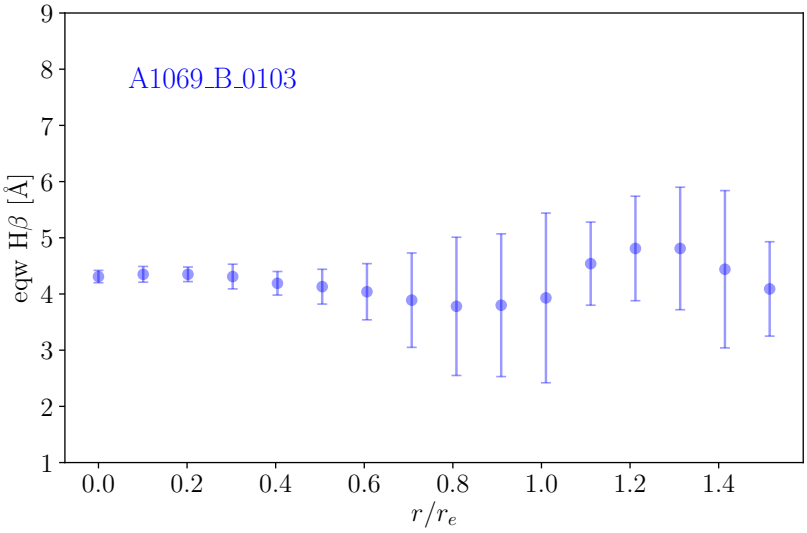

Figure 4.32: Averaged radial mean profile of EW(Hβ) for A1069_B_0103.

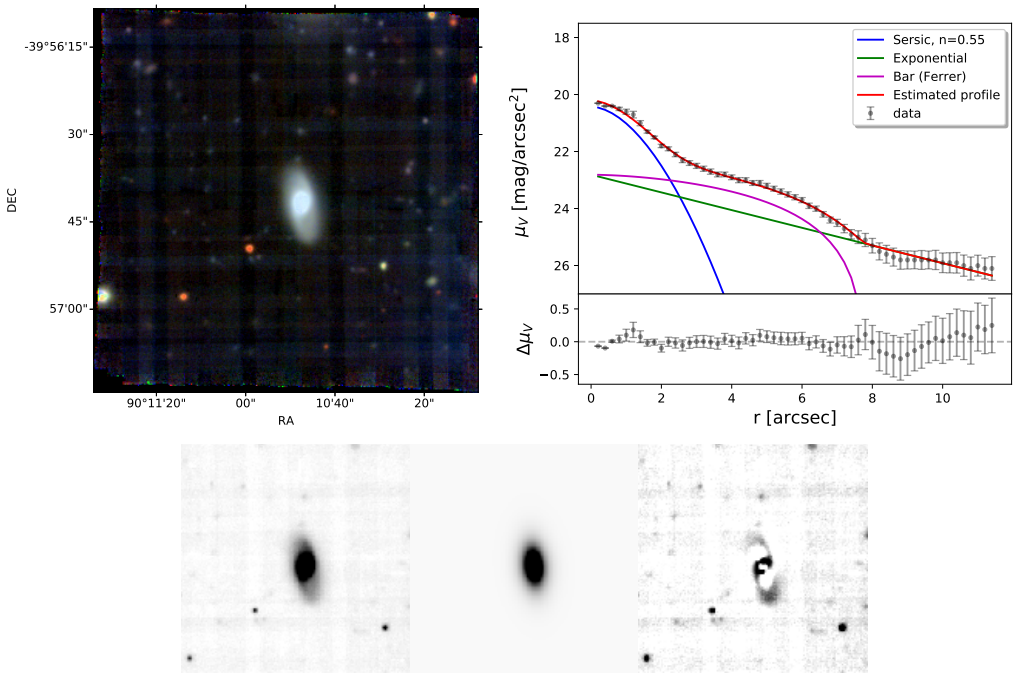

Figure 4.33: Color image from g, r, and i bands extracted from MUSE data-cube (upper left panel), surface brightness radial profile and photometric decomposition (upper right panel) and GALFIT output (input, model and residual image, lower panels) for A3376_B_0214.

GALFIT outputs (Figure 4.33). It has a Gaussian bulge with $n = 0.55$.
It has the higher value of the EW(Hβ) (Figure 4.36), since within r_e has a mean of 7.08 Å.
It shows a recent stellar burst about in the 5th age bin of star formation as the other sample galaxies, but between 0.06 and 0.2 Gyr ago it has undergone a more strong episode of star formation (7th age bin, Figure 3.22). The central population shifted in recent epochs as in earlier times, from E to W and the other way around.

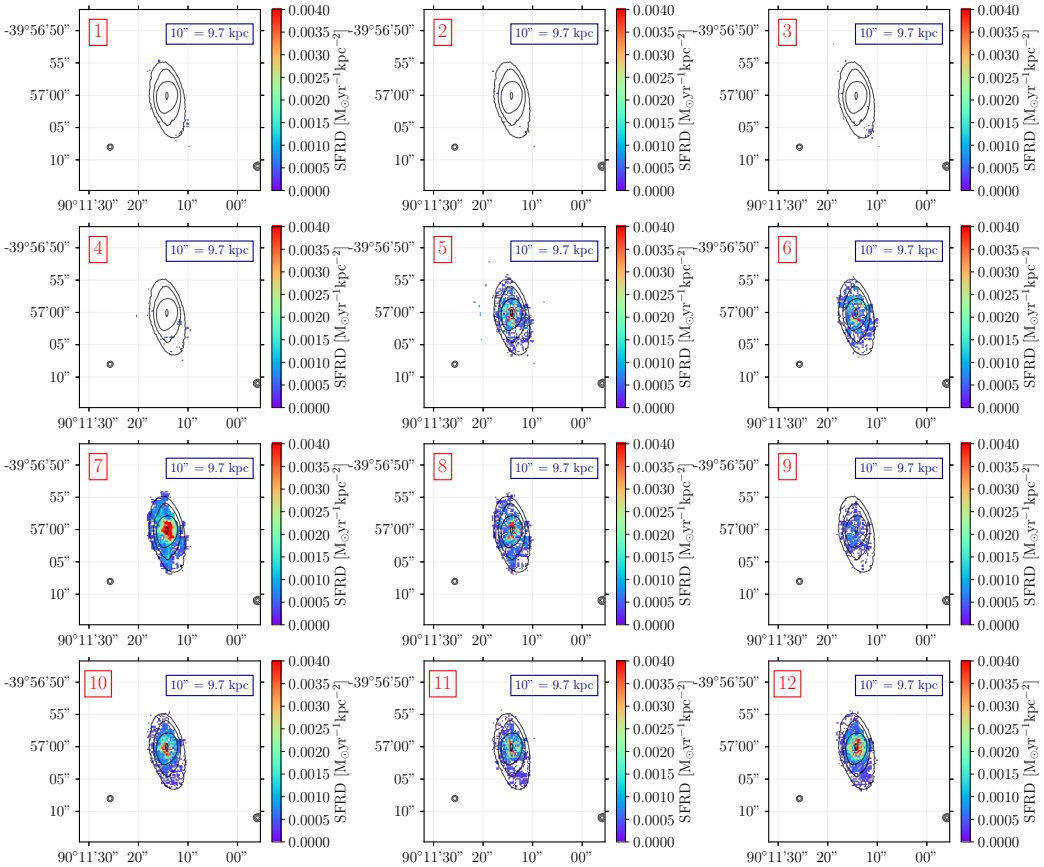

Figure 4.34: Age bins of the SFRD of A3376_B_0214. In the 7$^{\text{th}}$ bin we can notice the central burst of star formation (corresponding to $2.0 \cdot 10^8$ yr $\leq t \leq 5.7 \cdot 10^8$ yr ago). We excluded bad pixel data and values less than 10^{-4} for the SFRD from these maps.

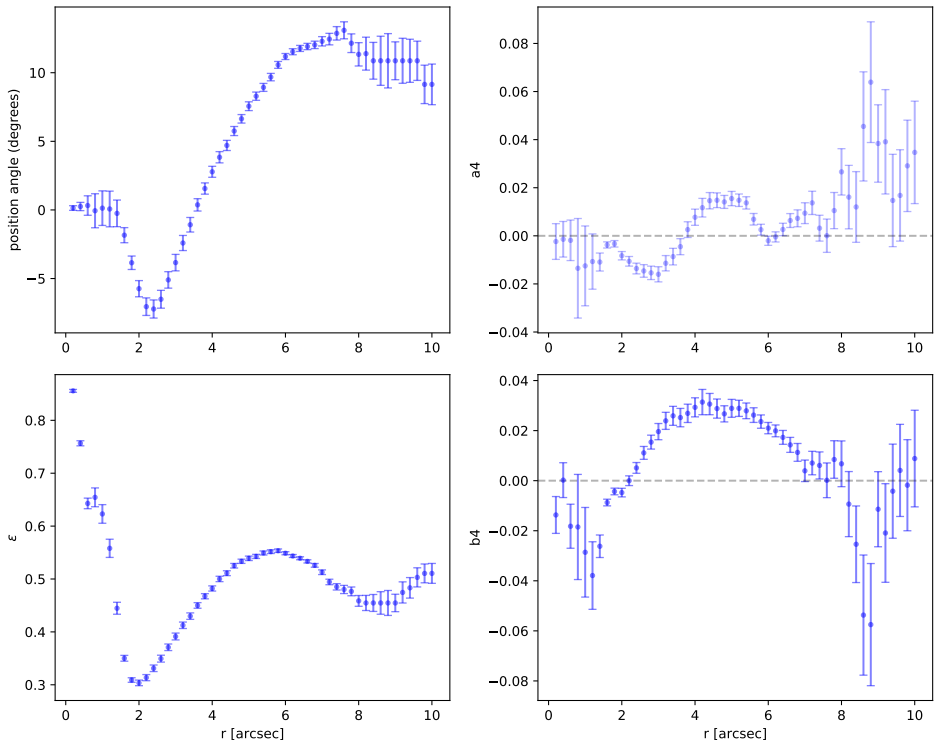

Figure 4.35: Radial profiles of the position angle, ellipticity, A4 and B4 for A3376_B_0214, from `ellipse`.

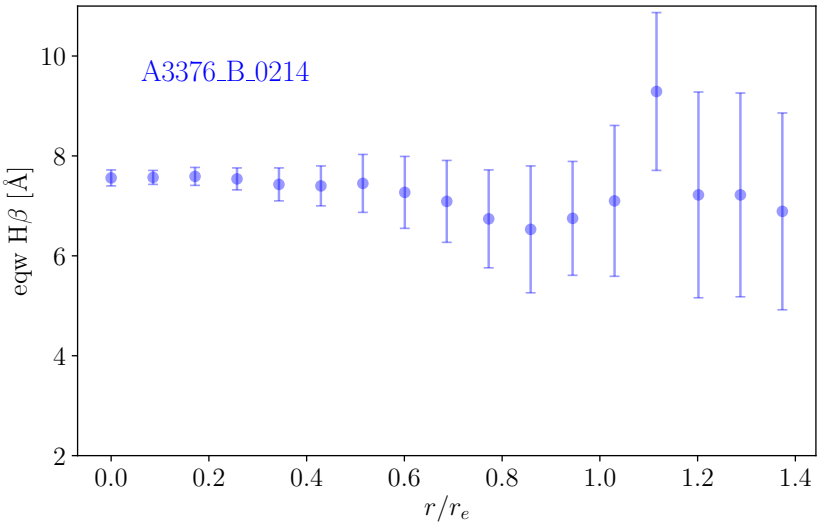

Figure 4.36: Averaged radial mean profile of EW(Hβ) for A3376_B_0214.

Chapter 5

Main results

Here I discuss the main results. In the Section 5.1 I present the specific angular momentum analysis derived from ATLAS^{3D} (Emsellem et al., 2004). Moreover I show the color-magnitude diagram for the sample galaxies (Section 5.2), the phase space analysis to search common features that characterize PSB galaxies in clusters (Section 5.3), and the correlation between EW(Hβ) and galaxy stellar mass and age (Section 5.5).

5.1 Specific angular momentum

To have a more complete view of the characteristics of the galaxies in our sample, as a last step we derived their specific angular momentum λ (Emsellem et al., 2004). It quantifies the global dynamical state of a galaxy. The two-dimensional stellar kinematics for elliptical, S0 and early spiral galaxies, shows a wide variety of features such as kinematically-decoupled or counter-rotating cores, central disks and velocity twists (Emsellem et al. 2004). Moreover, galaxies can be separated in two main classes: fast and slow rotators. Fast rotators exhibit velocity fields with a large-scale rotation pattern, while slow rotators show a lower or no sign of rotation.
This distinction between fast and slow rotators cannot be a mere consequence of inclination. Emsellem et al. (2004) highlighted that fast rotators tend to be relatively low-luminosity galaxies with $M_B \leq -20.5$, while slow rotators are brighter and more massive, and have a wide range of absolute magnitudes.
In order to distinguish these two classes, the anisotropy diagram V/σ-ϵ (Binney 1978), compares the observed amount of rotation with the apparent flattening of a galaxy. With long-slit spectra, the maximum observed

rotational velocity $V_{\{rmmax}$ and the central dispersion σ_0 are generally used. In two-dimensional spectroscopy, the observables contain much more information and the two-dimensional velocity field for stellar kinematics can be used. By averaging velocities and velocities dispersions to build the V/σ-ϵ diagram (Binney 2005). I obtained λ_{re} (Cappellari et al. 2007), defined as:

$$\lambda_{Re} = \frac{\langle R|V|\rangle}{\langle R\sqrt{V^2+\sigma^2}\rangle}. \tag{5.1}$$

This parameter defines a selection criterion between slow and fast rotators. The $< R|V| >$ term expresses the total angular momentum, where R is the distance from the center of the galaxy, and V the rotation velocity.
The absolute value of V is used as we are interested in the presence of local streaming motion. The denominator normalizes the expression, with $\sqrt{V^2+\sigma^2}$ being the second-order velocity moment. Therefore I constructed for the sample galaxy the anisotropy diagram, which relates the ratio of the ordered and random motion in a galaxy, to its observed ellipticity (Figure 5.1). Fast rotators and slow rotators are split in Figure 5.1 by the black curve of equation:

$$\lambda = 0.31 \cdot \sqrt{\epsilon}. \tag{5.2}$$

As we observe galaxies in the sky with an inclination i ($i = 90°$ corresponding to an edge-on galaxy) due to our reference frame, we have to correct the V/σ value for an edge-on view:

$$\left(\frac{V}{\sigma}\right) = \left(\frac{V}{\sigma}\right)_{\rm obs} \frac{\sqrt{1-\delta\cos^2 i}}{\sin i} \tag{5.3}$$

with $(V/\sigma)_{\rm obs}$ the observed value for V/σ, and δ the anisotropy parameter.

$$\epsilon_{\rm intr} = 1 - \sqrt{1 + \frac{\epsilon(\epsilon-2)}{\sin^2 i}} \tag{5.4}$$

with $\epsilon_{\rm intr}$ the intrinsic value for ellipticity and ϵ the observed one.
Under the oblate hypotesis, we can obtain the anisotropy parameter δ (Binney 2005):

$$\delta = 1 - \frac{1+(V/\sigma)^2}{[1-\alpha(V/\sigma)^2]\Omega_e} \tag{5.5}$$

with

$$e = \sqrt{1-(1-\epsilon_{intr})^2} \tag{5.6}$$

and

$$\Omega_e = \frac{0.5\arcsin e - e\sqrt{1-e^2}}{e\sqrt{1-e^2} - (1-e^2)\arcsin e}. \tag{5.7}$$

Galaxy	ϵ	λ_{Re}	$r_{\rm e}$ (arcsec)
A3376_B_0214	0.47	0.487	2.33
A3128_B_0248	0.48	0.493	2.22
A3158_B_0234	0.30	0.693	3.01
A3158_11_91	0.15	0.480	4.76
A500_F_0152	0.33	0.314	2.17
A3158_B_0223	0.10	0.403	4.90
A1069_B_0103	0.59	0.535	1.98
A500_22_184	0.66	0.616	2.17

Table 5.1: Observed mean ellipticity, specific angular momentum parameter, and effective radius taken from the single Sérsic fit with GASPHOT.

α is a dimensionless number, which does not depend on the galaxy amount of rotation, but only on the stellar density and velocity on the rotation plane. It is $\alpha \sim 0.15$ for an isotropic model. The value of i and δ are degenerated parameters, so we cannot derive the one from the other. Cappellari et al. (2007) suggested to proceed iteratively and they showed how the correction depends very little on δ.
In the λ_{Re} vs ϵ plot (Figure 5.1), the isotropy relation from edge-on galaxies, obtained from Equation 5.5, putting $\alpha = 0$ and $\delta = 0$ is also plotted:

$$\lambda_{Re} = 0.89\sqrt{\frac{\epsilon}{1-\epsilon}} \tag{5.8}$$

which corresponds to the red line.
In Figure 5.1 the blue line is the relation

$$\lambda_{Re} = \sqrt{\frac{(0.09 + 0.1\epsilon)\epsilon}{1-\epsilon}} \tag{5.9}$$

which approximately traces the location of the observed galaxies on the $(V/\sigma, \epsilon)$ diagram for edge-on galaxies.

The resulting λ_{Re} from our galaxy sample (Table 5.1) shows $\lambda_{Re} > 0.3$. Therefore all galaxies belong to the fast-rotator class.

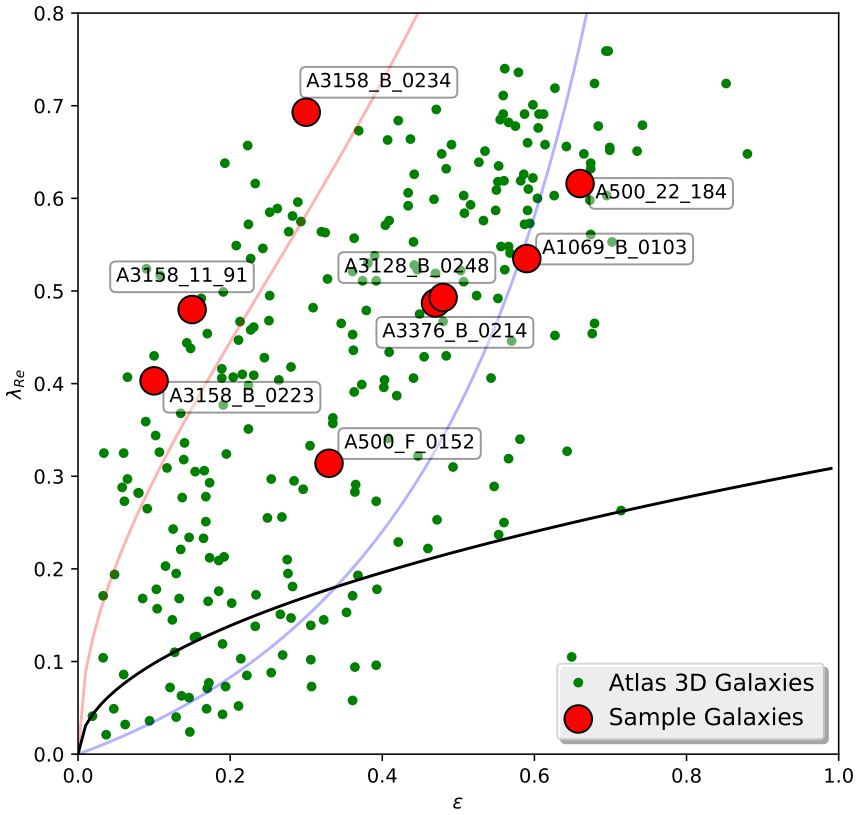

Figure 5.1: Anisotropy diagram for the sample galaxies (red dots) compared with ATLAS^{3D} sample (green dots). Slow and fast rotators are split by the black line. Both red and blue lines are related to edge-on galaxies: the first one is the isotropy relation, while the latter one corresponds to the relation $\delta = 0.7\epsilon_{intr}$ in the anisotropy diagram.

5.2 Color-magnitude diagram

In Figure 5.2 we superimposed our data to the color-magnitude diagram of PSB galaxies in the WINGS sample from Paccagnella et al. (2017). To this purpose we derived the absolute total magnitude in V band and the color $B-V$ (also derived from the B and V-band total absolute magnitudes) from the WINGS catalogue (Varela et al., 2009).
From this plot, I can see that the majority of our sample galaxies are in the redder part of the plot, in the so called red sequence. Two galaxies are in the transition region, between the red sequence and the blue cloud. A third one, A3158_B_0234, is at the limit of the transition zone, marked by the black line. The two galaxies in the transition region belong to the Abell 500 cluster. Note that these are also the least luminous and the only unbarred galaxies in the sample.

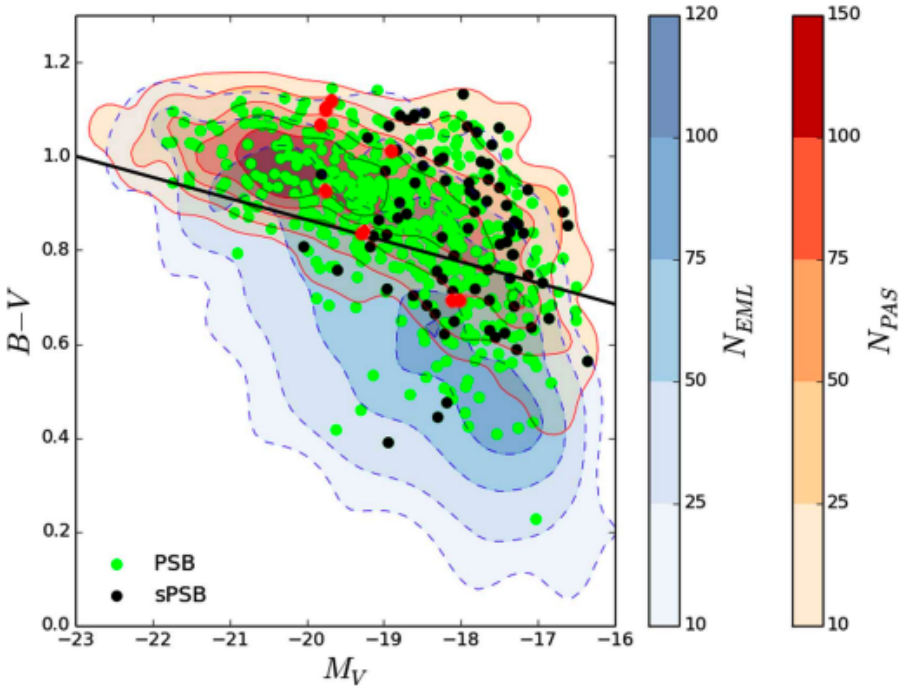

Figure 5.2: Color-magnitude diagram from Paccagnella et al., 2017. Red and blue-dashed contours are the number densities of passive and emission line galaxies, respectively. The black line represents the selection limit that Paccagnella et al. (2017) adopted to select red and blue galaxies. Red dots are our sample galaxies, Green dots: PSB; black dots: PSB with EW(Hδ) > 6 Å.

5.3 PSB galaxies in the phase-space

It is well known that in clusters there is a relation between morphology and density of galaxies (Dressler, 1980). Early type galaxies are frequent in high density regions while late-type ones are rare in the centers of clusters. The density of spirals increases with decreasing density. In clusters there is also a luminosity dependence: the brightest galaxies are in general very close to the center of the cluster (Oemler, 1974).
In this scenario one important tool to use is the projected phase-space diagram. This diagram correlates the $\Delta V/\sigma$ quantity with the r/r_{200} radius, where ΔV is the difference of the systemic velocity of the galaxy with respect to that of the cluster, σ is the velocity dispersion of the cluster and r/r_{200} is the distance of the galaxy from the assumed center of the cluster normalized to r_{200} that is the radius delimiting a sphere with a mean density equal to 200 times the critical density.
To derive the phase-space diagram for the sample galaxies, I obtained from Biviano et al., 2017 the values of r_{200}, σ, and z of the cluster. The position of the cluster center has been taken from an analysis of the X-ray emission (Gullieuszik, private communication).
As far as the PSB galaxies are concerned, no evident correlation has yet been found between their morphological/physical characteristics and position in the cluster. In Figure 5.3 from Muzzin et al., 2014, the PSB seem to concentrate in the central regions of the cluster and show no sign of some kind of segregation. In Figure 5.4 we show the phase-space for our PSB galaxies, which are color coded by the EW(Hβ). The two galaxies with highest values of EW(Hβ) are A3376_B_0214 and A500_F_0152. They exhibit low values for $\Delta V/\sigma$ and probably they are already virialized having $|\Delta V/\sigma| < 1$.
In the two phase-space diagrams in Figures 5.4 and 5.5, I plot the sample galaxies against the schematic of a galaxy trajectory falling into the cluster from Rhee et al. (2017), until $z = 0$. At the beginning, the galaxy is found in the "infalling" region (between A and B). After the first pericenter passage, it approaches apocenter at C. If the apocenter is beyond the cluster virial radius, then the galaxy is found in the "back-splash" region. Between C and D, the object settles into the lower-left hand corner of the diagram, known as the "virialized region". The black dashed line is the escape velocity curve of the cluster, calculated assuming a NFW halo density profile (Navarro et al., 1996) and a concentration parameter $c = 6$ (Gill et al., 2004). Seven sample galaxies are inside the escape velocity curve of the cluster and the one outside has a low value for EW(Hβ)<4 Å. Moreover, I notice that the galaxies with higher values of EW(Hβ) are infalling into the virialized region.

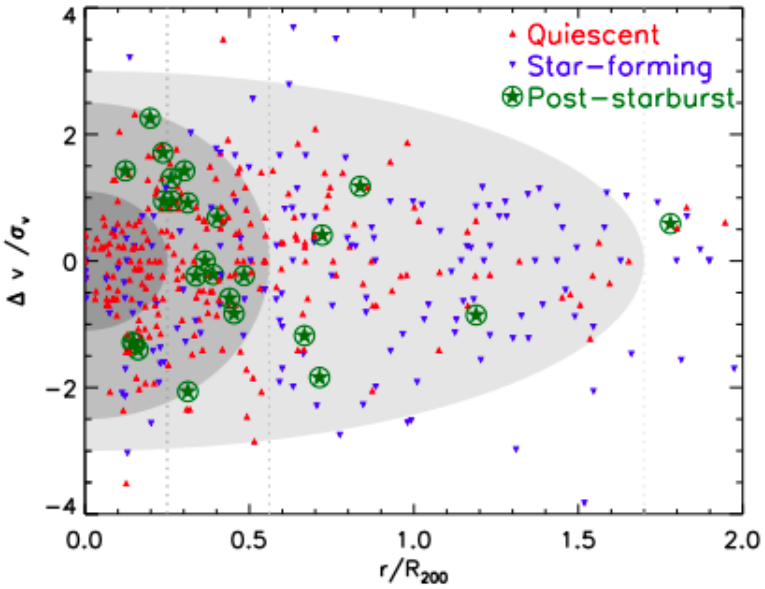

Figure 5.3: Phase-space plot for PSB galaxies at z∼1 from Muzzin et al. (2014).

Since four of our sample galaxies show a bar in the surface brightness profiles and two others exhibit residuals in the GALFIT output maps that may let consider a presence of a nuclear bar, I search for a correlation between the phase-space position and galaxy morphology. Figure 5.5 is represented the phase space plot with a third axis to highlight the presence of a bar. There is no correlation between morphology and position in the cluster.
However, plotting the infalling sequence curve in the diagram, three of four galaxies with a bar are close to the virialized region.

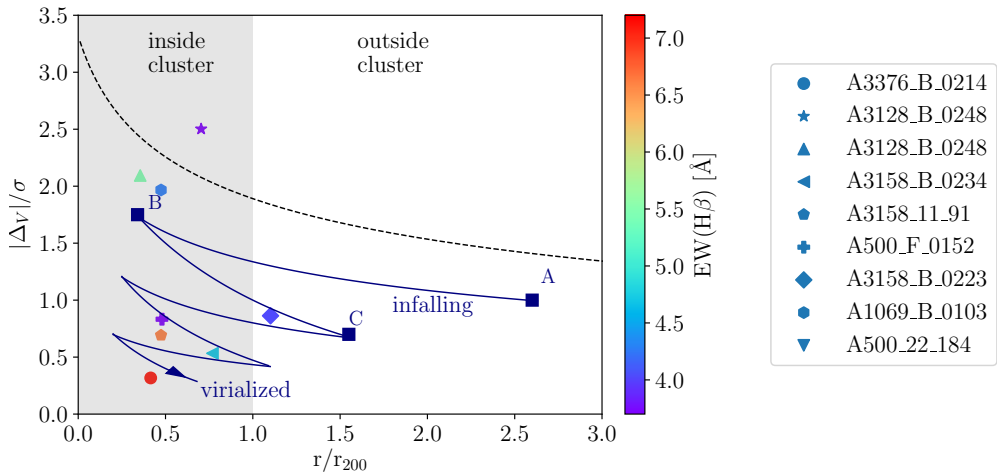

Figure 5.4: Phase space diagram for the sample galaxies. The color bar gives the EW(Hβ). The black dashed curve represents the escape velocity from the cluster as a function of r/r_{200} from Rhee et al. (2017). The blue curve is the infalling sequence of a galaxy into the cluster potential well.

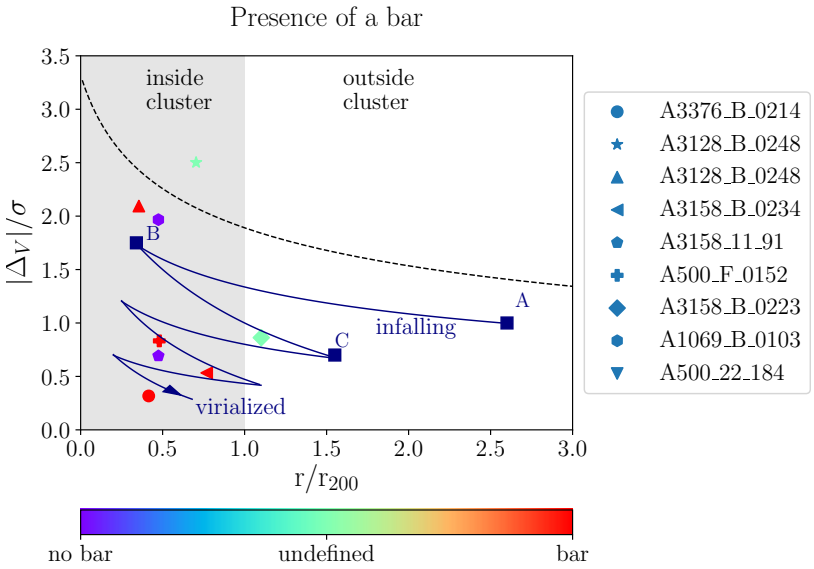

Figure 5.5: Phase-space diagram for the sample galaxies. The color bar marks the presence of a bar.The black dashed curve represents the escape velocity from the cluster vs r/r_{200}, from Rhee et al., 2017. The black dashed curve represents the escape velocity from the cluster as a function of r/r_{200} from Rhee et al. (2017). The blue curve is the infalling sequence of a galaxy into the cluster potential well.

5.4 Stellar mass vs (EW(Hβ)) mean

To check possible correlations between the properties of the sample galaxies and EW(Hβ), we plotted the stellar mass versus the EW(Hβ) mean within one r_e (figure 5.6).
I found that galaxies with higher stellar mass have a lower EW(Hβ), indicating that they have a more prominent young population than the less massive ones. Since the EWs obtained by SINOPSIS have errors of $\sim$ 2 Å (i.e. is 50% for a 4 Å measured value) these results must be taken with care.
For what concerns EW(Mg_b), the mass correlates directly with this parameter. This result was predictable, since Mg_b correlates with the stellar velocity dispersion (Ziegler and Bender, 1997), which is a proxy of the galaxy mass (Gültekin et al., 2009; Zubovas and King, 2012). Thus, a proportional correlation in the Hβ case seems visible, an inverse one for what concerns Mg_b. The more massive galaxies are those with higher values of EW(Mg_b). I performed a linear fit to the data, the best-fitting parameters are in the plot legends.

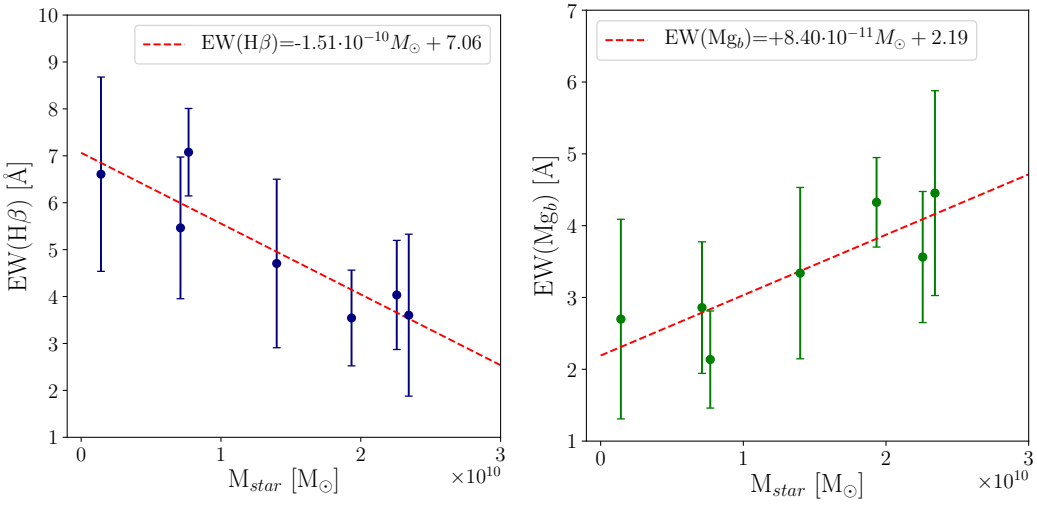

Figure 5.6: Mean EW(Hβ) and EW(Mg_b) as a function of the stellar mass for the sample galaxies. The red dashed line corresponds to the best-fitting of the data.

5.5 Mass-weighted age and luminosity-weighted age vs EW(Hβ) mean

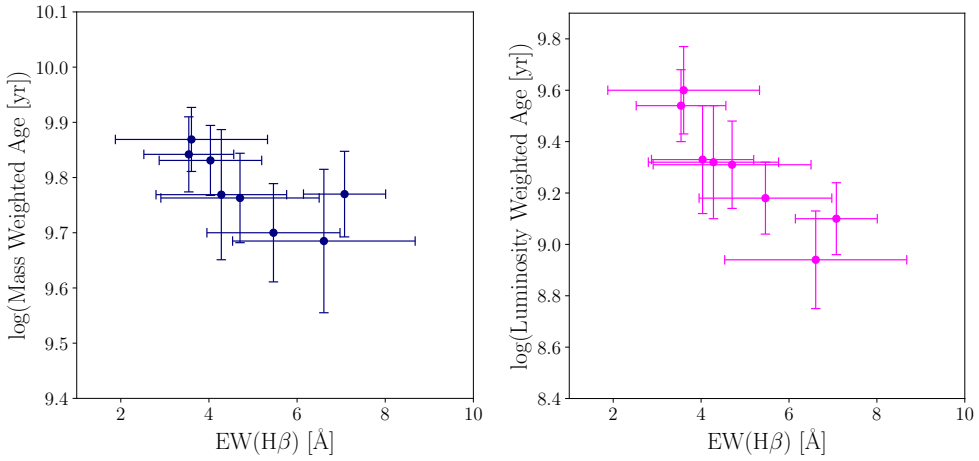

Figure 5.7: EW(Hβ) as a function of the mass-weighted (left panel) and luminosity-weighted age (right panel).

Despite the high errors, Figure 5.7 shows how the age correlates with EW(Hβ). This fact is evident in both mass-weighted age and luminosity-weighted age maps when compared with Hβ. The higher values of Hβ corresponds to the lower values of the stellar age. This is a confirmation of Hβ being a proxy of age (González Delgado et al., 1999). Younger A-type stars, for example, have stronger Balmer absoption lines than an older population of K stars.
Mass weighted-age values seems be systematically higher than the luminosity-weighted-age ones.

Chapter 6

Conclusions

In this Chapter I summarize the conclusions of this work.
I performed a spectro-photometric analysis of eight galaxies of the GASP sample and showing PSB features. In particular, I have compared their morphology, angular momentum, stellar population properties, and location within the cluster to obtain a valuable characterization of this kind of objects.
The main results can be summarized as follows:

- These galaxies are S0 or early-type spirals, showing different morphological features. From the photometric analysis, based on the surface-brightness radial profiles and a two-dimensional decomposition (performed with GALFIT and IRAF `bmodel`), it results that 50% of our galaxies have a bar. Two galaxies have central feature (probably an inner bar from which the spiral arms depart) and the remaining two are unbarred galaxies. All the galaxies show an extended disk and a small bulge, with $n \leq 3$.
- Following the ATLAS^{3D} analysis, I derived the λ parameter for each sample galaxy. All the sample galaxies are fast rotators.
- The analysis of the color-magnitude diagram points out that the majority of these galaxies are in the red sequence, while two lay in the green valley. The latter ones belong to the Abell 500 cluster and are also the less luminous and the only unbarred galaxies of the whole sample.
- SINOPSIS outputs provide measurements of the stellar populations features, such as SFR and EWs. I carried out an analysis of EW(Hβ), being the strongest line with the smallest errors in comparison to the others available absorption lines. Thus I plotted the EW(Hβ) profiles and compared them to the 12 age bins of SFR density shown in the

SINOPSIS outputs. All galaxies underwent a central star formation episode between $2.0 \cdot 10^7$ yr $\leq t \leq 5.7 \cdot 10^7$ yr ago. The only exception is A3376_B_0214 that has an older stellar population, with the more recent star formation in the central region between $2.0 \cdot 10^8$ yr $\leq t \leq 5.7 \cdot 10^8$ yr ago. Synthetic spectra offered a model prediction between EW(Hβ) and SSP age (Figure 3.19). In fact the galaxy with the highest value of EW(Hβ) (A3376_B_0214) shows the oldest burst of star formation (in figure 3.19 for an age of $0.20 < t < 0.57$ Gyr is predicted an 6.97<EW(Hβ)< 7.94 Å). EW(Hβ) mean profiles are almost constant for all galaxies within 0.5 r_e. Beyond this radius in three galaxies it increases (A500_F_0152, A3158_11_91, A500_22_184), while it decreases or remains constant at the increasing of the distance from the galaxy center in the remaining galaxies.

- I also found an anti-correlation between EW(Hβ) and EW(Mg$_b$) with the galaxy stellar masses. The resulting EW(Mg$_b$) shows a linear correlation with the stellar mass, while EW(Hβ) an inverse one. The EW(Mg$_b$) relation is expected, since it correlates with the stellar velocity dispersion (Ziegler and Bender, 1997), which is a proxy for the galaxy mass (Gültekin et al., 2009; Zubovas and King, 2012).
- Mass-weighted age seems to be a function of EW(Hβ) as well. SSP age decreases for increasing values of the EW(Hβ) as it could be predicted, since Hβ is stronger as the younger the SSP is.
- Phase-space analysis highlights that the two galaxies with the highest value of EW(Hβ) are in the virialized region of the cluster. Also the presence of a bar seems to correlate with the stripping sequence, but this latter result must to be taken with care.
- All the sample galaxies underwent a recent episode of starburst between $2.0 \cdot 10^7$ yr $\leq t \leq 5.7 \cdot 10^7$ yr ago, exception made for A3376_B_0214 which exhibits an older star formation event in the age bin in the range of $2.0 \cdot 10^8$ yr $\leq t \leq 5.7 \cdot 10^8$ yr ago. This galaxy has the highest value of EW(Hβ). Observing for each galaxy the SFH, the younger stars are concentrated in the central area and in most cases this population moves around the center of the galaxy. As the distance from the galaxy center increases, fewer young stars are found.

Bibliography

Bacon, R., Accardo, M., Adjali, L., Anwand, H., and Bauer, e. a. (2010). The MUSE Second-generation VLT Instrument. In *Proc. SPIE 7735, Ground-based and Airborne Instrumentation for Astronomy III*, volume 7735, page 773508.

Baldry, I. K., Balogh, M. L., Bower, R., Glazebrook, K., Nichol, R. C., Allen, R. E., Nanopoulos, D. V., and Pope, C. N. (2004). Color Bimodality: Implications for Galaxy Evolution. *The New Cosmology: Conference on Strings and Cosmology; The Mitchell Symposium on Observational Cosmology. AIP Conference Proceedings*, 743:106–119.

Balogh, M. L., Navarro, J. F., and Morris, S. L. (2000). The Origin of Star Formation Gradients in Rich Galaxy Clusters. *ApJ*, 540:113–121.

Bardelli, S., Zucca, E., Vettolani, G., Zamorani, G., Scaramella, R., Collins, C. A., and MacGillivray, H. T. (1994). A Study of the Core of the Shapley Concentration - I. The sample. *MNRAS*, 267:665–691.

Bardelli, S., Zucca, E., Zamorani, G., Vettolani, G., and Scaramella, R. (1998). A Study of the Core of the Shapley Concentration - III. Properties of the Clusters in the A3558 Complex. *MNRAS*, 296:599–613.

Binney, J. (1978). On the Rotation of Elliptical Galaxies. *MNRAS*, 183:501–514.

Binney, J. (2005). Rotation and Anisotropy of Galaxies Revisited. *MNRAS*, 363:937–942.

Binney, J. and Merrifield, M. (1998). *Galactic Astronomy.* Princeton University Press, Princeton, N.J.

Biviano, A., Moretti, A., Paccagnella, A., Poggianti, B. M., Bettoni, D., Gullieuszik, M., Vulcani, B., Fasano, G., D'Onofrio, M., Fritz, J., and Cava,

A. (2017). VizieR Online Data Catalog: Properties of the Sample of Clusters (Biviano+, 2017). *VizieR Online Data Catalog*, pages J/A+A/607/A81.

Bundy, K., Bershady, M. A., Law, D. R., Yan, R., Drory, N., MacDonald, N., and Wake, e. a. (2015). Overview of the SDSS-IV MaNGA Survey: Mapping nearby Galaxies at Apache Point Observatory. *ApJ*, 798:7–31.

Calvi, R., Poggianti, B. M., and Vulcani, B. (2011). The Padova-Millennium Galaxy and Group Catalogue (PM2GC): the Group-finding Method and the PM2GC Catalogues of Group, Binary and Single Field Galaxies. *MNRAS*, 416:727–738.

Cappellari, M., Emsellem, E., Bacon, R., Bureau, M., Davies, R. L., de Zeeuw, P. T., Falcón-Barroso, J., Krajnović, D., Kuntschner, H., McDermid, R. M., Peletier, R. F., Sarzi, M., van den Bosch, R. C. E., and van de Ven, G. (2007). The SAURON project - X. The Orbital Anisotropy of Elliptical and Lenticular Galaxies: Revisiting the V/σ-ϵ, diagram with Integral-field Stellar Kinematics. *MNRAS*, 379:418–444.

Cappellari, M., Emsellem, E., Krajnović, D., McDermid, R. M., Serra, P., Alatalo, K., Blitz, L., Bois, M., Bournaud, F., Bureau, M., Davies, R. L., Davis, T. A., de Zeeuw, P. T., Khochfar, S., Kuntschner, H., Lablanche, P.-Y., Morganti, R., Naab, T., Oosterloo, T., Sarzi, M., Scott, N., Weijmans, A.-M., and Young, L. M. (2011). The ATLAS^{3D} Project - VII. A New Look at the Morphology of Nearby Galaxies: the Kinematic Morphology-density Relation. *MNRAS*, 416:1680–1696.

Cava, A., Bettoni, D., Poggianti, B. M., Couch, W. J., Moles, M., Varela, J., Biviano, A., D'Onofrio, M., Dressler, A., Fasano, G., Fritz, J., Kjaergaard, P., Ramella, M., and Valentinuzzi, T. (2009). VizieR Online Data Catalog: WINGS Spectroscopy of 48 Galaxy Clusters (Cava+, 2009). *VizieR Online Data Catalog*, pages J/A+A/495/707.

Chabrier, G. (2003). Galactic Stellar and Substellar Initial Mass Function. *Publications of the Astronomical Society of the Pacific*, 115:763–795.

Ciambur, B. C. (2015). Beyond Ellipse(s): Accurately Modelling the Isophotal Structure of Galaxies with ISOFIT and CMODEL. *ApJ*, 810:120–133.

Ciambur, B. C. (2016). Profiler - A Fast and Versatile New Program for Decomposing Galaxy Light Profiles. *Publications of the Astronomical Society of Australia*, 33:e062, 16 pp.

Ciotti, L. (1991). Stellar Systems Following the $R^{1/m}$ Luminosity Law. *AAP*, 249:99–106.

Conselice, C. J. (2006). The Fundamental Properties of Galaxies and a New Galaxy Classification System. *MNRAS*, 373:1389–1408.

Couch, W. J. and Sharples, R. M. (1987). A Spectroscopic Study of Three Rich Galaxy Clusters at $z = 0.31$. *MNRAS*, 229:423–456.

Croom, S. M., Lawrence, J. S., Bland-Hawthorn, J., Bryant, J. J., Fogarty, L., Richards, S., Goodwin, M., Farrell, T., Miziarski, S., Heald, R., Jones, D. H., Lee, S., Colless, M., Brough, S., Hopkins, A. M., Bauer, A. E., Birchall, M. N., Ellis, S., Horton, A., Leon-Saval, S., Lewis, G., López-Sánchez, Á. R., Min, S.-S., Trinh, C., and Trowland, H. (2012). The Sydney-AAO Multi-object Integral Field Spectrograph. *MNRAS*, 421:872–893.

de Vaucouleurs, G. (1948). Recherches sur les Nebuleuses Extragalactiques. *Annales d'Astrophysique*, 11:247–287.

Dressler, A. (1980). Galaxy Morphology in Rich Clusters: Implications for the Formation and Evolution of Galaxies. *ApJ*, 236:351–365.

Dressler, A. and Gunn, J. E. (1983). Spectroscopy of Galaxies in Distant Clusters. II. The Population of the 3C 295 Cluster. *ApJ*, 270:7–19.

Emsellem, E., Cappellari, M., Peletier, R. F., McDermid, R. M., Bacon, R., Bureau, M., Copin, Y., Davies, R. L., Krajnović, D., Kuntschner, H., Miller, B. W., and de Zeeuw, P. T. (2004). The SAURON project - III. Integral-field Absorption-line Kinematics of 48 Elliptical and Lenticular Galaxies. *MNRAS*, 352:721–743.

Faber, S. M., Willmer, C. N. A., Wolf, C., Koo, D. C., Weiner, B. J., Newman, J. A., Im, M., Coil, A. L., Conroy, C., Cooper, M. C., Davis, M., Finkbeiner, D. P., Gerke, B. F., Gebhardt, K., Groth, E. J., Guhathakurta, P., Harker, J., Kaiser, N., Kassin, S., Kleinheinrich, M., Konidaris, N. P., Kron, R. G., Lin, L., Luppino, G., Madgwick, D. S., Meisenheimer, K., Noeske, K. G., Phillips, A. C., Sarajedini, V. L., Schiavon, R. P., Simard, L., Szalay, A. S., Vogt, N. P., and Yan, R. (2007). Galaxy Luminosity Functions to $z \sim 1$ from DEEP2 and COMBO-17: Implications for Red Galaxy Formation. *ApJ*, 665:265–294.

Fasano, G., Marmo, C., Varela, J., D'Onofrio, M., Poggianti, B. M., Moles, M., Pignatelli, E., Bettoni, D., Kjærgaard, P., Rizzi, L., Couch, W. J., and

Dressler, A. (2006). WINGS: a WIde-field Nearby Galaxy-cluster Survey. I. Optical Imaging. *A&A*, 445:805–817.

Fasano, G., Vanzella, E., and Wings Team (2007). MORPHOT: a Tool for Automatic Galaxy Morphology in Wide and/or Deep Fields. In Vallenari, A., Tantalo, R., Portinari, L., and Moretti, A., editors, *From Stars to Galaxies: Building the Pieces to Build Up the Universe*, volume 374, pages 495–496.

Ferreras, I. and Silk, J. (2003). On Breaking the Age-metallicity Degeneracy in Early-type Galaxies: Infall Versus Star Formation Efficiency. *MNRAS*, 344:455–460.

Franx, M. (1993). Kinematics of an e+a Galaxy in Abell 665 at $z = 0.18$. *ApJ*, 407:L5–L8.

Freeman, K. C. (1970). On the Disks of Spiral and S0 Galaxies. *ApJ*, 160:811–830.

Fritz, J., Moretti, A., Gullieuszik, M., Poggianti, B., Bruzual, G., Vulcani, B., Nicastro, F., Jaffé, Y., Cervantes Sodi, B., Bettoni, D., Biviano, A., Fasano, G., Charlot, S., Bellhouse, C., and Hau, G. (2017). GASP. III. JO36: A Case of Multiple Environmental Effects at Play? *ApJ*, 848:132.

Fritz, J., Poggianti, B. M., Bettoni, D., Cava, A., Couch, W. J., D'Onofrio, M., Dressler, A., Fasano, G., Kjærgaard, P., Moles, M., and Varela, J. (2007). A Spectrophotometric Model Applied to Cluster Galaxies: the WINGS Dataset. *A&A*, 470:137–152.

Fritz, J., Poggianti, B. M., Cava, A., Moretti, A., Varela, J., Bettoni, D., Couch, W. J., D'Onofrio D'Onofrio, M., Dressler, A., Fasano, G., Kjærgaard, P., Marziani, P., Moles, M., and Omizzolo, A. (2014). WINGS-SPE. III. Equivalent Width Measurements, Spectral Properties, and Evolution of Local Cluster Galaxies. *A&A*, 566:A32 (21 pp).

Fritz, J., Poggianti, B. M., Cava, A., Moretti, A., and WINGS Collaboration (2011). Equivalent Width Measurements in Optical Spectra of Galaxies in Local Clusters: Hints on the Star Formation History in Clusters. *Baltic Astronomy*, 20:435–441.

Gao, H. and Ho, L. C. (2017). An Optimal Strategy for Accurate Bulge-to-disk Decomposition of Disk Galaxies. *ApJ*, 845:114–140.

Gill, S. P. D., Knebe, A., Gibson, B. K., and Dopita, M. A. (2004). The Evolution of Substructure - II. Linking Dynamics to Environment. *MNRAS*, 351:410–422.

González Delgado, R. M., Leitherer, C., and Heckman, T. M. (1999). Synthetic Spectra of H Balmer and HE I Absorption Lines. II. Evolutionary Synthesis Models for Starburst and Poststarburst Galaxies. *The Astrophysical Journal Supplement Series*, 125:489–509.

Goto, T. (2005). 266 e+a Galaxies Selected from the Sloan Digital Sky Survey Data Release 2: the Origin of e+a Galaxies. *MNRAS*, 357:937–944.

Goto, T., Okamura, S., Sekiguchi, M., Bernardi, M., Brinkmann, J., Gómez, P. L., Harvanek, M., Kleinman, S. J., Krzesinski, J., Long, D., Loveday, J., Miller, C. J., Neilsen, E. H., Newman, P. R., Nitta, A., Sheth, R. K., Snedden, S. A., and Yamauchi, C. (2003). The Environment of Passive Spiral Galaxies in the SDSS. *PASJ*, 55:757–770.

Gullieuszik, M., Poggianti, B., Fasano, G., Zaggia, S., Paccagnella, A., Moretti, A., Bettoni, D., D'Onofrio, M., Couch, W. J., Vulcani, B., Fritz, J., Omizzolo, A., Baruffolo, A., Schipani, P., Capaccioli, M., and Varela, J. (2015). VizieR Online Data Catalog: OmegaWINGS BV photometry (Gullieuszik+, 2015). *VizieR Online Data Catalog*, pages J/A+A/581/A41.

Gültekin, K., Richstone, D. O., Gebhardt, K., Lauer, T. R., Tremaine, S., Aller, M. C., Bender, R., Dressler, A., Faber, S. M., Filippenko, A. V., Green, R., Ho, L. C., Kormendy, J., Magorrian, J., Pinkney, J., and Siopis, C. (2009). The M-σ and M-L Relations in Galactic Bulges, and Determinations of Their Intrinsic Scatter. *ApJ*, 698:198–221.

Gunn, J. E. and Dressler, A. (1988). Cluster galaxies at high redshift. In Kron, R. G. and Renzini, A., editors, *Towards Understanding Galaxies at Large Redshift*, volume 141, pages 227–237.

Holmberg, E. (1946). On the Apparent Diameters and the Orientation in Space of Extragalactic Nebulae. *Meddelanden fran Lunds Astronomiska Observatorium Serie II*, 117:3–82.

Hubble, E. (1926). No. 324. Extra-galactic nebulae. *Contributions from the Mount Wilson Observatory / Carnegie Institution of Washington*, 324:1–49.

Jedrzejewski, R. I. (1987). CCD Surface Photometry of Elliptical Galaxies - I. Observations, Reduction and Results. *MNRAS*, 226:747–768.

Kennicutt, R. C. and Evans, N. J. (2012). Star Formation in the Milky Way and Nearby Galaxies. *Annual Review of Astronomy and Astrophysics*, 50:531–608.

Liu, G., Calzetti, D., Hong, S., Whitmore, B., Chandar, R., O'Connell, R. W., Blair, W. P., Cohen, S. H., Frogel, J. A., and Kim, H. (2013). Extinction and Dust Geometry in M83 HII Regions: An Hubble Space Telescope/WFC3 Study. *ApJ*, 778:L41 (6 pp).

Moretti, A., Gullieuszik, M., Poggianti, B., Paccagnella, A., Couch, W. J., Vulcani, B., Bettoni, D., Fritz, J., Cava, A., Fasano, G., D'Onofrio, M., and Omizzolo, A. (2017). OmegaWINGS: Spectroscopy in the Outskirts of Local Clusters of Galaxies. *A&A*, 599:A81 (11 pp).

Muzzin, A., van der Burg, R. F. J., McGee, S. L., Balogh, M., Franx, M., Hoekstra, H., Hudson, M. J., Noble, A., Taranu, D. S., Webb, T., Wilson, G., and Yee, H. K. C. (2014). The Phase Space and Stellar Populations of Cluster Galaxies at $z \sim 1$: Simultaneous Constraints on the Location and Timescale of Satellite Quenching. *ApJ*, 796:65–76.

Nair, P. B. and Abraham, R. G. (2010). On the Fraction of Barred Spiral Galaxies. *ApJ*, 714:L260–L264.

Navarro, J. F., Eke, V. R., and Frenk, C. S. (1996). The Cores of Dwarf Galaxy Haloes. *MNRAS*, 283:L72–L78.

Oemler, Augustus, J. (1974). The Systematic Properties of Clusters of Galaxies. Photometry of 15 Clusters. *ApJ*, 194:1–20.

Paccagnella, A., Vulcani, B., Poggianti, B. M., Fritz, J., Fasano, G., Moretti, A., Jaffé, Y. L., Biviano, A., Gullieuszik, M., Bettoni, D., Cava, A., Couch, W., and D'Onofrio, M. (2017). OmegaWINGS: The First Complete Census of Post-starburst Galaxies in Clusters in the Local Universe. *ApJ*, 838:148–162.

Peng, C. Y., Ho, L. C., Impey, C. D., and Rix, H.-W. (2002). Detailed Structural Decomposition of Galaxy Images. *ApJ*, 124:266–293.

Peng, C. Y., Ho, L. C., Impey, C. D., and Rix, H.-W. (2010). Detailed Decomposition of Galaxy Images. II. Beyond Axisymmetric Models. *AJ*, 139:2097–2129.

Pignatelli, E., Fasano, G., and Cassata, P. (2006). GASPHOT: a tool for Galaxy Automatic Surface PHOTometry. *A&A*, 446:373–388.

Poggianti, B. M. (2004). Modeling Stellar Populations in Cluster Galaxies. In Mulchaey, J. S., Dressler, A., and Oemler, A., editors, *Clusters of Galaxies: Probes of Cosmological Structure and Galaxy Evolution*, page 245.

Poggianti, B. M., Bressan, A., and Franceschini, A. (2001). Star Formation and Selective Dust Extinction in Luminous Starburst Galaxies. *ApJ*, 550:195–203.

Poggianti, B. M., Fasano, G., Omizzolo, A., Gullieuszik, M., Bettoni, D., Moretti, A., Paccagnella, A., Jaffe, Y. L., Vulcani, B., Fritz, J., Couch, W., and D'Onofrio, M. (2016). VizieR Online Data Catalog: Jellyfish Galaxy Candidates in Galaxy Clusters (Poggianti+, 2016). *VizieR Online Data Catalog*, page J/AJ/151/78.

Poggianti, B. M., Moretti, A., Gullieuszik, M., Fritz, J., Jaffé, Y., Bettoni, D., Fasano, G., Bellhouse, C., Hau, G., Vulcani, B., Biviano, A., Omizzolo, A., Paccagnella, A., D'Onofrio, M., Cava, A., Sheen, Y. K., Couch, W., and Owers, M. (2017). GASP. I. Gas Stripping Phenomena in Galaxies with MUSE. *ApJ*, 844:48–69.

Poggianti, B. M., Smail, I., Dressler, A., Couch, W. J., Barger, A. J., Butcher, H., Ellis, R. S., and Oemler, Augustus, J. (1999). The Star Formation Histories of Galaxies in Distant Clusters. *ApJ*, 518:576–593.

Rhee, J., Smith, R., Choi, H., Yi, S. K., Jaffé, Y., Candlish, G., and Sánchez-Jánssen, R. (2017). Phase-space Analysis in the Group and Cluster Environment: Time Since Infall and Tidal Mass Loss. *ApJ*, 843:128–141.

Rosales-Ortega, F. F., Kennicutt, R. C., Sánchez, S. F., Díaz, A. I., Pasquali, A., Johnson, B. D., and Hao, C. N. (2010). PINGS: the PPAK IFS Nearby Galaxies Survey. *MNRAS*, 405:735–758.

Sánchez, S. F., Kennicutt, R. C., Gil de Paz, A., van den Ven, G., Vilchez, J. M., Wisotzki, L., Marino, R. A., Mármol-Queraltó, E., Mast, D., and Viironen, K. (2011). CALIFA, the Calar Alto Legacy Integral Field Area survey: Early Report. In Zapatero Osorio, M. R., Gorgas, J., Maíz Apellániz, J., Pardo, J. R., and Gil de Paz, A., editors, *Highlights of Spanish Astrophysics VI*, pages 339–344.

Sarzi, M., Iodice, E., Coccato, L., Corsini, E. M., de Zeeuw, P. T., Falcón-Barroso, J., Gadotti, D. A., Lyubenova, M., McDermid, R. M., van de Ven, G., Fahrion, K., Pizzella, A., and Zhu, L. (2018). Fornax3D project: Overall Goals, Galaxy Sample, MUSE Data Analysis, and Initial Results. *AAP*, 616:A121.

Sérsic, J. L. (1963). Influence of the Atmospheric and Instrumental Dispersion on the Brightness Distribution in a Galaxy. *Boletin de la Asociacion Argentina de Astronomia La Plata Argentina*, 6:41.

Shapley, H. (1930). Note on a Remote Cloud of Galaxies in Centaurus. *Harvard College Observatory Bulletin*, 874:9–12.

Strateva, I., Ivezić, Ž., Knapp, G. R., Narayanan, V. K., Strauss, M. A., and Gunn, e. a. (2001). Color Separation of Galaxy Types in the Sloan Digital Sky Survey Imaging Data. *AJ*, 122:1861–1874.

Varela, J., D'Onofrio, M., Marmo, C., Fasano, G., Bettoni, D., Cava, A., Couch, J. W., Dressler, A., Kjaergaard, P., Moles, M., Pignatelli, E., Poggianti, M. B., and Valentinuzzi, T. (2009). VizieR Online Data Catalog: WINGS: Deep optical Phot. of 77 Nearby Clusters (Varela+, 2009). *VizieR Online Data Catalog*, pages J/A+A/497/667.

Wuyts, S., Labbé, I., Franx, M., Rudnick, G., van Dokkum, P. G., Fazio, G. G., Förster Schreiber, N. M., Huang, J., Moorwood, A. F. M., Rix, H.-W., Röttgering, H., and van der Werf, P. (2007). What Do We Learn from IRAC Observations of Galaxies at $2 < z < 3.5$? *ApJ*, 655:51–65.

Yesuf, H. M., Faber, S. M., Trump, J. R., Koo, D. C., Fang, J. J., Liu, F. S., Wild, V., and Hayward, C. C. (2014). From Starburst to Quiescence: Testing Active Galactic Nucleus feedback in Rapidly Quenching Post-starburst Galaxies. *ApJ*, 792:84.

York, D. G., Adelman, J., Anderson, John E., J., Anderson, S. F., Annis, J., Bahcall, N. A., and SDSS Collaboration (2000). The Sloan Digital Sky Survey: Technical Summary. *AJ*, 120:1579–1587.

Zabludoff, A. I., Zaritsky, D., Lin, H., Tucker, D., Hashimoto, Y., Shectman, S. A., Oemler, A., and Kirshner, R. P. (1996). The Environment of e+a Galaxies. *ApJ*, 466:104.

Ziegler, B. L. and Bender, R. (1997). The Mg_b-sigma Relation of Elliptical Galaxies at $z \sim 0.37$. *MNRAS*, 291:527–543.

Zubovas, K. and King, A. R. (2012). The M-σ Relation in Different Environments. *MNRAS*, 426:2751–2757.

Zucca, E., Zamorani, G., Scaramella, R., and Vettolani, G. (1993). All-Sky Catalogs of Superclusters of Abell-ACO Clusters. *ApJ*, 407:470.